

Viscoelastic Free Surface Instabilities During Exponential Stretching

by

Ryan D. Welsh

B.S., Mechanical Engineering
University of Cincinnati, 2000


Submitted to the Department of Mechanical Engineering
in partial fulfillment of the Requirements for the Degree of
Master of Science in Mechanical Engineering

at the
Massachusetts Institute of Technology
December 2001

© 2001 Massachusetts Institute of Technology
All Rights reserved

Signature of Author 
Department of Mechanical Engineering
December 20, 2001

Certified by 
Gareth H. McKinley
Professor of Mechanical Engineering
Thesis Supervisor

Accepted by 
Ain A. Sonin
Chairman, Department Committee on Graduate Students

Acknowledgements

The person who I owe the most for helping me to accomplish this thesis is Canee, who was patient enough to put off getting a ‘real’ place to live and who agreed to spend two more years living like a student; I am happy that I will now finally be able to spend more time with her and Zachary.

I thank my advisor, Gareth McKinley, for his guidance throughout this project. I feel very lucky to have worked with Gareth over the past year and a half. Although he is constantly busy, he always took time to answer my questions, and I am grateful to him for making my time here at MIT both an enjoyable and enriching experience. I was able to do and learn much more than I expected while here, thanks to Gareth.

I am also heavily indebted to José Bico, my friend and coworker on this project, for all of his help, good ideas, and insights. This thesis would not be what it is without his input. José will make a great professor next year.

Thanks to everyone in the lab for making our lab such a fun and interesting place to work. I really hate to leave such a great environment, but then I think of moving all of the equipment back to Building 3 and I come back to my senses! Anyway, I have a lot of friends here at MIT and it is definitely hard to leave for that reason.

Finally, I have to acknowledge my financial support. The bulk of the funding, I think, has come from my parents, who have generously kept us going for the past couple years. In addition, I appreciate the funding I got from the Department in the form of the Rohsenow Fellowship and I thank NASA Glenn for funding this research.

Viscoelastic Free Surface Instabilities During Exponential Stretching

by

Ryan D. Welsh

Submitted to the Department of Mechanical Engineering
on December 20, 2001 in partial fulfillment of the
requirements for the Degree of Master of Science in
Mechanical Engineering

ABSTRACT

A viscous Newtonian fluid and two model polystyrene Boger fluids are used to investigate the evolution of free-surface instabilities during the debonding of two cylindrical parallel rigid surfaces. A filament stretching rheometer is used to separate the surfaces at an exponential rate and simultaneously measure the evolution in the axial force. The experimental configuration also allows for simultaneous imaging of the fluid sample from beneath the endplate during the test. The test method is similar to both the probe-tack test used in adhesive testing and filament stretching rheometry experiments. Several geometric aspect ratios (defined as the ratio of initial sample height to radius) are used to vary the degree of sample confinement. These geometries bridge the gap between conventional adhesive testing and extensional rheometry. Three types of instabilities are seen in the experiments. The first is similar to the classical Saffman-Taylor instability, in which fingers of a less viscous fluid penetrate into a more viscous one during pressure driven flow. In the present three-dimensional analog, the instability occurs at a critical rate of plate separation for a given geometry and fluid. Larger pressure gradients result from higher fluid viscosity, a more confined geometry and greater rate of plate separation. A second instability is caused by the extensional stress growth in the elastic fluids and occurs at a critical Hencky strain for a given Deborah number. This instability is characterized by the growth of fingers radially outward from the base of a stable, cylindrical fluid column. As this instability progresses, the fingers can repeatedly bifurcate resulting in complex surface morphologies. Finally, cavitation in the test fluids occurs below a critical negative gage pressure within the fluid. Modal interactions of the three instabilities are also observed and lead to complex evolution of the elastic instability.

Thesis Supervisor: Gareth H. McKinley
Title: Professor of Mechanical Engineering

Table of Contents

Chapter 1	Introduction and Background.....	9
1.1	Non-Newtonian Fluids.....	9
1.1.1	Flow Behavior	11
1.1.2	The Role of Molecular Structure	13
1.2	Characterization of Non-Newtonian Fluids	15
1.2.1	Shear Rheometry: Cone and Plate Rheometer.....	18
1.2.2	Extensional Rheometry: Filament Stretching Rheometry	19
1.3	Pressure-Sensitive Adhesives (PSAs).....	22
1.3.1	Literature Review	23
1.3.2	The Probe-Tack Test	27
1.4	A Modified Probe-Tack Experiment	28
1.5	Summary.....	31
Chapter 2	Experimental Setup and Testing Method.....	33
2.1	Experiment.....	33
2.1.1	Flow Geometry and Experimental Setup.....	34
2.1.2	Sample Preparation and Loading.....	36
2.1.3	Temperature.....	37
2.2	FISER II Filament Stretching Rheometer	37
2.2.1	Motor Platens.....	37
2.2.2	Endplates and Endplate Assemblies	41
2.2.3	Data Acquisition.....	42
2.2.4	Force Measurements.....	43
2.2.5	Dynamic Testing of Futek load cells, Model L2338-Q10419	47
2.2.6	Video Imaging.....	49
2.3	Data Analysis.....	50
2.3.1	Force Data	51
2.4	Conclusion	55
Chapter 3	Test Fluids	57
3.1	Styrene-based fluids.....	58
3.1.1	Fluid Composition	59
3.1.2	Shear Rheometry	61
3.2	Polybutadiene Fluid	66

3.2.1	Fluid Composition	66
3.2.2	Shear Rheometry	67
Chapter 4	Experimental Results	73
4.1	Elastic Fingering Instability	75
4.1.1	Background.....	77
4.1.2	Results and Discussion	80
4.2	Saffman-Taylor Fingering Instability	87
4.2.1	Planar Saffman-Taylor Instability	88
4.2.2	Scaling Arguments for 3-D Radial Case	93
4.2.3	Results and Discussion	97
4.3	Cavitation.....	102
4.3.1	Results and Discussion	102
Chapter 5	Conclusions and Future Work	105
5.1	Conclusions.....	105
5.1.1	Stability Diagram.....	106
5.1.2	Adhesive properties	111
5.2	Future Work.....	115
5.3	Summary	117
Bibliography.....		119

Chapter 1 Introduction and Background

1.1 Non-Newtonian Fluids

Despite the exotic name, non-Newtonian fluids are fairly common. They occur naturally in the plant and animal kingdoms and are in many of foods; many bodily fluids are also non-Newtonian. Some specific examples include tree sap, ketchup, and saliva. Most plastics, or polymers, are processed in the liquid state and often exhibit strong non-Newtonian behavior. As a result, many commercial processes involve non-Newtonian fluid flows and one can easily see why knowledge of the flow characteristics of such fluids is important. Unfortunately, non-Newtonian fluid flows can be complex and unlike Newtonian flows, they are not yet completely understood. The experiments undertaken for this thesis investigate the free surface instabilities that can occur in uniaxial elongation of certain non-Newtonian fluids. Because of the similarities in flow conditions, these experiments can help to explain the fundamental physics involved in commercial applications such as the development of adhesives and the spinning of synthetic fibers.

A Newtonian fluid is a fluid that abides by Newton's law of viscosity, i.e., the stress tensor is proportional to the rate of strain tensor, which the constant of proportionality being the shear viscosity. In a two-dimensional shear flow, such as the flow found in a journal bearing inside an automotive engine, these equations reduce to the following expression:

$$\tau_{yx} = \mu \frac{\partial v_x}{\partial y}, \quad (1.1)$$

The term on the left in Equation 1.1 is the shear stress. The term on the right side is formed by the product of the shear viscosity, μ , and the shear rate. Thus, a fluid could be called non-Newtonian if its viscosity changed as a function of shear rate. A shear-thinning, or pseudoplastic, fluid has a viscosity that decreases with increasing shear rate. A shear thickening, or dilatant fluid is a non-Newtonian fluid that has a viscosity that increases with increasing shear rate. Returning to the journal bearing example; if such a non-Newtonian fluid were used to lubricate the bearing, the torque required to spin the bearing would not be proportional to the rotational speed, as it would be for a Newtonian lubricant. There are other definitions of non-Newtonian fluids; a Bingham plastic fluid (mayonnaise is an example of one) is a fluid that requires a threshold stress value, or

yield stress before it flows. The shear flow behaviors of some types of non-Newtonian fluids are shown graphically in Figure 1.1.

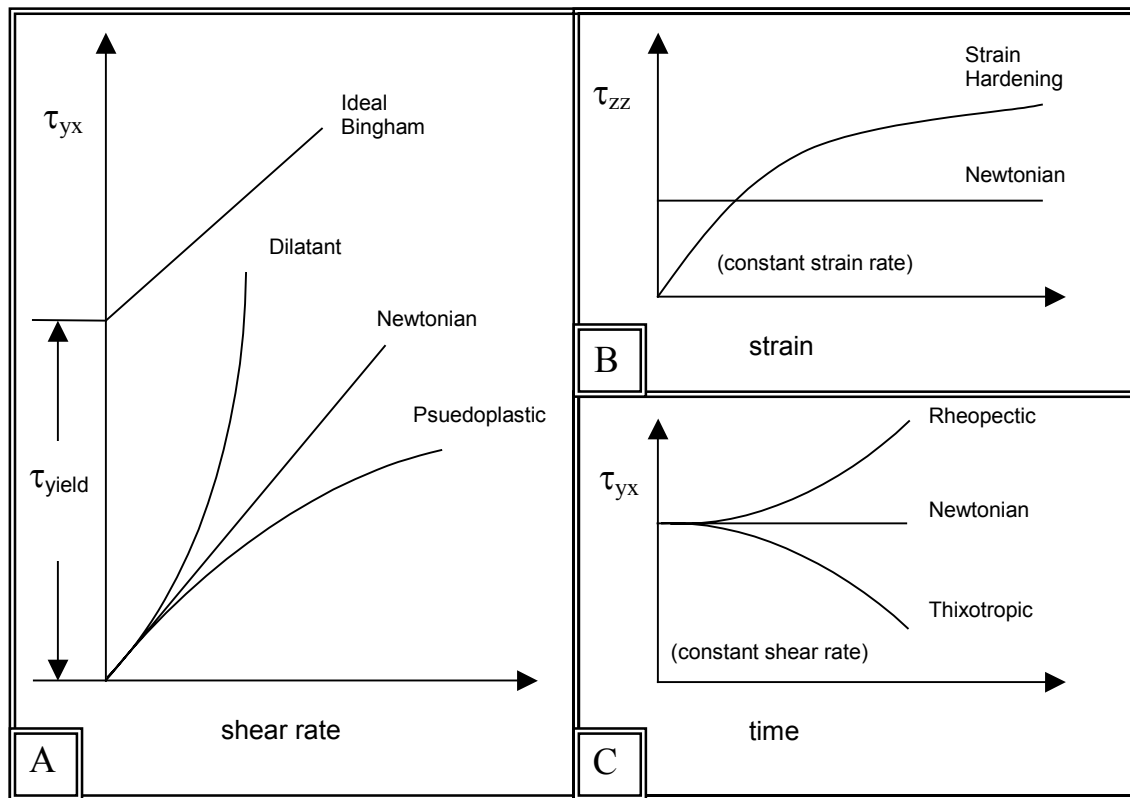


Figure 1.1 Rheological behavior of various materials: A) Shear stress vs. Shear rate; B) Elongational flow: Tensile stress vs. Strain (for constant strain rate); C) Shear stress vs. time (constant shear rate)

Another type of non-Newtonian fluid, which happens to be the type of fluid used for the current experiments, is the Boger fluid [1]. Such a fluid has a constant shear viscosity but a non-constant extensional, or elongational, viscosity, η_E . While the shear viscosity can be thought of as a fluid's resistance to shearing, the extensional viscosity can be thought of as its resistance to stretching or elongation. For a Newtonian fluid, such as water, this parameter is constant and directly proportional to the shear viscosity. A derivation of the extensional viscosity for a Newtonian liquid is given in Section 1.2.

Boger fluids are named after D.V. Boger who developed them [1]. Such fluids have been used extensively in the development of extensional rheometry because they give the investigator the benefit of isolating extensional effects from shear-induced effects in flow. The Boger fluids

used for the experiments in this thesis have an extensional viscosity that can increase by up to four orders of magnitude with strain for a given strain rate [2]. These fluids are described in detail in Chapter 3.

The word viscoelastic is often used to describe non-Newtonian fluids, and it means that the fluid has both viscous and elastic properties. Newtonian liquids, such as water, are purely viscous and after a sample of water is deformed it has no discernable tendency to regain its original shape. On the contrary, elastic solids, such as the material in a rubber band, will completely return to their original form after a moderate deformation. A viscoelastic liquid has the property that for given flow conditions, it can behave like an elastic solid, a viscous liquid, or as a combination of both, depending on the deformation rate.

1.1.1 *Flow Behavior*

Many synthetic polymers are viscoelastic, and how they behave in flow is of commercial interest because it can affect factors such as product quality and maximum production rates. The molecular structure of viscoelastic fluids gives rise to the possibility of significant elastic stresses under deformation and leading to peculiar results as the fluid begins to flow. A popular example is the Fano flow, or tubeless siphon, shown in Figure 1.2. It is common knowledge that a liquid can be siphoned from a tank using a hose, but if the liquid is viscoelastic it can continue to flow from the tank even after the hose has been removed from the free surface. This is because the stretched polymer chains result in a tensile elastic stress, i.e., they act as a series of interconnected springs and allow the fluid to transmit normal stresses along the streamlines.



Figure 1.2 The tubeless siphon. In the images above, a dyed polybutene Boger fluid is wound upwards onto a rotating spool.

Another interesting viscoelastic flow phenomenon is the Weissenberg effect, also called rod climbing, pictured in Figure 1.3. When a rotating rod is dipped into the center of a jar containing a Newtonian liquid, the fluid begins to rotate in the direction of the rod, and centripetal acceleration causes the liquid to rise at the sides and to take on a hyperbolic free surface shape. If the experiment is done with a viscoelastic fluid, elastic stresses can develop along the concentric streamlines. These concentric rings of streamlines tend to contract and squeeze fluid up near and along the axis of the rod, causing it to “climb” the rod, while the fluid level at the wall actually drops.



Figure 1.3 The rod-climbing effect. In the images above, a dyed polybutene fluid is stirred with a rotating rod. The streamlines contract around the rod and the fluid ‘climbs’ the rod.

1.1.2 *The Role of Molecular Structure*

The key to the seemingly strange macroscopic behavior of polymeric fluids lies in the molecular structure of the fluid. As the word polymer suggests, the molecules in such a substance are made of many small building blocks, or repeat units. Some common repeat units for various polymers can be seen in Figure 1.3. The chemical bonds at the union of two repeat units do allow some freedom of movement and therefore in very large molecules (the molecules in the fluids used in this thesis can be made up of 20 million repeat units) the molecule assumes what can be thought of as a more or less spherical equilibrium shape. A polymer molecule with n repeat units each of length l can be described as having a characteristic radius of gyration [3]

$$R_g \propto \sqrt{\langle nl^2 \rangle}. \quad (1.2)$$

It is deformations from this equilibrium state on the molecular scale that act to decrease entropy and result elastic restoring forces on the macroscale. When polymer is in solution, it of course interacts with the solvent and depending on the polymer concentration, it can also physically interact with neighboring molecules. The overlap concentration c^* , is defined as the polymer concentration at which the volume of molecules based on the radius of gyration exceeds the total volume. This critical concentration then varies with the molecular weight, and

$$c^* \sim M_w^{-1/2}. \quad (1.3)$$

The concentrations of the polystyrene Boger fluids used for the current experiments are below the overlap concentration.

As a solution becomes molecularly more crowded, the chances for physical interaction between molecules increases. If the fluid is then deformed macroscopically as in a flow, the chains can be deformed from their equilibrium entropic state. The situation can be thought of as being similar to pulling spaghetti from a bowl with a fork. The elastic forces that arise when the molecules are deformed act over a characteristic time scale that depends on the composition of the fluid. This time scale is referred to as the relaxation time and can be written nominally as the ratio of the fluid viscosity to its shear modulus

$$\lambda \sim \frac{\eta}{G} \quad (1.4)$$

A material with a very short relaxation time accommodates deformation rapidly may not even be considered as elastic. Because water has a relaxation time of $O \sim 10^{-9} s$, a time that cannot be discerned by humans, it is considered a purely viscous Newtonian fluid. On the contrary, some substances have a rather long relaxation time would be considered as solids. It has been reported that the lead glass in the windows of medieval cathedrals is thicker at the bottom because under gravity the glass flowed. In this case the characteristic time scale of the material would be on the order of hundreds of years.

One might hypothesize that the viscoelasticity of a material depends on the eye of the beholder. This is the idea behind the Deborah number, an extremely useful non-dimensional parameter used to evaluate fluid flow [4]. The Deborah number is a ratio of the fluid time scale, or relaxation time, to the experimental (deformation) time scale, i.e.,

$$De = \frac{\lambda}{t_{\text{exp}}}, \quad (1.5)$$

where $1/t_{\text{exp}} = \dot{\gamma}$ is also a characteristic deformation rate. For large Deborah numbers (short deformation time or large relaxation time) the material will behave primarily elastically. For small Deborah number ($De \ll 1$) the material will behave like a viscous fluid. A good example is Silly Putty; with a rapid deformation time (high De) it will bounce off the floor, but if left untouched for a few hours (low De), it will turn to a puddle on the floor. With a long enough observation time even the lead glass windows are in a low Deborah number flow and the glass looks like a liquid.

1.2 Characterization of Non-Newtonian Fluids

To completely characterize a Newtonian liquid, one must measure the surface tension, density, and shear viscosities as a function of temperature. Following the notation of Bird *et al.* [5], the equation of motion for an incompressible fluid can be written

$$\rho \frac{D}{Dt} \bar{v} = -[\nabla \cdot \boldsymbol{\pi}] + \rho \bar{g}. \quad (1.6)$$

From Newton's law of viscosity, the stress tensor, $\boldsymbol{\pi}$, is

$$\boldsymbol{\pi} = p\boldsymbol{\delta} - \mu\dot{\boldsymbol{\gamma}}, \quad (1.7)$$

where p is the hydrostatic pressure, $\boldsymbol{\delta}$ is the unit tensor, μ is the shear viscosity and $\dot{\boldsymbol{\gamma}}$ is the rate of strain tensor. The velocity components for pure elongational flow of an incompressible fluid are found from conservation of mass and written

$$V_z = \dot{\epsilon} z \quad V_y = -\frac{1}{2} \dot{\epsilon} y \quad V_x = -\frac{1}{2} \dot{\epsilon} x. \quad (1.8)$$

By definition, the rate of strain tensor is then written

$$\dot{\boldsymbol{\gamma}} = \begin{bmatrix} -\dot{\epsilon} & 0 & 0 \\ 0 & -\dot{\epsilon} & 0 \\ 0 & 0 & -2\dot{\epsilon} \end{bmatrix} \quad (1.9)$$

and for a Newtonian fluid,

$$\boldsymbol{\pi} = \begin{bmatrix} \mu\dot{\epsilon} & 0 & 0 \\ 0 & \mu\dot{\epsilon} & 0 \\ 0 & 0 & -2\mu\dot{\epsilon} \end{bmatrix} + p\boldsymbol{\delta} \quad (1.10)$$

When the fluid is being stretched, pressure gradients within the fluid arise. If a pressure gradient exists, a force balance on an infinitesimal volume element shows that it is equivalent in magnitude to its respective normal stress gradient, or

$$\frac{\partial p}{\partial x} = -\frac{\partial \tau_{xx}}{\partial x} \quad (1.11)$$

Integrating Equation 1.11, and using taking the ambient pressure as the constant of integration, it is found that

$$p = p_0 - \tau_{xx} \quad (1.12)$$

It then follows from Equation 1.10 that

$$\pi_{zz} - p_0 = \tau_{zz} - \tau_{xx}. \quad (1.13)$$

The term on the left side of Equation 1.13 is exactly the pressure required to stretch the fluid in the z-direction. The definition of the extensional viscosity is

$$\eta_E \equiv \frac{\tau_{zz} - \tau_{xx}}{\dot{\epsilon}}, \quad (1.14)$$

and from Equation 1.10 it is seen that the extensional viscosity is independent of strain rate and proportional to the shear viscosity, i.e.,

$$\eta_E = 3\mu. \quad (1.15)$$

This result was found by Trouton in 1906 in experiments using mixtures of pitch and tar [6]. It should be noted that there is an analogous result in solid mechanics, i.e., for an incompressible material ($\nu = 0.5$) the elastic modulus is three times the shear modulus, or

$$E = 3G \quad (1.16)$$

For non-Newtonian fluids, material characterization is not so simple. There is no concise, all encompassing constitutive equation relating the rate of strain to stress, and the extensional viscosity can be very large in proportion to the shear viscosity. Many constitutive models exist, but unfortunately they tend to be much more complicated than the model put forth by Newton and they are often fluid and flow specific. Nevertheless, such models can be very useful in designing commercial processes. Non-Newtonian constitutive equations often incorporate data from shear and extensional rheometry to predict fluid flow behavior. For polymer solutions such as those used for the current experiments, these fluid properties can be measured using the devices

described in paragraphs 1.2.1 and 1.2.2. More detailed information concerning non-Newtonian fluids and fluid constitutive models can be found in the reference by Bird *et al.* [5], [7].

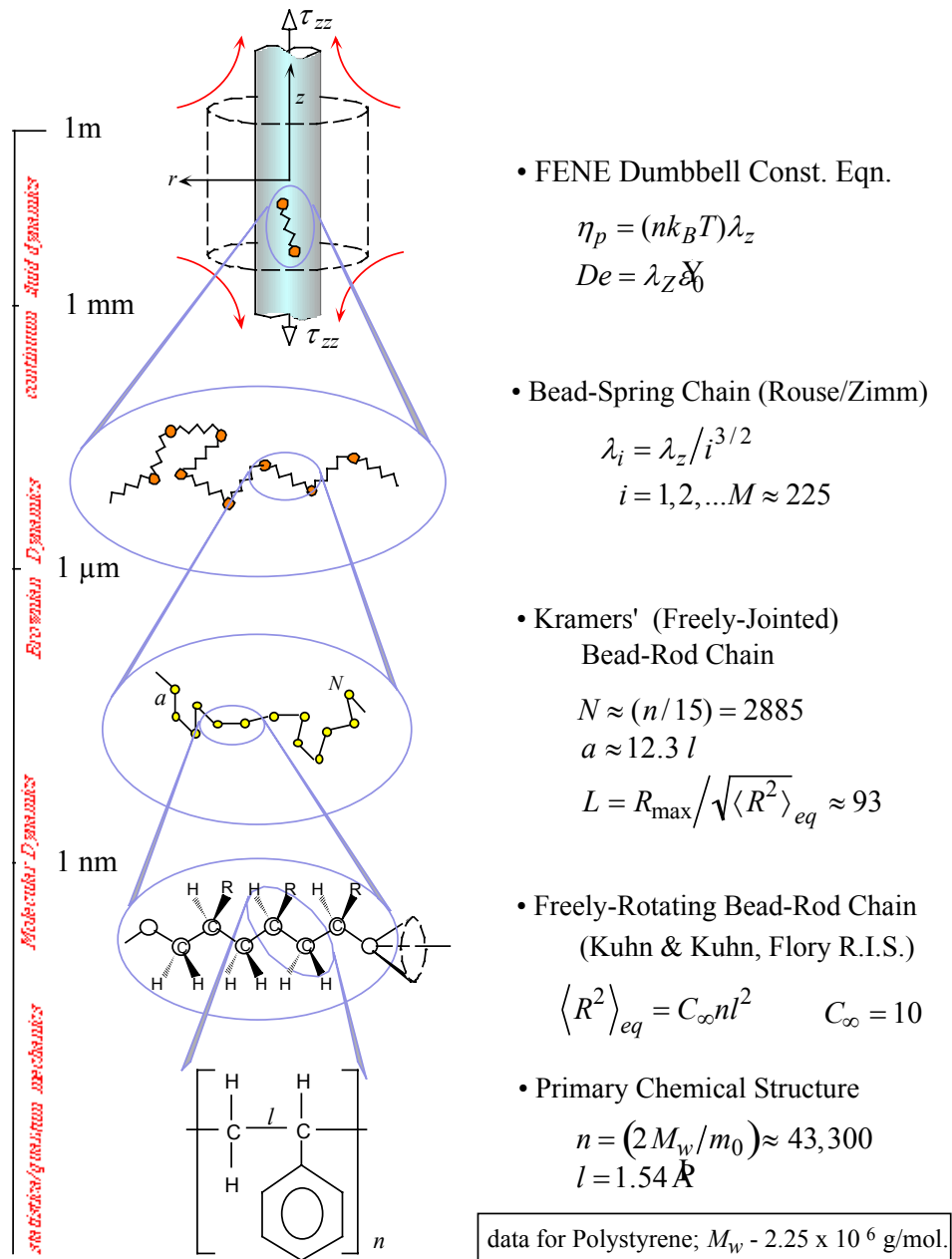


Figure 1.4 A progressive ‘course-graining’ of structural information. Moving up the diagram from the bottom, statistical simplifications are made in the consideration of polymer solutions. The diagram includes the major assumptions used in various constitutive models.

1.2.1 Shear Rheometry: Cone and Plate Rheometer

There are many ways to measure the shear viscosity of a fluid. The Couette viscometer uses concentric cylinders to create a small-gap shear flow while measuring torque to deduce viscosity. A falling ball viscometer relates the speed at which a sphere falls under gravity in a fluid to the shear viscosity of the fluid. Parallel plate and the cone-and-plate type rheometers (see Figure 1.5) are ideal for use with non-Newtonian fluids because they only require a small sample volume, loading of the sample is achieved with relative ease, and the design can be made robust enough to handle the high viscosities typical of such fluids. In addition, by applying an oscillatory torque or strain, they can measure the storage and loss moduli functions, G' and G'' , which can be taken as a measurement of the viscoelasticity of a fluid [5]. Of these two similar geometries, the cone-and-plate is preferable because it provides a constant shear rate throughout the sample (the shear rate is defined as the ratio of the plate or cone speed at a given radial position to the gap thickness at that position). The cone-and-plate device consists of a small angle cone that rotates just above a flat plate, thus the shear rate is governed purely by the cone angle and the rate of rotation. Cone-and-plate rheometers can measure viscosity either by measuring torque for a given rotation rate (strain-controlled), or by measuring strain for a given applied torque (stress-controlled). Modern commercial cone-and-plate rheometers are able to measure shear viscosity as a function of strain rate and temperature as well as implement the oscillatory profile for viscoelasticity measurements. The shear rheometry of the test fluids used in this thesis was carried out using a cone-and-plate rheometer and is described in detail in Chapter 3.

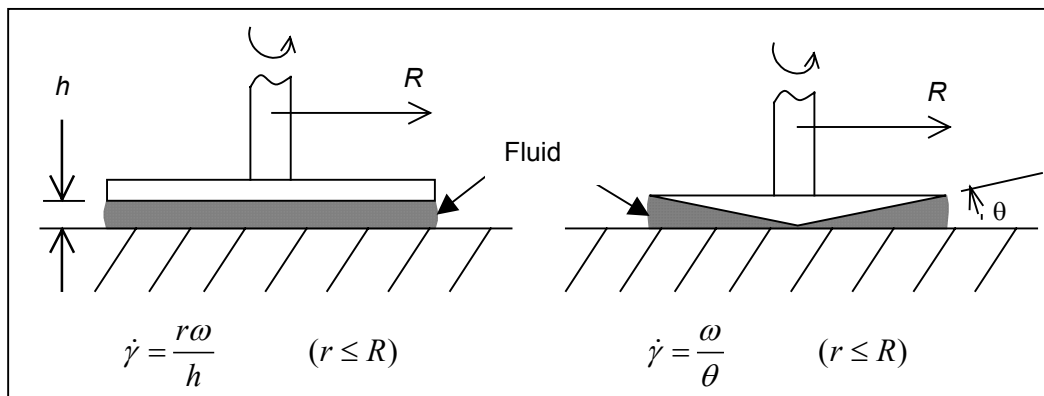


Figure 1.5 The parallel plate (left) and cone-and-plate (right) geometries.

1.2.2 *Extensional Rheometry: Filament Stretching Rheometry*

It was noted previously in this chapter that large extensional viscosities are possible in viscoelastic fluid flows. Since many commercial polymer processes involve extensional flow, the measurement of transient extensional viscosities of polymeric liquids has received considerable research attention in recent years. But although flows with extensional components are common, it is difficult to achieve ideal shear-free flows in the laboratory, especially for more mobile liquids such as polymer solutions. Several extensional viscometers have been developed, but the difficulty in measuring this fluid property is perhaps best shown by Figure 1.6, which shows the widely disparate results of a round-robin study among several researchers using a common test fluid and various measurement devices that was published in 1990[8].

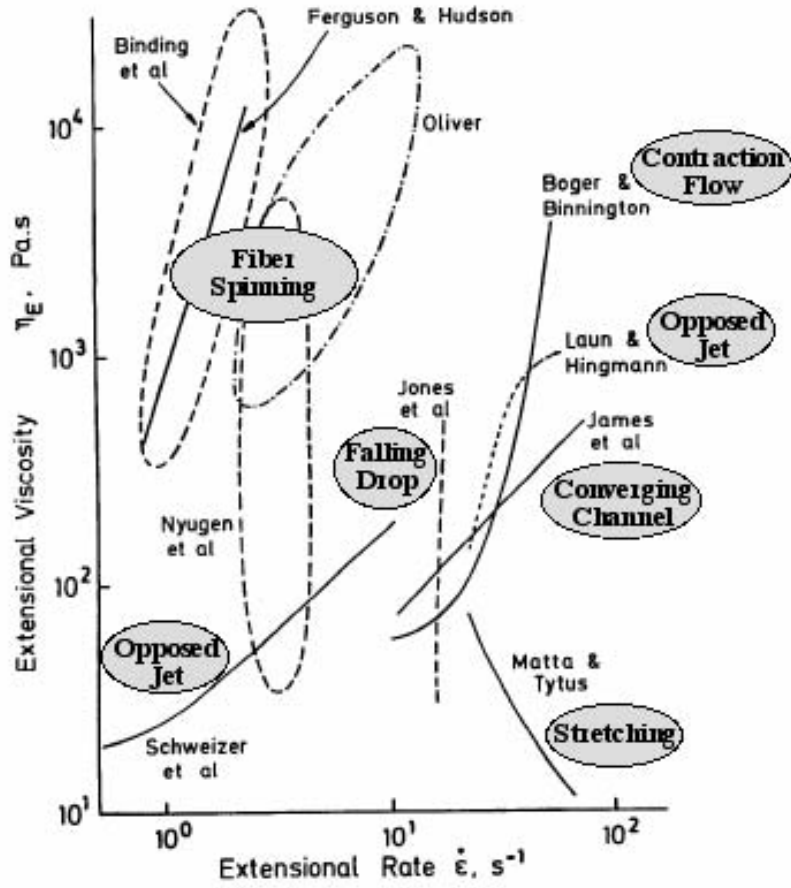


Figure 1.6 Apparent extensional viscosity measured in various devices for a single common test fluid, M1. Reproduced with permission from [9]. Copyright 1994 Elsevier.

Because of the important role of extensional viscosity in polymeric fluid flows, and in light of the discord in measurements reflected by the 1990 study, filament stretching extensional rheometry has developed over the past decade to become a viable measurement technique. The filament stretching rheometer (see Figure 1.7) in its modern form was first implemented by Sridhar [10] and consists of two cylindrical plates that can be separated at a programmable rate to stretch a small fluid sample and create a slender filament [11]. The plates move apart at an exponential rate, providing a nearly constant rate of deformation and a nearly shearfree flow at the filament midpoint. If the midpoint filament diameter and the tension in the filament are also measured, a measurement of the transient extensional viscosity can be derived. Neglecting inertial and axial curvature terms, the force balance proposed by Szabo [12] is written

$$\langle \tau_{zz} - \tau_{rr} \rangle = \frac{F_z(t)}{(\pi R_{mid}(t))^2} + \frac{1}{2} \frac{\rho g V}{(\pi R_{mid}(t))^2} - \frac{\sigma}{R_{mid}(t)}, \quad (1.17)$$

where F_z is the measured axial force, R_{mid} is the measured mid-filament radius, and V is the fluid sample volume. The rightmost two terms account for the effects of gravitational sagging and surface tension respectively. It should be noted that for low strain rates fluid sagging due to gravity can be appreciable and elimination of this sagging is the premise of NASA's zero gravity Extensional Rheometry Experiment (ERE) [13]. The term on the left side of Equation 1.17 is the normal stress difference in extensional flow and the transient extensional viscosity can be found by

$$\eta_E^+ = \frac{\langle \tau_{zz} - \tau_{rr} \rangle}{\dot{\epsilon}_0}, \quad (1.18)$$

where $\dot{\epsilon}_0$ is the imposed constant strain rate. The success of the filament stretching extensional rheometer is made clear by the recent results of a study involving four different laboratories using common test fluids and four independently designed filament stretching rheometers. The results of the extensional viscosity measurements from the participants in this study are in remarkable agreement [14]. The transient extensional viscosities of the test fluids used for the current experiments have been measured by Anna [2] using the filament stretching rheometer at MIT and are discussed in Chapter 3. For further information on filament stretching rheometry, the reader may refer to a recent review of the subject by McKinley and Sridhar [15].

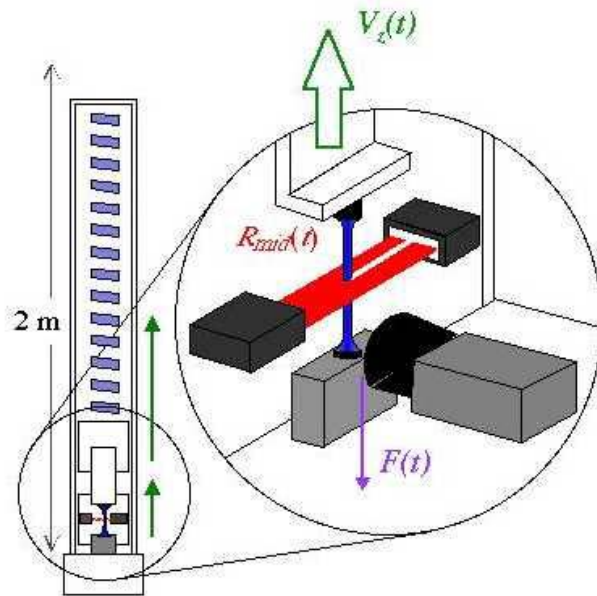


Figure 1.7 A solid model of a Filament Stretching Extensional Rheometer (FISER)

1.3 Pressure-Sensitive Adhesives (PSAs)

The word adhesive is a general term given to any material used to bond two surfaces together. Since ancient times, people have used naturally occurring adhesives such as pinesap and tar for various construction purposes. In the past century, as the number of manufacturing applications has blossomed, so has the need for adhesives to fit these applications. Accordingly, adhesives have been designed for nearly every imaginable application, ranging from fixing labels on beer bottles to the fastening of the insulation tiles on the space shuttle. We rely on adhesives to mail our letters, catch flies, and to keep our shoes from falling apart. In modern automobiles, adhesives have become ubiquitous, taking the place of traditional fastening techniques such as riveting and welding in numerous places.

Today there are many types of adhesives. Some adhesives require a chemical reaction to set. Others require activation by UV light or the evaporation of a solvent to cure. Pressure-sensitive adhesives are an important class of adhesive used for tapes, postage stamps, labels, and many other applications. The Pressure Sensitive Tape Council has defined these adhesives as follows:

Pressure sensitive is a term commonly used to designate a distinct category of adhesive tapes and adhesives which in dry (solvent free) form are aggressively and permanently tacky at room temperature and firmly adhere to a variety of dissimilar surfaces upon mere contact without the need of more than finger or hand pressure. They require no activation by water, solvent, or heat in order to exert a strong adhesive holding force toward such materials as paper, cellophane, and glass, wood, and metals. They have a sufficient cohesive holding and elastic nature so that, despite their aggressive tackiness, they can be handled with the fingers and removed from smooth surfaces without leaving a residue. General trade usage by leading tape manufacturers does not sanction extension of the term “pressure sensitive” to embrace tapes and adhesives merely because they are sticky (e.g., fly papers) or merely because they cohere or adhere to a particular type of surface (e.g., self-sealing envelopes); and terms other than “pressure sensitive” should be used to avoid confusion [16]

Although much empirical data is available, as with the majority of non-Newtonian fluids, a comprehensive theory of PSAs is lacking. Rules of thumb such as the *Dalquist criterion*, which states that a good pressure-sensitive shall have an elastic modulus below around 0.2 MPa (it must be low enough to achieve good surface contact) are still in use [17] although recently great strides

have been made in understanding the relation of molecular architecture and bulk material properties to adhesive performance [18], [19], [20]. The commercial importance of pressure-sensitive adhesives underlies the quest for a better theoretical understanding of these materials because such an understanding will enable better adhesive performance predictions as well as the design of better PSAs.

1.3.1 *Literature Review*

The behavior of a pressure-sensitive adhesive depends on many factors. Changing the chemical composition, molecular weight, or molecular structure of the adhesive can alter adhesion properties [21], [18]. For example, under large strain, a branched molecule can have more interactions with neighboring molecules than a linear molecule of the same size, thus influencing the viscoelasticity and extensional viscosity of the material. Surface properties also play a very important role in the strength of an adhesive bond [22], [23], [24], [25]. A PSA will not have the same debonding energy for a highly polished stainless-steel surface as for a roughened surface of the same material. This is perhaps best exemplified by considering the non-stick backing, or ‘release paper’, used for tapes and decals. An indirect consequence of surface roughness is surface cavitation. On the microscale, even a surface that feels smooth looks very rough microscopically and contains many pores. These pores can trap air and provide nucleation sites for cavitation bubbles [26]. Stemming from such nucleation sites or from material defects, cavitation can occur in a purely viscous liquid due to a negative hydrostatic gage pressure [27], or in an elastic or viscoelastic material because the growth of cavities reduces elastic stresses [28]. In agreement with the results first observed by Gent for elastic materials [29], [30] and later by Kaelble for viscoelastic liquids [31], the experiments in this thesis indicate that cavitation occurs at specific negative internal pressure for a given fluid and geometry.

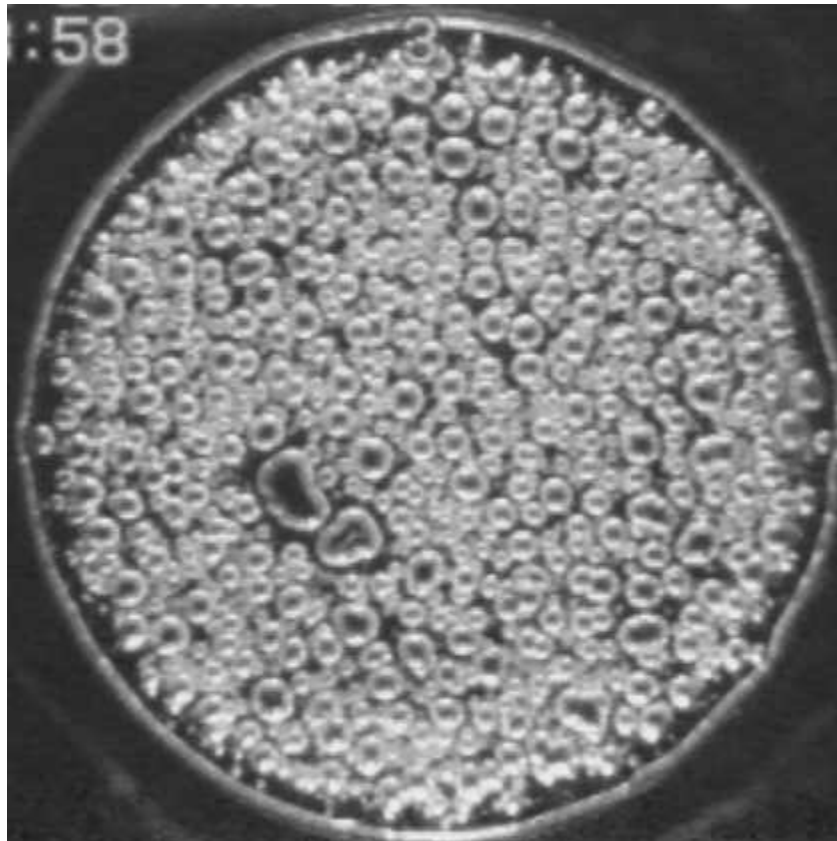


Figure 1.8 Cavitation in a 200µm layer of a pressure-sensitive adhesive during a probe-tack experiment (viewed from beneath). Note the incomplete wetting of the probe due to misalignment. Photo courtesy of A. Chiche & C. Creton.

When an adhesive joint is strained, fibrils, or thin strands of adhesive that bridge the two surfaces, can form (see Figure 1.9). These fibrils can sometimes be seen with the naked eye when an adhesive is removed from a solid surface and have long been recognized in adhesive peeling tests (see Figure 1.9) [32], [33] and probe-tack tests (see Figure 1.10) [34], [35], as well as in polymer films in roll nip experiments [36]. The stretching of these fibrils can account for a large majority of the external work required to debond two surfaces [37], [38]. The extension of such fibrils is primarily an elongational flow and the fibrils strain harden by the same molecular mechanism that causes the large extensional viscosities in the polymer solutions mentioned previously. A theory relating extensional rheology to adhesive strength was first suggested by Gent & Petrich [30] and was later implemented with some success by Connelly [39]. More

recently, this idea has been investigated further by Good & Gupta for ideal fibril elongation [40] as well as by Piau *et al.* [24] and by Christensen & McKinley [41] in the peeling geometry.

Two recent studies on model pressure-sensitive adhesives by Zosel [38] and Lakrout *et al.* [37] utilize the probe-tack experiment to investigate the onset and development fibrils and their effect on tack. In the latter of these studies, it was shown that fibrils can form as the result of longitudinal growth of cavitation bubbles. In the current experiments it is shown that fibrils can result not only from cavitation, but also from an elastically induced flow instability, and that the development of such fibrils can be heavily influenced by a viscous free-surface flow instability which is described in the following paragraphs.

For highly confined geometries, viscous forces predicted by Reynold's lubrication theory can also play a role in the force required to debond two surfaces [42], [21]. In small gaps, this lubrication flow can induce a three dimensional axisymmetric fingering instability similar to the Taylor-Saffman fingering instability [43] observed in Hele-Shaw cells [44] when a less viscous fluid displaces a more viscous one. The fingering phenomenon was long observed in the oil industry before it was physically explained in the classic paper by Saffman & Taylor. When oil was pumped from a field it was often discovered that water from surrounding areas would reach the pump well before the known oil pocket had been exhausted. Alternatively, when natural gas or air is pumped into the ground at some distance from the well in order to drive the oil out, the same problem can occur. It is now known that because the air and water are less viscous than the oil, an interfacial instability is prone to occur as the oil is removed and a finger of air or water is able to penetrate the oil pocket and reach the well, stymieing the drilling operation. Paterson later adapted the theory to the axisymmetric case in which the more viscous fluid is sucked from a hole in the Hele-Shaw cell [45], which is perhaps closer to the physical problem. Viscous fingering in the axisymmtric case as well as in the cases of converging and diverging channels was more recently investigated by Thome *et al.* [46]. It should be briefly noted that the inverse case of the axisymmetric fingering problem, in which a gas is injected in a Hele-Shaw cell to create a point source, has been studied by numerous investigators a well, however the investigators seem interested primarily in the tip splitting and fractal nature of the fingering [47], [48], [49], [50].

In addition to fingering in a Hele-Shaw cell, similar meniscus instabilities have been observed when a thin layer of liquid is spread with a blade or roller [51] or when a fluid exits two counter-rotating rollers [52]. By nearly the same mechanism, viscous fingering has also been observed in the peeling geometry [27]. Viscous fingering can be considered to result when forces

due to viscous effects overcome capillary forces, a balance that can be described by the capillary number exceeding a critical value,

$$Ca = \frac{\mu V_r}{\sigma} > Ca_{crit},$$

where μ is the shear viscosity, V_r is the bulk radial velocity, and σ is the surface tension. Following lubrication theory for reverse squeeze flow, decreasing the initial aspect ratio and increasing the separation rate both act to increase the fluid radial velocity (see Chapter 4 for a derivation of this). Accordingly, in the current experiments, viscous fingering is observed for sufficiently small plate separation distance and for sufficiently large stretching rates; i.e., above a critical capillary number. This phenomenon has been theoretically investigated for the Newtonian case by Shelley *et al.* [53] and has recently become of interest in the study of the tackiness of adhesives [54]. A recent publication by Thamida *et al.* investigates the effect of viscous fingering on the work of adhesion by using a constant force to separate two plates joined by Newtonian liquid film while measuring the strain as a function of time [55]. In axisymmetric probe tests of soft PSAs by Crosby *et al.* [56] and by Shull *et al.* [57] the occurrence of Saffman-Taylor-like fingering has been reported. In separate publications, these authors have noted similar fingering instabilities in purely elastic materials [58], [59], which appeared very similar to the fingers seen by Spiegelberg & McKinley in extensional rheology tests of viscoelastic dilute polymer solutions at large strains [60]. Since the Saffman-Taylor instability is due to a viscous flow phenomenon, it cannot be the cause of both instabilities. The experiments in this thesis show that there are two separate and distinct fingering instabilities and that one results from elasticity and the other from viscous flow. Each of the instabilities studied in this thesis (cavitation, elastic and viscous fingering) can heavily influence fibrillation, therefore influencing debonding energies. These instabilities depend on the adhesive material, geometry, and debonding speed and are discussed in Chapter 4.

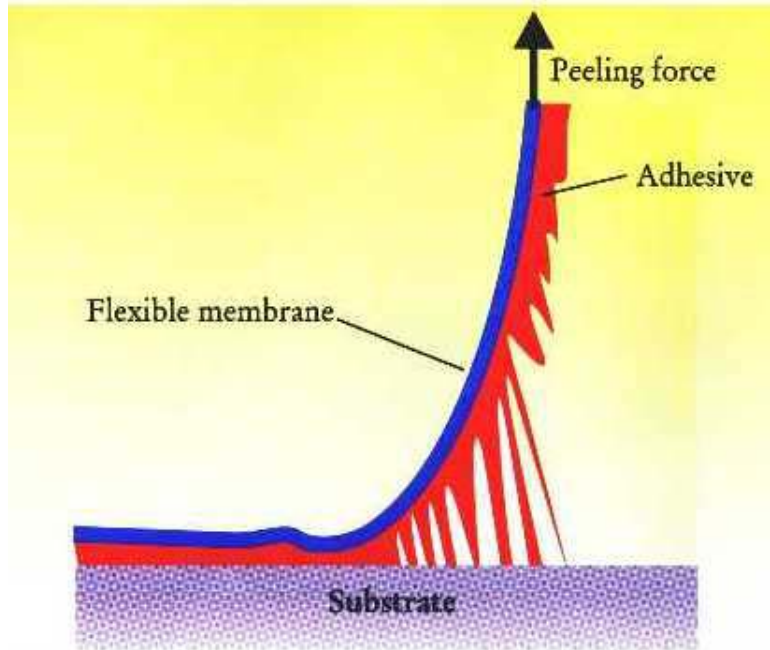


Figure 1.9 In the Peel Test, an adhesive layer is peeled from a rigid substrate, often resulting in the formation of fibrils. Reproduced with permission from [21]. Copyright 1999 American Institute of Physics.

1.3.2 *The Probe-Tack Test*

Quantifying the performance of a PSA can be done experimentally by measuring the energy required to separate two adhesively bonded surfaces. In practice, there are several methods of doing this, but perhaps the most common is the peel test (see Figure 1-8). In this test, a flexible membrane bonded to a rigid substrate with a PSA is peeled at a constant speed and peel angle, while the peel force is measured [61], [32]]. Another type adhesive test is the tack test. By definition, tack is the ability of an adhesive to form a bond of measurable strength immediately upon contact [62]. The tack tests are, in simple terms, a quantification of what we can do by separating our thumb and forefinger after putting a drop of liquid between them. Most people would agree that pancake syrup is a tacky fluid, while water is not. The tack test uses a rigid probe that can be retracted uniaxially from an adhesive layer at a known rate while measuring the maximum axial force. The JKR tack test uses a spherical indenter to probe the adhesive layer, testing for tack. The name comes from the well-known JKR adhesion theory (Johnson-Kendall-Roberts) [63], which is based on a modification of the Hertz contact theory [64] for soft substrates and is heavily relied upon in the testing of PSAs [57]. If instead, a flat cylindrical

indenter is used, the test is termed the probe-tack test [65], and although alignment becomes more difficult (see Figure 1.7), the analysis benefits from a simpler geometry. Although the probe-tack test was developed some time ago [66], [34], it seems to have not become a popular method of testing PSAs until after the important study on adhesion and tack by Zosel [67], who apparently was the first to use the test to measure force as a function of distance and deduce a work of adhesion. For the study of adhesive breakup and the development of fibrils, the axisymmetric probe tests are far superior to the peeling tests because they provide a more homogeneous elongation of the whole area of contact. With the peel test, the whole spectrum of strain is included in the force measurement, providing only an average sense of the debonding mechanisms. Probe-tack tests provide a way to quantify fibril stress through the entire evolution of the strained joint, from rest to fracture. In addition, if a clever modification to the experiment to allow for viewing the sample from the axial direction is made, the development of fibrils as well as cavitation in the adhesive layer can be visualized and matched to the strain curve and corresponding force.

1.4 A Modified Probe-Tack Experiment

The ASTM standard (D2979-95) for the probe tack-test specifies that a flat, 5mm diameter stainless steel probe with a surface roughness between 250 and 500 nm (rms) be brought into contact with a substrate of pressure-sensitive adhesive and then moved away in the normal direction at a constant velocity of 10mm/s. The dwell time, dwell load, and maximum force upon probe retraction are recorded for each experiment. Although the standard probe-tack test only calls for the measurement of a maximum force, the experiment can easily accommodate the measurement of force as a function of strain, allowing the experimenter to gather more useful information. Specifically, the effects of fibril formation and elongation on the debonding energy can be investigated. This method also allows for another adhesive measurement, the work of adhesion, defined as

$$w_a = \frac{1}{A} \int F(z) dz, \quad (1.19)$$

which is the integral of the axial force over the distance traveled by the probe, divided by the area of contact [67]. If the experiment is coupled with video imaging even more useful information can be gleaned from the test. For example the strain or load at the onset of fibrillation or cavitation can be recorded.

The experiments detailed in this thesis use two model viscoelastic polystyrene fluids, both well characterized in shear and extensional flow, to investigate various flow instabilities and their effect on the work of adhesion. Because the test fluids used fail cohesively, leaving a residue on the probe, they cannot be considered as true pressure-sensitive adhesives. However, the fluids do exhibit the nearly the same fingering instability phenomena as those seen by other researchers in the testing of pressure-sensitive adhesives, making them ideal to further probe the instabilities from a fluid mechanics viewpoint. In addition to the polymeric liquids used as test fluids, various model Newtonian fluids of similar shear viscosity were used to further probe the viscous fingering instability.

The experiments were performed by employing a modification of the standard probe-tack test and are described briefly below and in more detail in Chapters 2 and 4. For the majority of the experiments, an exponential velocity profile was used rather than the constant speed called for in the ASTM standard. The explanation for this deviation is that an exponential velocity profile provides a nearly constant strain rate and more uniform kinematics since the flow in the fibrils is primarily elongational. If L is the instantaneous sample length, then the strain rate is defined as

$$\dot{\epsilon} \equiv \frac{1}{L} \frac{dL}{dt} . \quad (1.20)$$

For a constant strain rate, as is desired for rheological measurements, separation of variables and integration results in a length that increases exponentially in time, or

$$L(t) = L_0 e^{\dot{\epsilon}t} , \quad (1.21)$$

where L_0 is the initial sample thickness. It follows from Equation 1.21 that the velocity is also an exponential function of time, and

$$V(t) = \frac{dL}{dt} = L_0 \dot{\epsilon} e^{\dot{\epsilon}t} . \quad (1.22)$$

By inserting Equations 1.21 and 1.22 into Equation 1.20, it can be seen that an exponential stretching profile results in a strain rate that is constant in time.

When a linear velocity profile is implemented in a stretching experiment, the same definition of strain rate from Equation 1.20 applies, but the strain rate is obviously not constant. For constant stretching velocity V_0 , the length as a function of time must be

$$L(t) = L_0 + V_0 t , \quad (1.23)$$

so the strain rate decreases as a hyperbolic function of time, or

$$\dot{\epsilon}(t) = \frac{V_0}{L_0 + V_0 t}. \quad (1.24)$$

If the flow in the fibrils is primarily elongational, it is clear that the use of an exponential velocity profile for stretching experiments provides more uniform kinematics.

As mentioned already, the apparatus incorporates the ability to visualize the flow near the rigid endplates. This modification required the use of glass as the endplate material, rather than the standard stainless steel. A final deviation from the standard test is another result of the liquid nature of the test materials. In the standard, a probe is to approach an idealized infinite layer of adhesive and remain there under some dwell load and time. In these experiments rather than using a substrate, a thin fluid layer was loaded between the two equal-sized endplates creating a cylindrical fluid sample, and the test was started after the fluid was allowed to relax so that there were no residual stresses in the material.

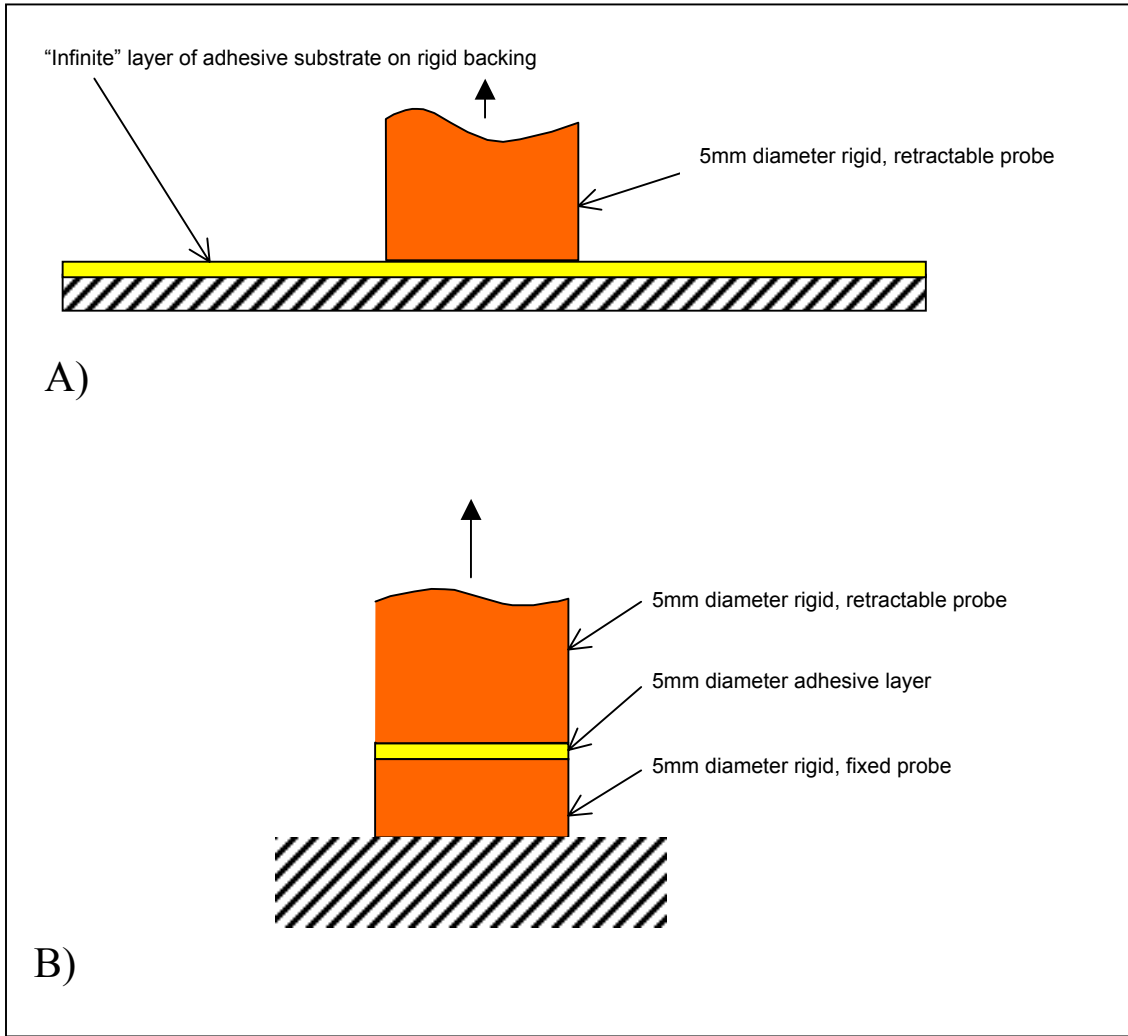


Figure 1.10 Sketch comparing; A) The conventional probe-tack geometry, and; B) The geometry of the current experiments

1.5 Summary

The design of better adhesives depends not only on an understanding of materials at a molecular level, but on physical properties and deformations of the adhesive at the bulk level as well. Most adhesives are non-Newtonian fluids at some point in their lifecycle, and therefore a fluid mechanics approach to understanding many adhesive problems is logical. In this thesis, flow instabilities such as cavitation, fibrillation, and viscous fingering (all phenomena that are common in the debonding of many adhesives) are investigated experimentally using such an approach. The

effect of these instabilities on the adhesive performance can be dramatic and it is hoped the contribution of this work will further advance the understanding of adhesive debonding mechanisms and therefore lead to better engineered adhesives.

Chapter 2 Experimental Setup and Testing Method

2.1 Experiment

The experiment utilizes an adaptation of the filament stretching rheometer to implement a modification of the probe-tack adhesion test for the purpose of investigating endplate instabilities in mobile viscoelastic polymer solutions. The standard probe-tack test, which was discussed briefly in the last chapter, incorporates a flat probe that can be retracted from an adhesive substrate at a known rate while recording the maximum normal load. The current experiment deviates from the probe-tack test in the following ways: 1) Due to the mobile nature of the test fluids, a cylindrical sample having the same 5mm diameter as the probe is used rather than an infinite substrate of adhesive material (see Figure 1.10); 2) The velocity profile is exponential in time, rather than the constant 10 mm/s back-off velocity specified by ASTM D2979-95. The aim of using an exponential velocity profile is to provide a constant strain rate within the elongating sample. This is a fundamental requirement in extensional rheometry and in the current case, it is required in order to induce a strongly strain hardening elastic response in the viscoelastic test fluids; 3) The test probe material is glass rather than the polished stainless steel called for by the standard. This is because the implementation of the optical device for viewing the sample from beneath the endplate required that a transparent material be used for the lower endplate. A matching glass optical window was used for the upper endplate to ensure flow symmetry at low plate separation distances and to provide symmetrical conditions for the occurrence of adhesive failure at the end of stretching.

In contrast to the standard probe-tack test, in which only the maximum axial force on the probe on the probe is recorded, the axial force is measured over the course of the whole experiment in the current test setup. This allows for a quantifiable investigation of the stretch and the development of any elastic stresses. Recording the tensile force as a function of strain also permits the calculation of the work of adhesion [67], written

$$w_a = \frac{1}{A} \int F(z) \cdot dz . \quad (2.1)$$

In addition, the test has been further modified so that the fluid sample can be viewed simultaneously from the side and from beneath via the optical apparatus described in the next section.

2.1.1 *Flow Geometry and Experimental Setup*

The fluid sample is initially in the shape of a cylindrical plug and is held between two rigid circular endplates by surface tension (see Figure 2.1). The upper endplate is attached to the linear motor described in Section 2.2, and can move away from the stationary and mechanically isolated lower endplate at a programmable rate. At the start of an experiment the plates begin to separate, thus deforming the fluid sample. Depending upon the initial experiment parameters, a slender fluid filament may form. If a stable filament does develop, then the flow near the filament midpoint will be a nearly pure uniaxial extensional flow if an exponential profile is chosen [14]. This shearfree flow is the key to the success of filament stretching rheometry. With certain initial conditions, however, flow instabilities can either prevent the ideal filament from developing, or if it does develop, cause it to become unstable [60]. Such instabilities are the topic of this thesis and are discussed thoroughly in Chapter 4.

For stretching experiments, an initial aspect ratio can be defined as the ratio of initial sample height to sample radius, or $\Lambda_0 \equiv L_0 / R_0$. In typical extensional rheometry experiments $\Lambda_0 \sim O(1)$, and initial sample radii are no more than a few millimeters [14]. Larger samples would provide bigger extensional forces and perhaps more accurate measurements, however if the sample height is too large gravity may cause the sample to ‘slump’. This effect is quantified by the Bond number, which compares surface tension to gravitational forces and is written

$$Bo = \frac{\rho g L_0^2}{\sigma}. \quad (2.2)$$

For large Bond numbers, i.e., $Bo > 1$, gravitational forces are dominant and cause the sample to sag or even fail cohesively before the stretching even starts [12]. Such sagging can be problematic during experimental rheometry experiments, and it serves as the basis for NASA’s zero-gravity Extensional Rheology Experiment (ERE) [13].

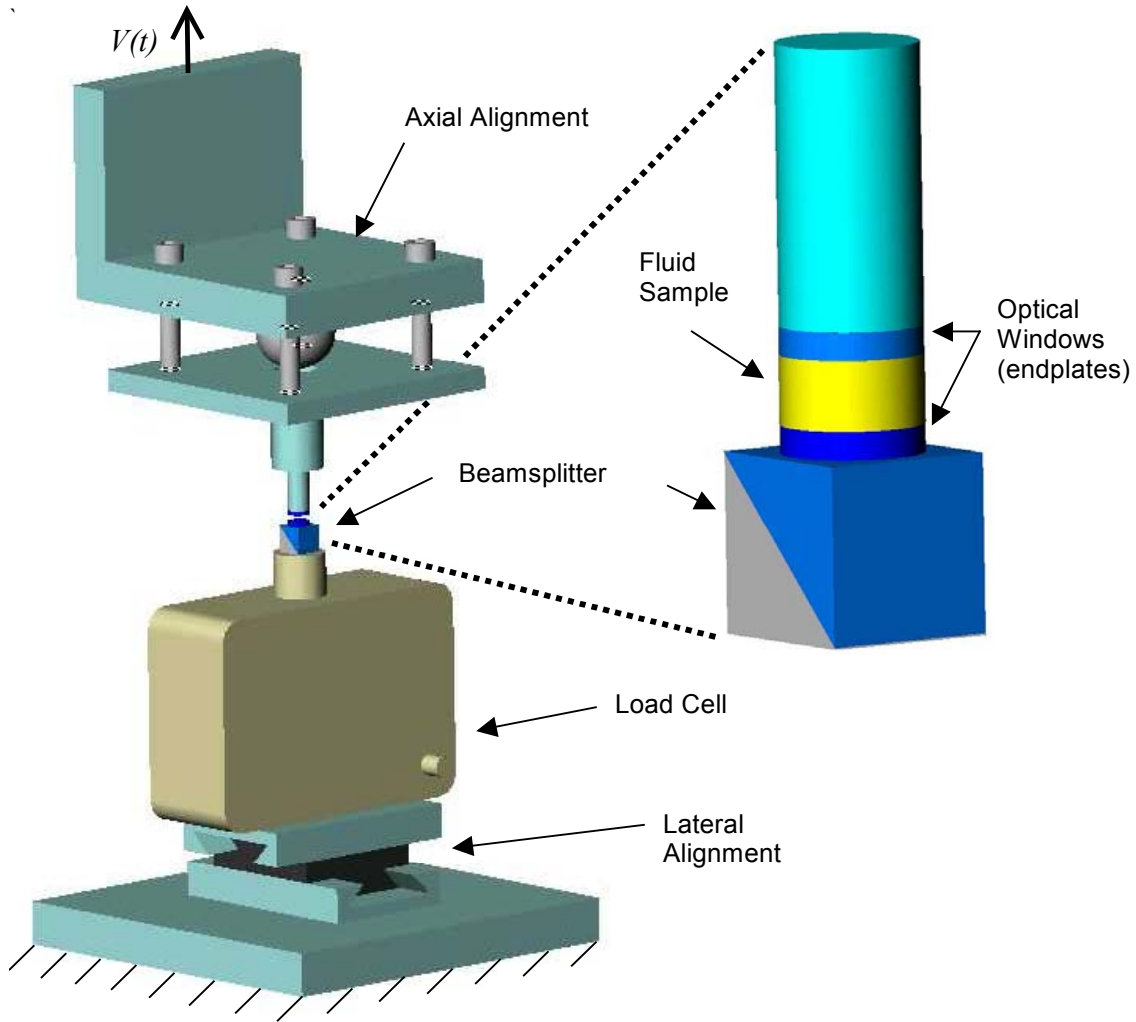


Figure 2.1 Sketch of upper and lower endplate assemblies showing alignment mechanisms and load cell. The upper endplate assembly is attached to the linear motor. The lower endplate assembly is isolated from the motor and remains stationary.

There is also a limit on how small the aspect ratio can be. A highly confined sample ($\Lambda_0 \ll 1$) can lead to a viscous fingering instability similar to that described by Taylor & Saffman [43]. If the aspect ratio is further reduced, cavitation may occur due to a reduced pressure within the fluid [31] when stretching begins. Cavitation and fingering instabilities have been observed in probe-tack testing of adhesives as well [56]. In the current experiments, the test fluids were stretched at aspect ratios as large as 0.40, and as small as 0.04. These experiments span a range of

sample thicknesses that bridge the gap between those used in probe-tack testing and those used in extensional rheology experiments (see Table 2.1).

	Aspect Ratio	Sample Thickness (mm)
Extensional Rheometry	$\Lambda_0 \sim O(1)$	$1.5 < L_0 < 3.5$
Probe-Tack Test	$0.01 < \Lambda_0 < 0.20$	$0.025 < L_0 < 0.500$
Current Experiments	$0.04 < \Lambda_0 < 0.40$	$0.10 < L_0 < 1.00$

Table 2.1 Comparison of aspect ratios, or degree of confinement, used in extensional rheometry and probe-tack tests

2.1.2 *Sample Preparation and Loading*

The polystyrene fluids used in the current experiments have been characterized in both shear and extensional flow by Anna [2], and were tested in shear flow by the author just prior to the current experiments in order to check whether the viscometric properties of these fluids had significantly changed since the experiments by Anna (see Chapter 3). Although the fluids are very viscous, they are mobile enough to be loaded using a syringe system driven by compressed air (EFD Model 800). The procedure for loading a test sample first involves cleaning, then aligning and zeroing the endplates (see Figure 2.1). After the plates have been zeroed, the motor moves to the programmed plate separation on command, and the no-load voltage of the load cell is recorded. Next, the upper endplate is backed-off by hand using a micrometer thread and an appropriate-sized drop of the fluid sample is loaded onto the lower endplate using the pressurized syringe. The micrometer is then slowly adjusted back to its original position, as indicated by the vernier scale, which has a resolution of 1 μm . Care must be taken to avoid visible air cavities or stray dust particles from entering the fluid when loading because they can disturb the flow or act as seeds for unwanted cavitation bubbles during the experiment. In addition, since the fluid sample volumes used in these experiments are rather small, it is crucial to ensure that the proper amount of fluid has been loaded. This is done visually using live video imaging from the CCD cameras. After the fluid has been loaded, the sample is permitted to relax for at least three fluid relaxation times before the experiment begins.

2.1.3 *Temperature*

The viscoelasticity of the fluids used in these experiments is very sensitive to changes in temperature (see Chapter 3). Accordingly, the temperature of the fluid must be carefully monitored in order to account for such changes during data analysis. Due the laboratory environment and the design of the filament stretching rheometer, the fluid temperature could not be controlled by any other means than the thermostat in the laboratory and variations in temperature of 2-3 °C were encountered over the course of a day. In each experiment, just prior to stretching, the temperature of the endplate at the edge of the fluid was measured using a digital thermometer (Omega Model HH200 with Al/Cr thermocouple) and recorded for later data processing.

2.2 **FISER II Filament Stretching Rheometer**

The FISER II filament stretching rheometer (see Figure 1.7) was built by Anna and has proven to be a reliable and robust device in past research in the Non-Newtonian Fluid Mechanics Lab at MIT [2], [68]. This machine utilizes two programmable linear brushless DC motors to stretch fluid samples. The top endplate is attached to the upper motor platen, and the lower endplate is stationary and isolated from the rest of the machine. The lower motor platen is designed to carry an optical micrometer (Omron Model Z4LA-L10), and move at one-half the velocity of the lower motor to provide the measurements of midpoint filament diameter that are necessary for filament stretching rheometry.

2.2.1 *Motor Platens*

The FISER II motion control system was manufactured by Northern Magnetics, Inc (now a division of Baldor). The two linear DC brushless motors are open-loop controlled by a Delta Tau PMAC-Lite Controller that is interfaced with a Labview operating system (see Figure 2.2). The position of the motors can be controlled to within 1 μ m and can be measured to within $\pm 1\mu$ m via an optical encoder. In the majority of the current experiments, only the upper motor was utilized, and filament radius measurements were not taken. Table 2.2 contains information concerning the velocity and position limits on the upper motor.

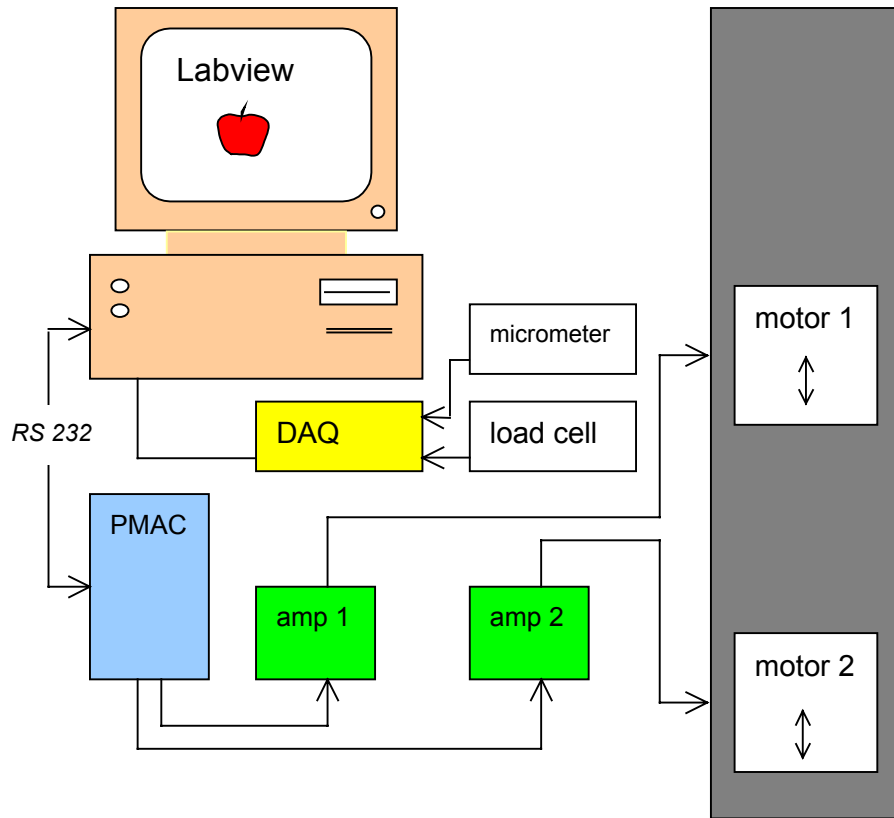


Figure 2.2 Block diagram showing operation of the FISER II filament stretching rheometer.

	Maximum Value	Resolution
L_p	180cm	1 μ m
$V_p = \dot{L}_p$	300cm/s	.035cm/s

Table 2.2 Motor position and velocity limits for the FISER II rheometer.

Prior to each experiment, a motion control program file with the desired velocity profile is generated using the Labview program and uploaded to the PMAC via RS232. For an exponential velocity profile, the motion control program file would also contain information such as the desired strain rate, the initial gap, and the desired final strain. After each experiment, the motion control system creates a data file containing command and encoder-determined positions for the motors for that experiment. A plot containing motor position error data as a function of

strain, $\varepsilon \equiv \ln(L(t)/L_0)$, for a typical experiment is given in Figure 2.3. Note that overall position error increases cumulatively with position, but that position error remains small as a fraction of commanded position during a stretch.

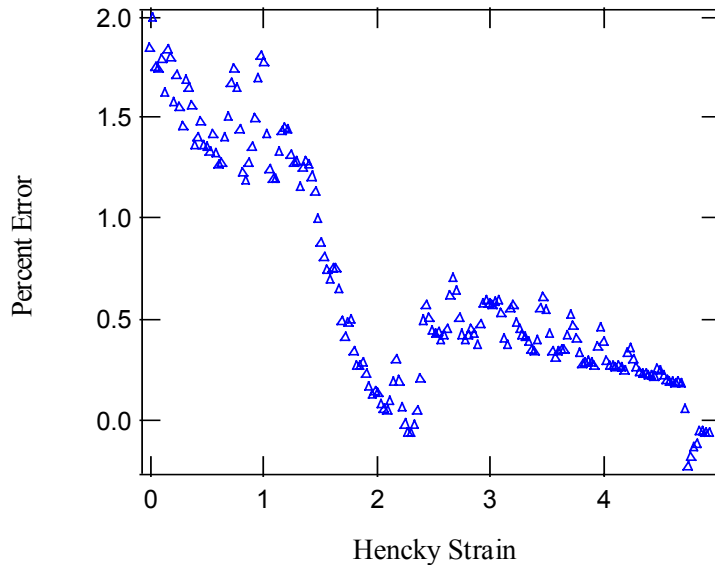


Figure 2.3 Motor position error as a fraction of distance traveled for a typical exponential velocity profile.

The motor platen motion is controlled in the PMAC motion control program by dividing the experiment into a number of time-steps, then specifying a desired position for each time. In addition to specifying position/time data, an acceleration time must also be specified in the file. This acceleration time is roughly the time required for the motor to move from one position to the next. For experiments performed at a low strain rate, and for extensional rheology experiments (for which the initial stages of the stretch are not as important), a rather large acceleration time is acceptable. However for the current experiments at high strain rates, which correspond to short stretch durations, a short acceleration time is more appropriate. Figure 2.3 shows the effect of altering the acceleration time on motor position as a function of time; note that for the same, programmed exponential position profile, the case with the smaller acceleration time reaches the ideal commanded position sooner. An exponential velocity program requires that at the start of the stretch the motor must move to a finite velocity instantaneously. This is physically impossible, and the actual velocity follows a profile that can be empirically modeled as

$$V(t) = V_0 e^{\dot{\varepsilon}t} (1 - e^{-t/\tau}) \quad (2.3)$$

where τ is a timescale of the linear motor that depends on the programmed motor acceleration time. As the acceleration time decreases, τ decreases as well, and from Equation 2.2, the actual velocity reaches the ideal velocity sooner. This is not to say that a small acceleration time is always ideal. For example, at low strain rates, tests can be rather long and a short acceleration time causes the motor to make unnecessary movements that would serve only to add more noise to the motion profile.

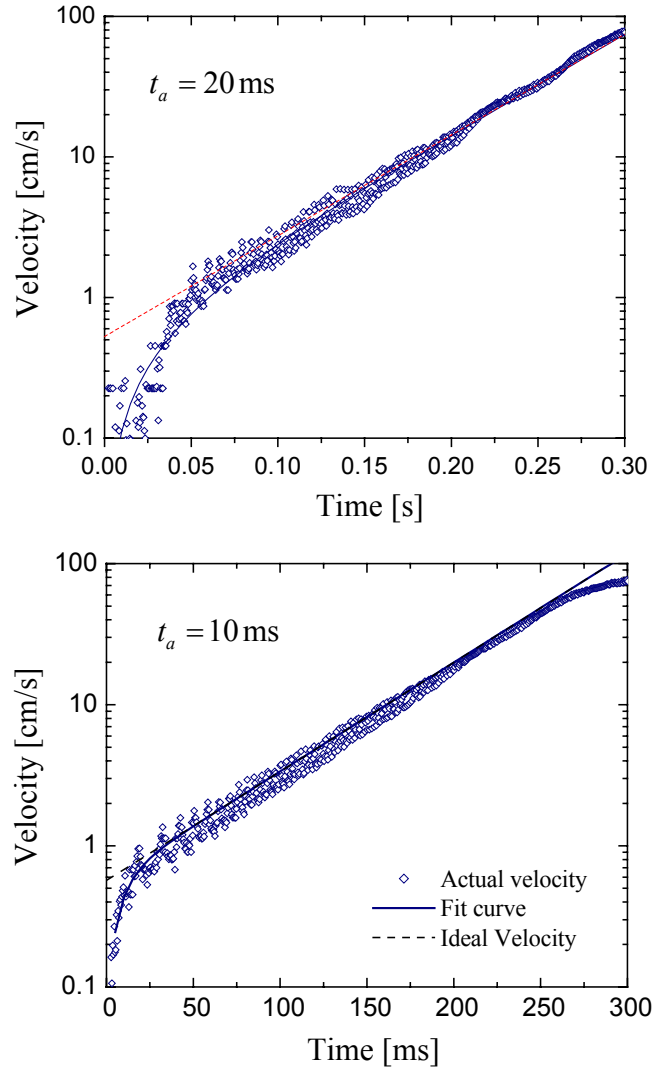


Figure 2.4 Effect of altering the motor acceleration time. The upper plot in the figure above corresponds to a motor acceleration time of 20ms. A smaller acceleration time (10ms for the lower plot) can have the effect of making the velocity profile closer to the ideal exponential profile.

2.2.2 *Endplates and Endplate Assemblies*

The endplates used for the current experiments consist of 5mm diameter by 1mm thick optical windows obtained from Edmund Industrial Optics (Tech Spec 1 Wave) and have a surface roughness on the nanometer scale. The lower endplate assembly consists of one of these windows bonded with optical adhesive to the top of a 6.35mm cube beamsplitter (also purchased from Edmund Industrial Optics) that is rigidly clamped in a specially designed lightweight aluminum fixture (see Figure 2.1). This assembly is then fixed to the top of the load cell, which remains stationary. The load cell is fixed on a two-axis alignment mechanism that permits concentric alignment of the endplates. The beamsplitter permits an axial view of the filament, and the design is compact enough that both the axial view from beneath the endplate and a side view of the filament extending approximately two endplate diameters from the endplate can be imaged simultaneously.

It should be noted that a 12mm beamsplitter and a 10mm optical window of similar specifications to the smaller versions were also purchased. This larger cube allowed for better optical resolution of the instability (although the field of view in the axial direction was more limited), and it also provided the opportunity to probe smaller aspect ratios using the same initial endplate gap. However, it was found that because the nature of the endplate alignment mechanism, which is discussed in the next paragraph, the larger endplate was much more difficult to align for the same initial endplate gap, therefore the smaller endplate assembly was used for the majority of the experiments.

Endplate parallelism is achieved by adjusting a universal-joint mechanism and tuned using visual aid from two CCD cameras aimed at the side of the endplates and opposed at a 90° angle. It should be noted that this mechanism provides some finite angular resolution, meaning that as the endplate radius is increased, sine errors pose a problem. Nevertheless, the mechanism was well suited for alignment of the 5mm endplates at the smallest gap used; 100 microns. The endplate axial position is adjusted by hand using a micrometer head and zeroed using the DC signal from the force transducer. To accommodate the larger forces encountered in the current experiments (due to smaller aspect ratios), both the upper and lower endplate support assemblies were redesigned and strengthened to accommodate the larger axial forces seen in adhesive testing.

2.2.3 *Data Acquisition*

As mentioned in the previous paragraph, PMAC the motion control system creates a file containing encoder data for the motor positions in addition to the command position data for each experiment. Signals from the load cell and radius measurement device are fed into the PMAC and are also written into this data file. The PMAC can store data from only one experiment, and the data file must be downloaded to an external computer before the next run. In addition to the PMAC-gathered data, a data acquisition card (National Instruments PCI-MIO-16XE-50) is used in conjunction with a personal computer to acquire load cell and radius measurement data. The PMAC can only store two thousand data points, so for long experiments, i.e., experiments at low strain rates, the large number of data necessitates the use of the file generated by the data acquisition card.

2.2.4 Force Measurements

Axial force measurements were taken using two externally amplified strain-gage based load cells (Futek L2338). These load cells used 10 gram and 1kg capacities in both tension and compression, and have resolutions of 5 milligram and 500 milligrams respectively. The Futek L2338 load cells were alternatively used as required for a given experiment. The load cells were calibrated in compression regularly to ensure that any change in sensitivity was noted and accounted for in the data analysis. It should be noted, however, that no drift in the sensitivity was seen for either of the load cells over the entire three-month period during which the majority of the experiments in this thesis were performed. The sensitivity of the 10 gram and 1 kg load cells were found to be 0.997 [V/g] and 99.7×10^{-3} [V/g] respectively. The data in Figure 2.5 is typical of that recorded using the Futek L2338 load cell for these experiments.

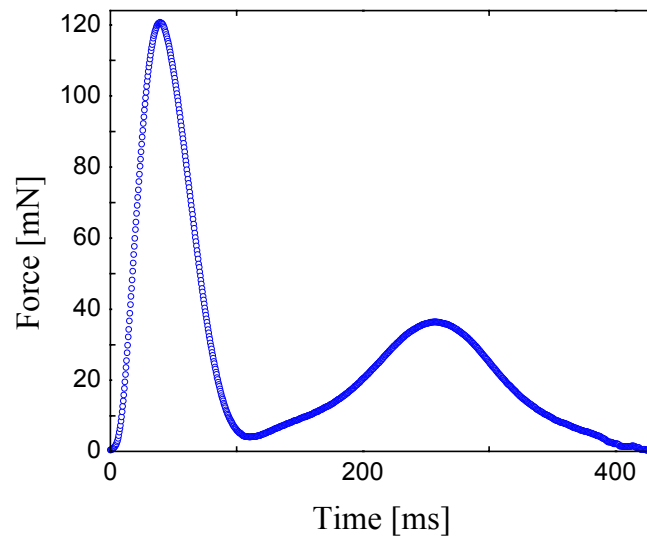


Figure 2.5 Typical experimental force data plotted vs. time. The data is for the PS025 Boger fluid for $De=67$ and $\Lambda_0=0.22$. Note that the first peak in the curve can be explained by lubrication theory (see Section 2.3.1) and that the second peak is due to flow induced elasticity, or strain hardening of the fluid

In addition to the static compression calibration, each of the load cells were calibrated dynamically using two methods similar to those used by Anna [2] for dynamic characterization.

The first method involves using a permanent magnet and a small coil excited by an oscillating current. As indicated by Figure 2.6 (a), the magnet was firmly attached to the top of the load cell. A coil was then placed just above the magnet, and a small AC current applied using a lock-in amplifier (EG&G Model 7260), thus applying a sinusoidal load to the force transducer in the form of

$$f(t) = A \sin(\alpha t). \quad (2.4)$$

The output signal from the load cell was sent to the lock-in amplifier, and the relative magnitude of the input and output signals were recorded for several oscillation frequencies, α (see Figure 2.8).

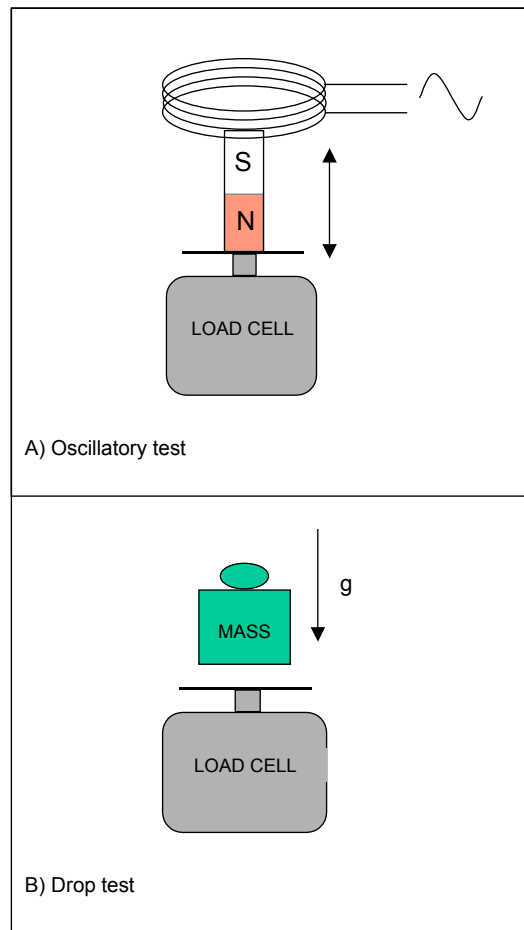


Figure 2.6 Schematics of the drop and oscillatory tests used to analyze the dynamic response of the load cells.

The data from these tests was then plotted and a second order differential equation was used to fit to the data using a computer program. The modeling differential equation is

$$\ddot{x} + 2\gamma\dot{x} + \omega_0^2 x = f(t), \quad (2.5)$$

where $f(t)$ is the external force applied to the coil and $x(t)$ is the transducer output signal. The fit parameters, representing the natural frequency, ω_0 , and the damping coefficient γ , for both the 10g and 1kg L2338 load cells are listed in Table 2.3. Both load cells were found to have very similar dynamic behavior, as indicated by the plots in Figure 2.7, which show the results of the oscillatory tests. As a result of sufficient damping, the amplitude of the output signal rapidly decreases at frequencies beyond the natural frequency. To verify the results of the oscillatory tests, a second ‘step signal’ method was employed. In this test a mass resting on the load cell was quickly removed and the load cell probe was allowed to return to equilibrium. The output signal was recorded and a curve was fit to the data by inserting the parameters listed in Table 2.3 into the homogenous solution of Equation 2.4, a formula for the normalized response of the load cell to a step signal can be written

$$\frac{x(t)}{x_0} = 1 - e^{-\gamma t} \left(\frac{\gamma}{\omega_0^2 - \gamma^2} \sin\left(\sqrt{\omega_0^2 - \gamma^2} \cdot t\right) + \cos\left(\sqrt{\omega_0^2 - \gamma^2} \cdot t\right) \right), \quad (2.6)$$

where $x(t)$ is the transducer output signal, x_0 is the magnitude of the initial output signal, and the parameters ω_0 and γ are the natural frequency and damping coefficient found from the oscillation test. The results of the step signal test and the fit curve for the 10g L2338 load cell are shown in Figure 2.8.

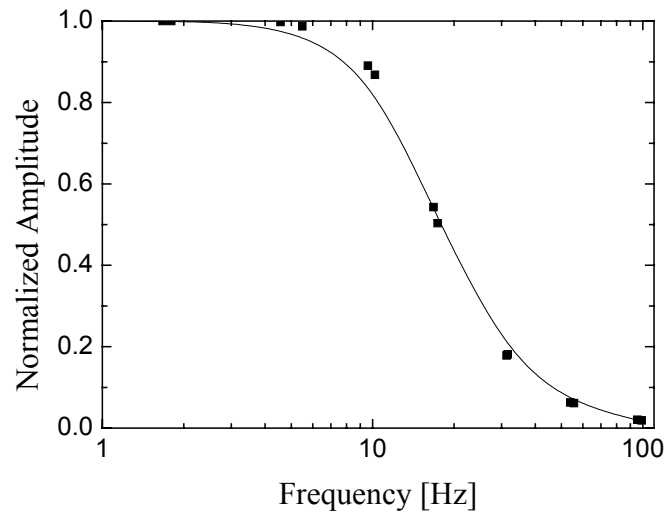
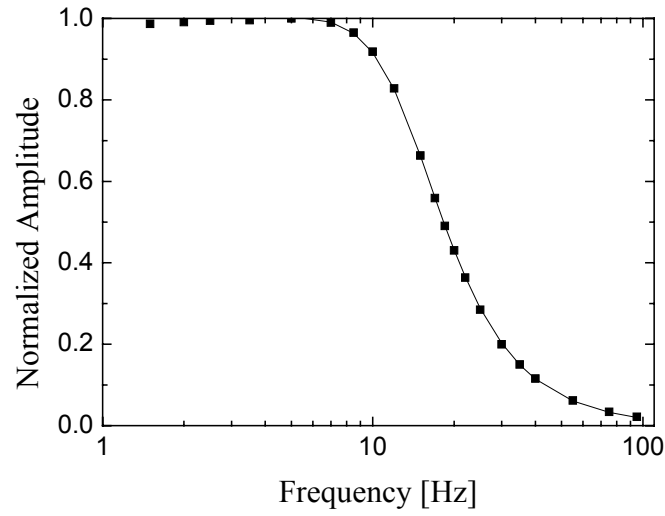


Figure 2.7 Results of oscillatory test (signal amplitude vs. oscillation frequency) for Futek L2338-10g (top) and 1kg load cells. The model fits (Equation 2.3) are also given.

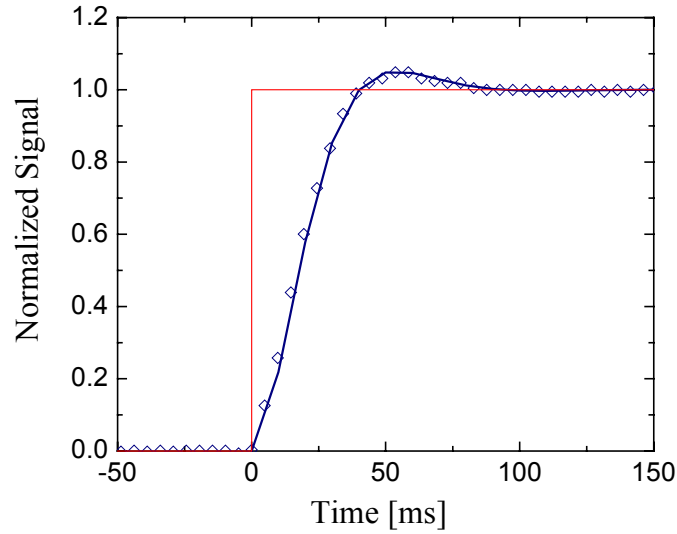


Figure 2.8 Results of step signal test for 10 gram L2338 load cell and fit curve generated using fit parameters determined from the oscillation test. The step function is also shown as a reference.

2.2.5 *Dynamic Testing of Futek load cells, Model L2338-Q10419*

In addition to the testing done on the Futek model L2338 load cells and described in the last paragraph, two other Futek load cells were dynamically tested in order to determine their suitability for use in these experiments. The two load cells, 10gram and 100gram capacity versions of Futek model L2338-Q10419 and having built-in amplifiers, were acquired and subjected to the same dynamic tests described above. It was determined that the newer models had significantly less damping than the older L2338 models. This is indicated by the spike, or resonance frequency, in the amplitude plot for the magnet/coil test (see Figure 2.9, top) and the rather long decay time of the output signal following the step input of the drop test (see Figure 2.9, bottom). In addition to the damping problem, the load cells had a significant deflection (~1mm) and the load cells were determined to be unsuitable for filament stretching tests. The data in Table 2.4 lists the results of the testing of all four Futek load cells for comparison.

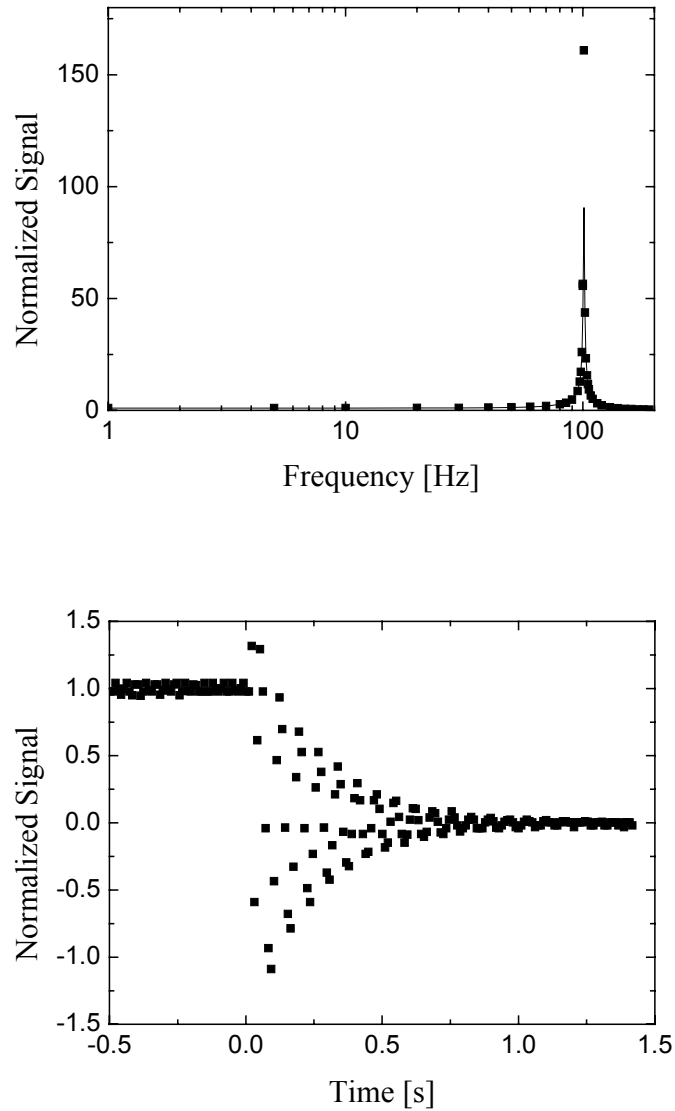


Figure 2.9 Results of oscillatory (top) and drop test (bottom) for Futek model L2338-Q10419 100g. Note that in the oscillatory test, a large spike occurs at a driving frequency of around 100 Hz, signifying resonance. This underdamping is also evident in lower plot, which contains the data from the free oscillation test. It takes almost a full second for the oscillations to settle.

Load cell	ω_0 [rad/s]	γ [s ⁻¹]	Step decay time [ms]
L2338 (10g)	78.7	56.2	50
L2338 (1kg)	84.3	59.5	50
L2338-Q10419 (10g)	239	1.5	~ 1000
L2338-Q10419 (100g)	634.6	3.5	~ 1000

Table 2.3 Measured parameters for all of the Futek load cells tested.

2.2.6 Video Imaging

Every experiment performed for this thesis was recorded on digital video tape (MiniDV) at 30 frames per second. This format allows for still frames of good quality to be easily extracted from the tape for analysis. The tape contains a digitally encoded frame index allowing the images to be matched to strain and force data for an experiment. The diagram in Figure 2.10 shows a side view of the beamsplitter and the optical path leading to the camera. Note that in this application, the beamsplitter acts as a mirror, allowing visualization of the bottom of the fluid sample from the view of the camera. The camera view has an aspect ratio of 4:3 and experiments were recorded so that the long axis of the camera was aligned with the flow direction, allowing for maximum visualization of the filament and possible fibrillation during stretching. The setup allowed for a field of view that extended from the base of the cube beamsplitter to approximately two endplate diameters beyond the endplate surface for a total viewing area of approximately 16 x 12mm in size. Lighting was provided by a electroluminescent diffuse light source (Lucas Proto-Cut) placed behind the beamsplitter and in conjunction with a fiber optic light source focused on the front of the cube from an angle of approximately 45° above the camera viewing axis. Both of this light sources produce a negligible amount of heat, a detail that is crucial because of the thermal sensitivity of the test fluids. The CCD camera used to record the video images was a Cohu Model MS12 with 798 x 494 pixels and a Computar C-mount, 25mm 1:1.8 lens. The camera was set to record continuous video at 30 frames per second, thus providing strain resolution of

$$\pm \Delta \varepsilon = \frac{1}{30} [\text{s}] \cdot \dot{\varepsilon}_0 [\text{s}^{-1}]. \quad (2.7)$$

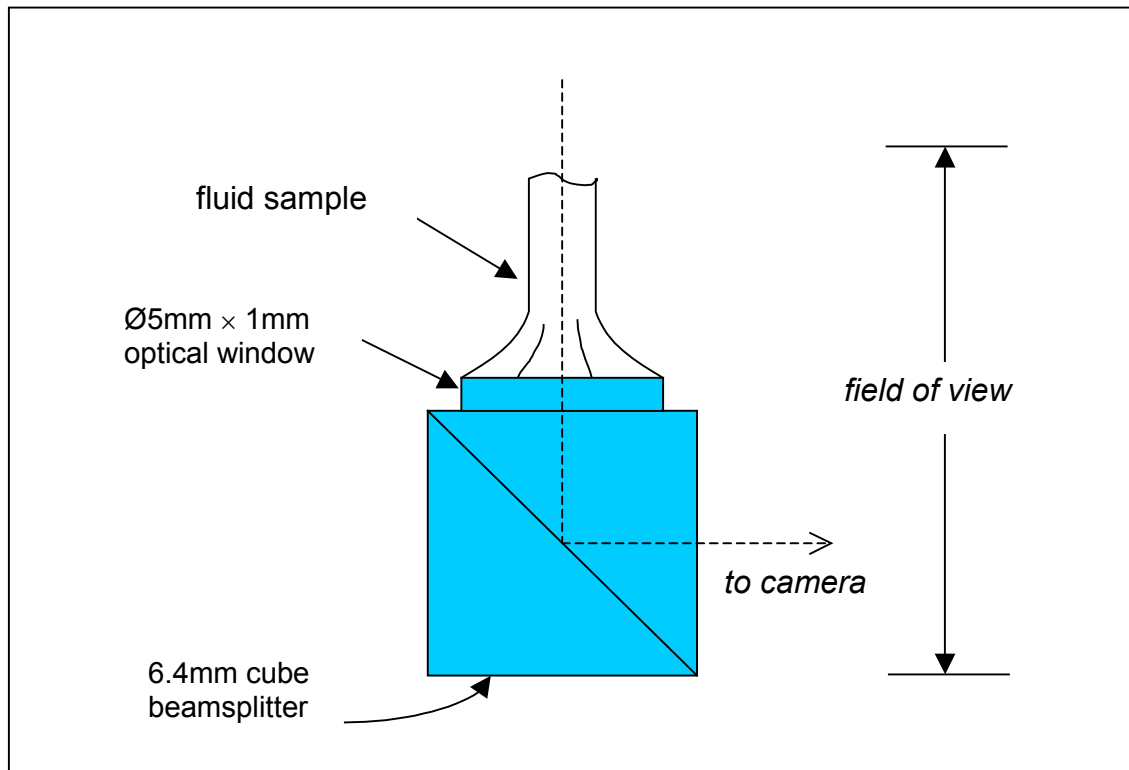


Figure 2.10 Sketch of the beamsplitter and optical window and the optical path from the fluid sample to the CCD camera.

2.3 Data Analysis

The data from the experiment is written to a text file and exported to a personal computer from the PMAC. This text file can then be opened in a program such as Excel or Matlab for analysis. As mentioned already, the bulk properties of the test fluids are strongly dependent upon temperature. Time-temperature correction using thermorheological simplicity, which is detailed in Chapter 3, is implemented so that experiments can be compared at a common reference temperature. The radius data measurements are fairly straight forward require no post-processing. The Omron laser micrometer has a dynamic response of $5\mu\text{s}$ and was calibrated by the author using optical fibers of similar opacity to the test fluid and found to be linear at diameters as low as $20\mu\text{m}$. The signal from the Futek L2338 load cells, however, is convoluted with a significant dynamic response ($\sim 100\text{ms}$) of the load cell itself. This response was measured using methods detailed in Section 2.2.4. The following section contains an explanation of how the response of

the load cell was deconvoluted from the raw signal and how this deconvoluted signal compares to the prediction of the force from lubrication theory for a typical stretching experiment.

2.3.1 Force Data

A typical force versus strain curve for a probe-tack test on a pressure-sensitive adhesive has the characteristic feature of a large spike in the measured force, followed by a second, more gradual increase in force [21]. It is generally accepted that the second increase in force in this characteristic curve is due to strain hardening.

Though they are not true pressure-sensitive adhesives, the strain-hardening Boger fluids used for the current experimental investigations demonstrate very similar behavior (see Figure 2.5). A recent article by Francis & Horn [69] applies lubrication theory to find an analytical solution of the force curve for a Newtonian liquid in a specific probe-tack tester. In this study, the authors model a probe-tack tester as a probe attached to a linear actuator, but coupled by a spring. When the stretch starts lubrication forces cause the spring to stretch, and the motion of the probe is not the same as the motion of the actuator. This results in a force with a peak that grows from zero when the stretch begins and goes through a maximum when the spring is at maximum extension. Even though the system used for experiments in this thesis, like most probe-tack testers, contains no spring (there is no significant deflection of the load cell probe or endplate mechanisms), the initial spike in the force data during a stretch can also be explained by the lubrication theory.

If an ideal, instantaneous strain profile is implemented to stretch a viscous Newtonian liquid, there is no physical reason for the actual axial force to start at zero, increase quickly to a peak, then decrease sharply. For a Newtonian fluid, Reynolds lubrication theory [42], [70] provides a solution for the axial force for reverse squeeze flow, provided that the fluid is confined enough that it can be assumed to be an infinite layer (see Figure 2.12). The Reynolds equation for the pressure distribution as a function of radius and time for squeeze flow is written

$$P(r, t) = P_0 + \frac{3\mu V_z(t)}{L(t)^3} (r^2 - R_0^2), \quad (2.8)$$

where μ is the shear viscosity of the fluid, R_0 is the endplate radius and V_z , and L are the axial velocity and endplate separation distance as functions of time. This solution is valid in the lubrication limit when the product of the Reynolds number and the square of the initial aspect

ratio are small, or when $Re \Lambda_0^2 \ll 1$. In the case of the current experiments, this condition becomes $L(t) \ll R_0$, since the Reynolds number is always small. For such a flow, the inertial terms in the Navier-Stokes equations are negligible. The flow is then considered reversible Stokes flow, meaning the squeeze flow solution also applies the case of reverse squeeze flow. By integrating Equation 2.8 over the area of the endplate, an equation for the axial force as a function of time can be written

$$F_z(t) = \frac{3}{2} \mu \pi R_0^2 \frac{V_z(t)}{L(t)} \left(\frac{R_0}{L(t)} \right)^2. \quad (2.9)$$

Because of volume conservation and the no-slip condition, the radius is not constant either axially or temporally, this relation can only be considered to be valid at the initial moments of the stretch. Equation 2.9 predicts that the force should be at a maximum at the instant the stretch starts, so long as the velocity profile V_z in Equation 2.4 starts at a positive value. Thus, the force should decrease from a maximum at the beginning of the stretch for both a linear profile, such as that used in the probe-tack test, and for an exponential profile, like the one used for the current experiments. This is regardless of the fact that two velocity profiles result in totally different strain rates during the experiment (see Figure 2.11). Finally, although it is true that a pressure-sensitive adhesive is not a Newtonian fluid, it is often true that the initial response of the fluid, before any strain hardening can occur, can be considered viscous.

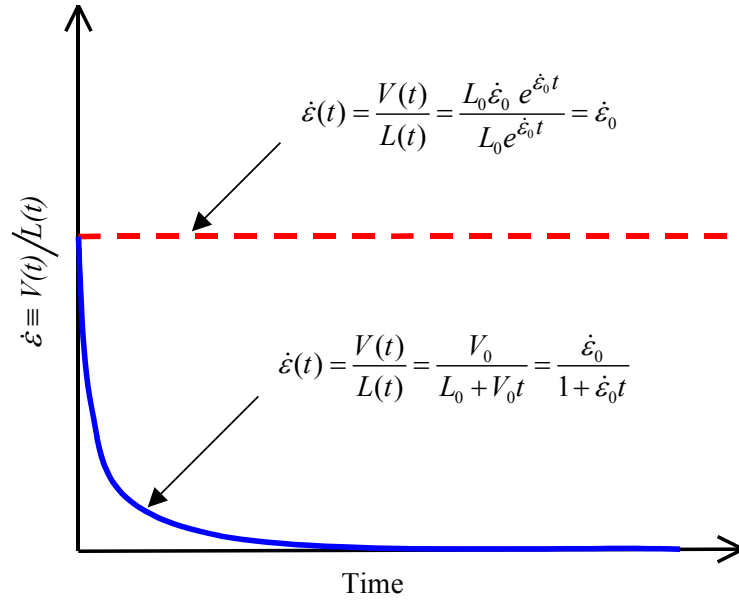


Figure 2.11 In elongational flow, the strain rate is defined as the instantaneous stretch velocity over the instantaneous length. An exponential stretch rate results in a strain rate that is constant in time, while a linear stretch rate leads to a strain rate that decreases hyperbolically in time.

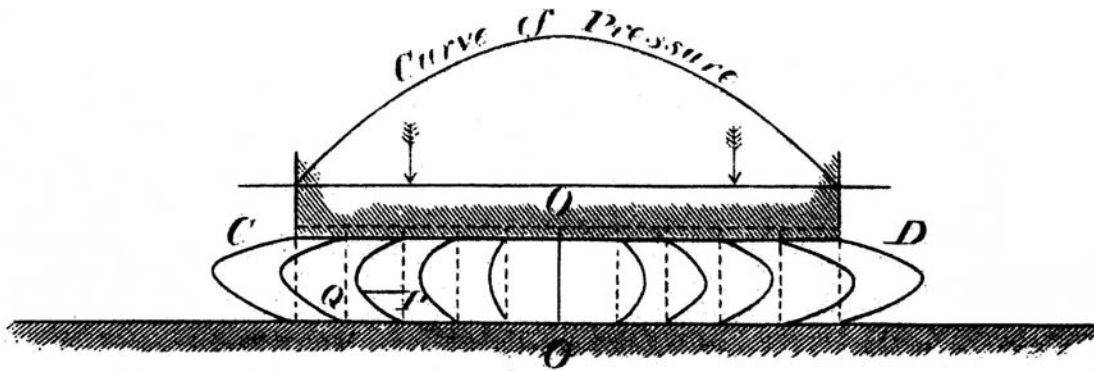


Figure 2.12 Sketch of a squeeze flow with a geometry similar to that of the current experiments. For small Reynolds number (Stokes flow), the squeeze flow is reversible and lubrication theory applies. Figure taken from O. Reynolds [42]

What has been ignored in the preceding discussion is the fact that a real stretching apparatus can never reach a finite velocity instantaneously. There is always some ramp-up time, no matter how minute, and the velocity starts at zero at time zero. The response of the linear motor used in the stretching apparatus in these experiments was explained in a previous section and can be modeled with Equation 2.3. When this ‘true’ velocity profile is substituted into Equation 2.9, it is obvious that the force will have a peak value after the stretch begins. The data plotted in Figure 2.13 consists of the prediction of Equation 2.9 for an ideal exponential velocity function, $F_{act}(t)$, as well as the force curve predicted from the actual velocity profile of Equation 2.3, i.e.,

$$F_{act}(t) = \frac{3}{2} \eta \pi R_0^3 \frac{V_0 e^{\dot{\epsilon}t} (1 - e^{-t/\tau})}{(L_0 e^{\dot{\epsilon}t} (1 - e^{-t/\tau}))^3} \quad (2.10)$$

The experimentally measured data of Figure 2.5, $F_{exp}(t)$, is also shown on this plot. Finally, a plot of the force predicted from lubrication theory with the actual velocity profile (machine response time), but convoluted with the force transducer response from Equation 2.3. This can be written

$$F_{conv}(t) = \mathcal{L}^{-1} \{ F_{act}(s) * R(s) \}, \quad (2.11)$$

where \mathcal{L}^{-1} is the inverse Laplace operator, $F_{act}(s)$ is the Laplace transform of Equation 2.10 and $R(s)$ is the response of the load cell which can be found by expressing Equation 2.5 in Laplace space:

$$R(s) = \frac{X(s)}{f(s)} = \frac{1}{s^2 + 2\gamma s + \omega_0^2}. \quad (2.12)$$

The excellent agreement between the prediction of Equation 2.8 and the experimental force data serve to validate the use of the lubrication approximation as well as to explain the characteristic spike seen in force data of probe-tack tests of PSAs.

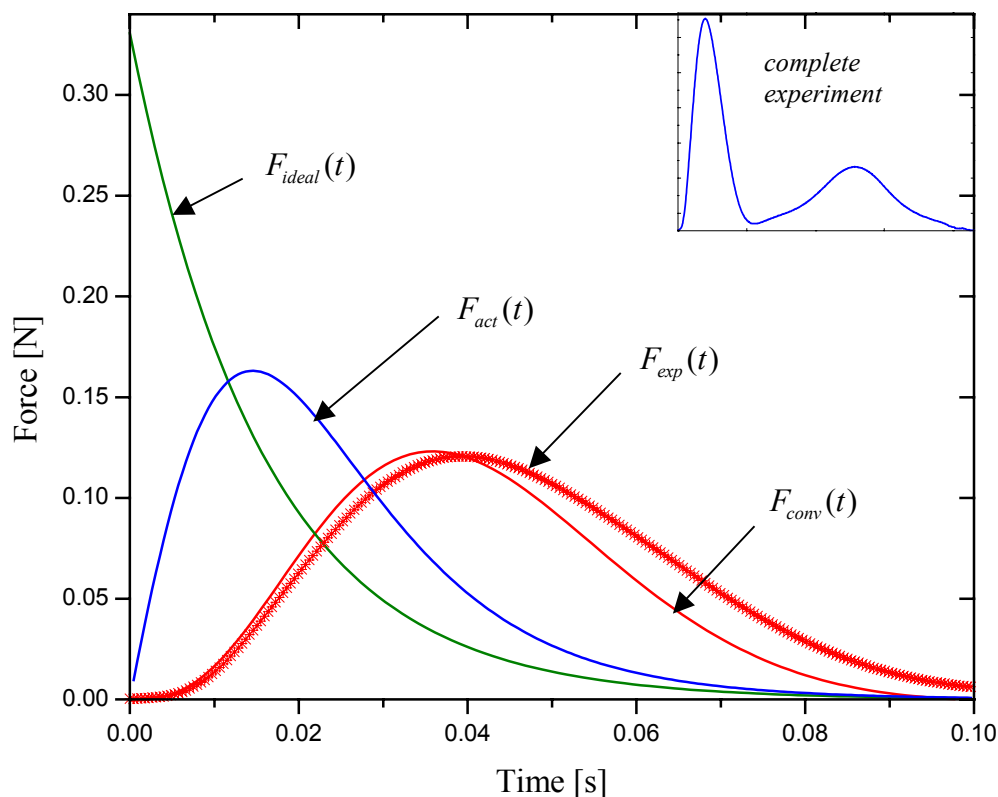


Figure 2.13 The lubrication approximation for the initial force response for a given experiment is convolved with the response of the load cell and the linear motor. The resulting curve matches the actual measured force. The inset plot contains complete experimental force data for the same experiment; the second peak is a result of strain hardening. The experimental data is the same as that shown in Figure 2.5.

2.4 Conclusion

The filament stretching apparatus built by Anna has been modified in order to test mobile fluids in a manner quite similar to the probe-tack test used to test pressure-sensitive adhesives. The resulting experiment permits a very thin layer of a test fluid to be stretched at a pre-programmed rate while measuring the axial force as a function of time, or strain. In addition, a special endplate setup allows the fluid sample to be viewed from beneath and images are recorded with CCD camera. The dynamic response times of the linear motor and the force transducer were characterized experimentally. It was found that when these transient effects were accounted for in the measured experimental force data, the data matched the theoretical prediction of the Reynolds

lubrication theory very well. It is concluded that the apparatus is well suited for the measurements undertaken in this thesis. The current experiments are intended to investigate flow instabilities that occur during stretching, and for these experiments, three model fluids were chosen. The composition and shear rheology of these test fluids are discussed thoroughly in Chapter 3, and the results of the experimental investigations can be found in Chapter 4.

Chapter 3 Test Fluids

For the large majority of the experiments performed for this thesis, styrene-based fluids (a Newtonian fluid and two ideal elastic, or “Boger”, fluids) were used. The polystyrene Boger fluids were previously characterized experimentally in both shear and elongational flow by Anna [14], [2]. As mentioned already, Boger fluids possess the unique characteristic of being both viscoelastic and having a constant shear viscosity, making them useful for isolating and studying the phenomenon of flow induced elasticity. In keeping with this idea, a Newtonian styrene oil of similar shear viscosity (the solvent for the Boger fluids) was used for many experiments as a benchmark fluid. Polystyrene solutions can be sensitive to light and heat and in order to check whether the fluid properties had changed significantly since the experiments done by Anna in 2000, the shear rheology measurements of the styrene-based test fluids were repeated by the author using a cone-and-plate rheometer.

In addition to the styrene-based fluids, a concentrated, entangled polybutadiene fluid was mixed by the author for use as a test fluid in investigations into elastic instabilities during stretching. To create this fluid, a small amount of high molecular weight, monodisperse polybutadiene was dissolved in a low molecular weight polybutadiene. Unfortunately, the fluid did not prove to be elastic enough to be useful for studying the elastic instability. Nevertheless, the details of the composition, mixing process, and results of shear rheometry of this fluid are reported in Section 3.3.

A plot of the phase space of concentration and molecular weight is given in Figure 3.1. All of the discussed in this chapter can be located on this plot, referred to as the Graessley diagram [71]. Boger fluids normally lie in the dilute region of the Graessley diagram where the concentration is less than the overlap concentration, c^* . The overlap concentration is the polymer concentration at which the volume occupied by the polymer molecules based on an equilibrium radius of gyration exceeds the total fluid volume, i.e.

$$c^* = \frac{M_w}{\frac{4}{3}\pi R_g^3 N_A}. \quad (3.1)$$

One of the two polystyrene Boger fluids falls in the dilute region of Figure 3.1, while the other Boger fluid, which mixed with a higher concentration of a higher molecular weight polymer, is in the semi-dilute unentangled region of the plot. Note that although the SM3 fluid’s concentration is greater than c^* , its viscometric behavior (see Section 3.1.2) is like that of a Boger

fluid. On the Graessley diagram, the Newtonian styrene oil is located in the concentrated unentangled region. The polybutadiene fluid was mixed using a rather high molecular weight polymer at a concentration high enough to be considered a concentrated entangled fluid in Figure 3.1, i.e., a fluid which a with a concentration beyond c^{++} (see Graessley) [71], where

$$c^{++} \approx 0.1 \text{ g/cm}^3. \quad (3.2)$$

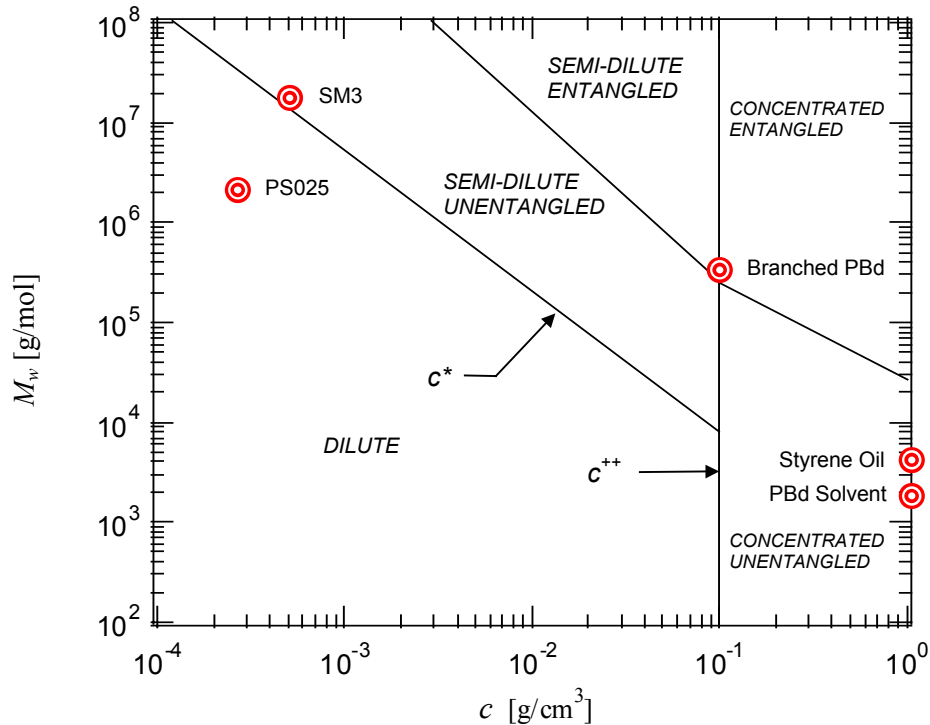


Figure 3.1 Graessley plot showing characteristic regimes of polymer dynamical behavior [71].

3.1 Styrene-based fluids

The two polystyrene solutions were mixed for earlier experiments carried out by Anna and were chosen for the current work because of their viscoelastic properties and the fact that these fluids had already been investigated in shear and elongational flow. The *dilute* unentangled solution and the *semi-dilute* unentangled solution were termed is “PS025” and “SM3” respectively in a previous publication by Anna *et al.* [14]. For simplicity, and to avoid confusion, these fluids will henceforth be referred to by those names. Information concerning the

composition and other physical properties of these solutions as well as those for the styrene oil (used as both a solvent for the solutions and as a test fluid in these experiments) can be found in Section 3.1.1. The results of shear rheology measurements performed by the author are discussed in Section 3.1.2. For more detailed information concerning these fluids, the reader may consult the PhD thesis by Anna [2].

3.1.1 *Fluid Composition*

The PS025 fluid was made by dissolving a high molecular weight, monodisperse polystyrene (obtained from Scientific Polymer Products by S.Anna) in oligomeric styrene oil at a concentration of 0.25 wt%. The SM3 fluid was mixed in a similar manner but a polymer of higher molecular weight (10 times higher) was used and it was mixed at a concentration that was double that of the PS025. The polymer for the SM3 fluid was obtained from Pressure Chemical and the solution was mixed by Prof. Susan Muller at the University of California at Berkeley for use as one of the test fluids in the interlaboratory extensional rheometer comparison [14]. Both polymers had a polydispersity index (PDI) of less than 1.20 as defined by the ratio of the weight averaged molecular weight, M_w , to the number-averaged molecular weight, M_n [3]. Changing the molecular weight and concentration of the polystyrene in the solution significantly changes the elasticity of the fluid without dramatically changing the shear viscosity and is therefore a good way to isolate and investigate the effects of these variables on viscoelasticity, which was in fact a goal of the work done by Anna. Figure 3.2 contains data from a filament stretching extensional rheometry experiment on the PS025 fluid. The dramatic increase in the Trouton ratio (η_E/η_0) as a function of strain is a clear indication of the flow-induced elasticity of these fluids. The solid curve on this plot is the prediction of the FENE-P constitutive model (FENE = Finitely Extensible Non-linear Elastic) [5], [7]. This model statistically simplifies the polymer chain by considering the polymer chains as beads connected by finitely extensible springs. Note, however, that the FENE-P model tends to under predict the experimental data in Figure 3.2 by up to an order of magnitude at intermediate strains ($2 \leq \varepsilon \leq 4$), reflecting the models poor capabilities for predicting transient viscoelastic flows.

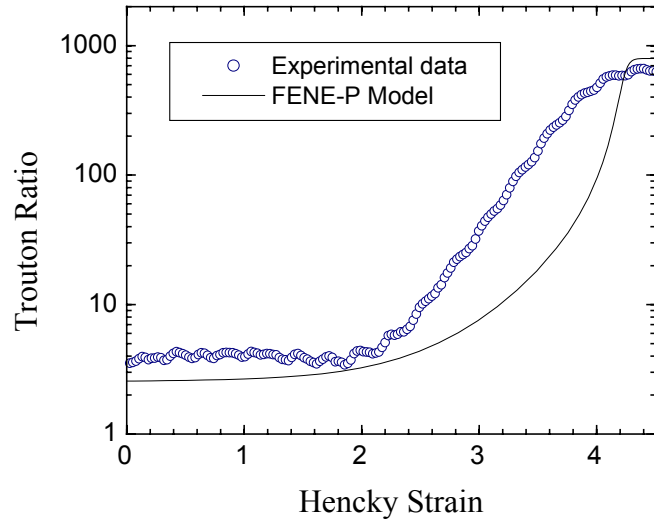


Figure 3.2 Transient extensional rheometry data and FENE-P fit for PS025 fluid with $De=10.0$ and $\Lambda_0=1.0$

The data in Tables 3.1 and 3.2 were excerpted from the thesis by Anna and list the quiescent fluid properties and physical properties of these styrene-based test fluids. The Newtonian, oligomeric styrene oil that was used as the solvent for both of the polystyrene Boger fluids was obtained by Anna from Hercules under the name ‘Piccolastic A5 Resin’. The polystyrene solutions are non-toxic and non-volatile. The results of a Thermal Gravimetric Analysis (TGA) (with a temperature ramp between 23-150 °C) on the PS025 showed that the solution experienced no detectable weight loss until 42 °C, and at 60 °C it had only lost 0.15% of its initial mass [2]. The current experiments were performed at room temperature (20-30 °C) so thermal degradation is not considered as an issue of major concern. The solutions *are* slightly susceptible to degradation by UV light. To avoid deterioration of the polymer solutions, they have been stored in a dark, refrigerated environment. Nevertheless, the author has repeated shear rheology measurements in order to verify the viscoelastic properties of the test fluids for the current experiments.

	M_w [g/mol]	R_g [nm]	c [g/mL]	c^* [g/mL]	c/c^*	PDI
PS025	2.25×10^6	15	0.00025	0.00078	0.33	1.02
SM3	2.0×10^7	133	0.00051	0.00034	1.50	<1.20
Styrene Oil	3.85×10^2	~	~	~	~	1.33

Table 3.1 Quiescent solution properties of styrene-based test fluids

Density, ρ [kg/m ³]	1026
Surface Tension, σ [N/m]	0.0378
Thermal Conductivity, k [W/m-K]	0.167
Heat Capacity, c_p [J/kg-K]	2040

Table 3.2 Physical properties of styrene oil at 25° C

3.1.2 Shear Rheometry

Viscometric measurements for all of the test fluids used in this thesis were performed with a TA Instruments AR1000 stress-controlled rheometer using a cone-and-plate geometry (4cm diameter, 2° stainless steel cone). Measurements of shear viscosity as functions of both strain and temperature were performed for all fluids and viscoelastic measurements of the non-Newtonian fluids were done using small amplitude oscillatory shear flow. The results of the shear viscosity measurements for all three of the styrene based test fluids as a function of shear rate can be seen in Figure 3.2. Note that the shear viscosities of the PS025 and the oligomeric styrene oil are very close ($\sim 30 \text{ Pa} \cdot \text{s}$). The viscosity of the SM3 fluid is higher by a roughly a factor of two, as a result of the higher polymer concentration and molecular weight. For the two non-Newtonian fluids, the data is indeed nearly constant as a function of shear rate as expected for Boger fluids. The apparent spike in the shear viscosity of the SM3 fluid is actually an artifact of elastic flow instability in torsional flows, e.g. the cone-and-plate rheometer. For more details about this instability, the reader may refer to the recent article by Rothstein and McKinley [72]. The results of the shear viscosity tests indicated that the viscosities each of the three fluids had increased since the measurements by Anna. This increase can be attributed to a slow polymerization of the oligomeric styrene. The viscosity of the PS025 fluid had increased by 26% and the SM3 by 8%. The results of the shear viscosity measurements are tabulated in Table 3.3 along with other measured and calculated values resulting from the shear rheometry of these fluids.

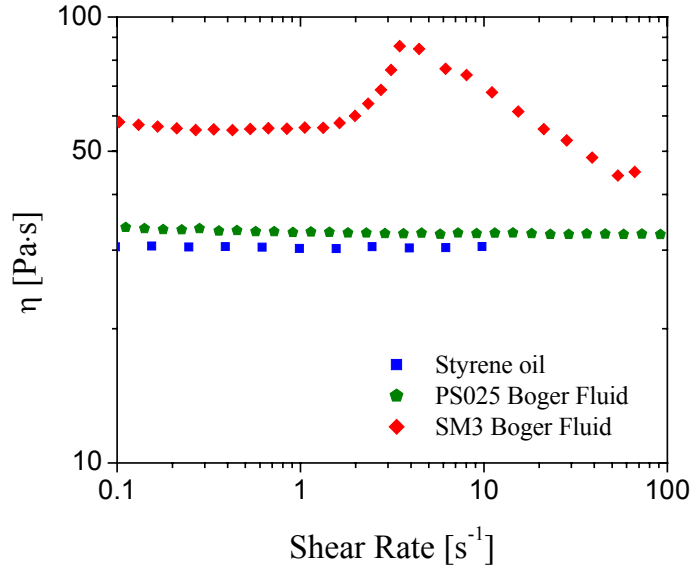


Figure 3.3 Shear viscosities of styrene-based test fluids as a function of shear rate measured at 25° C. The non-Newtonian fluids have a nearly constant shear viscosity, which is expected for Boger fluids. Note that the apparent spike in the viscosity of the SM3 fluid is an artifact of an elastic flow instability in the cone-and-plate rheometer [72].

The viscoelastic properties of polymeric fluids can be very sensitive to temperature changes. Because the temperature in the laboratory could not be maintained at a constant value, it was necessary to account for these temperature changes in the data analysis. Using the cone-and-plate rheometer, a temperature ramp experiment was performed. For a constant applied torque, the temperature was increased at a rate of 0.5 °C/min over a range of 15-35 °C to measure the shear viscosity as a function of temperature for each of the test fluids. For the styrene oil, the Arrhenius model was used to fit a curve to the data, and therefore generate a model for the zero shear viscosity as a function of temperature. The Arrhenius model can be written

$$\eta(T) = \eta_0(T_0) e^{\frac{\Delta H}{R} \left(\frac{1}{T} - \frac{1}{T_0} \right)}, \quad (3.3)$$

where $\Delta H/R$ is the flow activation energy ($\Delta H/R = 1.8 \times 10^4$ [K] for styrene oil). For the non-Newtonian fluids, the WLF (Williams, Landel, Ferry) model is better suited [5].

The WLF model is written

$$\eta_0(T) = \eta_0(T_0) \cdot \frac{T}{T_0} e^{\frac{-a(T-T_0)}{b+(T-T_0)}}, \quad (3.4)$$

where a and b are the fit parameters (see Table 3.3).

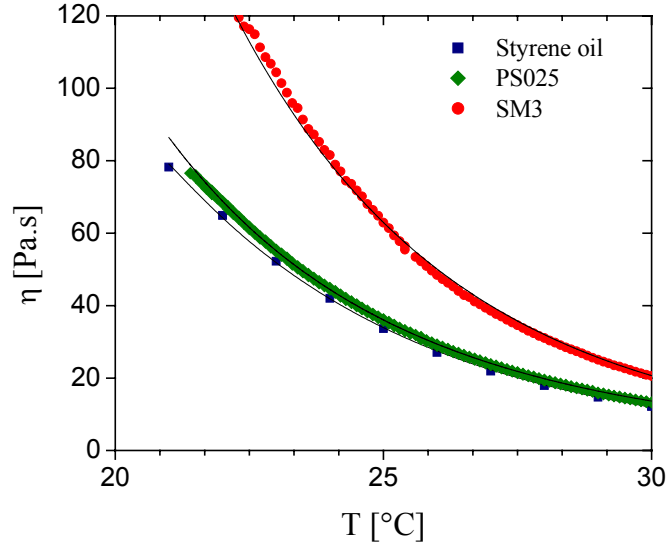


Figure 3.4 Shear viscosity data as a function of temperature together with fit curves for styrene-based fluids

The elastic properties of the test fluids were measured in the cone-and-plate rheometer using small amplitude oscillatory shear flow. In such flow, the shear rate is sinusoidal and

$$\dot{\gamma} = \gamma_0 \omega \cos \omega t, \quad (3.5)$$

where γ_0 is the strain amplitude, and ω is the oscillation frequency. For small amplitude deformations (linear viscoelasticity regime) the resulting shear stress can be separated into two components, one due to the fluid viscosity, and the other due to elasticity

$$\tau_{21} = G'(\omega) \gamma_0 \sin \omega t + G''(\omega) \gamma_0 \cos \omega t \quad (3.6)$$

The component of stress that is in phase with strain (elastic component) in Equation 3.6 is denoted G' which is termed the storage modulus. The out-of-phase, viscous damping component of this stress (in phase with strain rate) is denoted G'' , which is called the loss modulus. The

storage and loss moduli are functions of the oscillation frequency and can be used to evaluate the viscoelastic nature of a fluid.

For fluids lying in the dilute region of the Graessley diagram of Figure 3.1, the Zimm bead-spring model is well suited to model experimental data for the storage and moduli. Although the SM3 fluid is in the semi-dilute unentangled region, the Zimm model has been found to accurately describe this fluid in addition to the PS025 fluid [2]. The Zimm theory uses statistical simplifications to model the polymer chain as a series of beads connected by springs, which can interact hydrodynamically with the solvent. The Zimm model leads to a spectrum of relaxation times, the longest of which, λ_z , is the characteristic time constant of the fluid being modeled. More detailed information concerning the Zimm model can be found in the text by Bird *et al.* [7]. The Zimm model was used to fit the experimental data for the storage and loss moduli as well as the zero shear viscosity of the Boger fluids. The model can be expressed as:

$$\begin{aligned}
 G' &= \frac{cN_A k_B T}{M_w} \sum_{i=1}^{N_m} \left\{ \frac{(\lambda_z \omega)^2}{\left[i^{2(2+\sigma)} + (\lambda_z \omega)^2 \right]} \right\} \\
 G'' &= \eta_s \omega + \frac{cN_A k_B T}{M_w} \sum_{i=1}^{N_m} \left\{ \frac{(\lambda_z \omega)^2 i^{(2+\sigma)}}{\left[i^{2(2+\sigma)} + (\lambda_z \omega)^2 \right]} \right\} \\
 \eta_0 &= \eta_s + \frac{cN_A k_B T}{M_w} \lambda_z^2 \sum_{i=1}^{N_m} \frac{1}{i^{2(2+\sigma)}}
 \end{aligned} \tag{3.7}$$

where $\sigma \cong -1.40(h^*)^{0.78}$, k_B is Boltzman's constant, N_A is Avagadro's number, and N_m is the number of modes. The parameter h^* is the hydrodynamic interaction parameter which has a maximum value of 0.25 for a good solvent and a minimum value of 0.0 for an ideal solvent. By fitting the equations above to the experimental data, the longest relaxation time, λ_z , can be calculated. The longest Zimm relaxation times for the polystyrene Boger fluids were found to be 4.1 seconds for PS025 and 160 seconds for SM3, corresponding to increases of 5% and 3% respectively over the values measured by Anna (see Table 3.3).

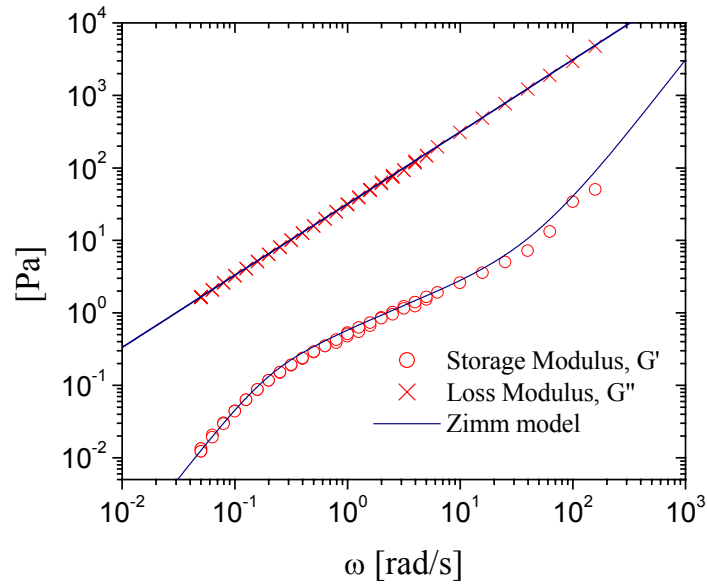


Figure 3.5 Storage and loss moduli of PS025 with Zimm model fit.

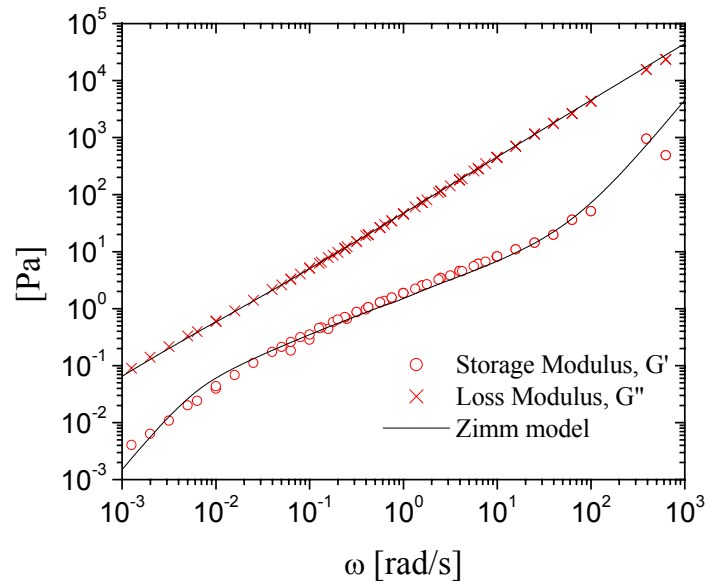


Figure 3.6 Storage and loss moduli of SM3 with Zimm model fit.

	Current results				Results of Anna (1999-2000)			
	η_0 [Pa·s]	λ_z [s]	a_{WLF}	b_{WLF}	η_0 [Pa·s]	λ_z [s]	a_{WLF}	b_{WLF}
PS025	30.3	4.1	16.2	77.0	24.0	3.9	16.4	80.5
SM3	60.0	160	37.3	160	55.5	155	36.9	160
Styrene Oil	33.0	~	~	~	21.9	~	~	~

Table 3.3 Tabulated results of shear rheometry for styrene-based fluids compared with earlier results of Anna [2] for the same fluids.

3.2 Polybutadiene Fluid

A concentrated, entangled polybutadiene (PBd) fluid was mixed by the author in hopes of creating a highly elastic fluid to be used to investigate the elastic fingering instability. A high molecular weight, branched, monodisperse polybutadiene polymer was dissolved in a low molecular weight polybutadiene at a concentration equal to c^{++} to create the fluid. Unfortunately, after the solution was prepared, it was discovered experimentally that the fluid was not significantly elastic to be used in the tests. The fluid was, however, subjected to the same shear rheology tests as the polystyrene fluid. The results of these tests are presented in the following paragraphs.

3.2.1 Fluid Composition

To create the polybutadiene fluid, a quantity of low molecular weight polybutadiene liquid was obtained from Polysciences, Inc. According to the manufacturer, this fluid is composed of 80% 1,2 Polybutadiene and 20% Vinyl, and has molecular weight of 1600. A monodisperse (PDI=1.10), high molecular weight polybutadiene sample was purchased from Polymer Source (Product# P1209-6Abd). This polymer has a molecular architecture that consists of a backbone and six arms (three branches at each end of the backbone). This structure is quite different from the linear molecules of polystyrene solutions, which have only a backbone and no arms, or branches (see Figure 3.7). The molecular weight of the backbone segment molecule is 90.7×10^3 [g/mol] and the arms each have a molecular weight of 30.0×10^3 [g/mol] for a total molecular weight of 270.7×10^3 [g/mol]. This polymer was carefully mixed with the low

molecular weight solution at a concentration of 10 wt%, precisely at c^{++} , in order to create a concentrated, entangled polymer solution (see Graessley diagram, Figure 3.1).

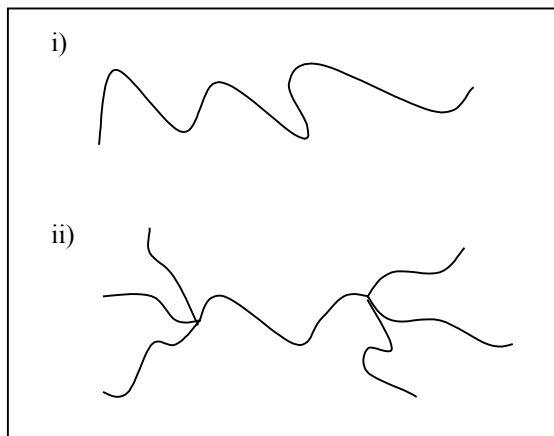


Figure 3.7 Molecular structure of; (i) a linear polymer, and; (ii) a branched polymer.

The high molecular weight PBd was in the form of a solid at room temperature, and had to be dissolved in a solvent for mixing with the oligomeric PBd liquid. In order to mix the two materials, the correct proportions were first carefully weighed using a balance and placed in a glass container of known weight. Next, hexane was then added to act as a solvent to dissolve the polymer. The glass container was then slowly rotated in a water bath at 50° C for one week. After one week, there were no discernable amounts of the solid polymer in the solution. The solution was then placed in a vacuum oven at 50° C and the pressure was slowly reduced by 29 inches-Hg and the hexane was allowed to evaporate. Periodically the chamber was vented and the sample was weighed to check the progress of the evaporation. After one week, the hexane had evaporated so that the weight of the sample was within 1% of the initial combined mass of the oligomer and solid.

3.2.2 *Shear Rheometry*

Both the low molecular weight polybutadiene solvent fluid and the concentrated, entangled polybutadiene solution were subjected to the same viscometric tests as the polystyrene test fluids. The data in Figure 3.8 shows the shear viscosity of the fluid at 25° C as a function of shear rate for the low molecular weight PBd fluid. The fluid exhibits Newtonian behavior by this measure as the shear viscosity varies by less than 1% over two orders of magnitude in shear rate.

Figure 3.9 contains the results of a temperature ramp during steady shear flow for the same fluid. The viscosity decreases logarithmically in temperature and is well modeled by the Arrhenius equation ($\Delta H/R = 1.1 \times 10^4$ [K]).

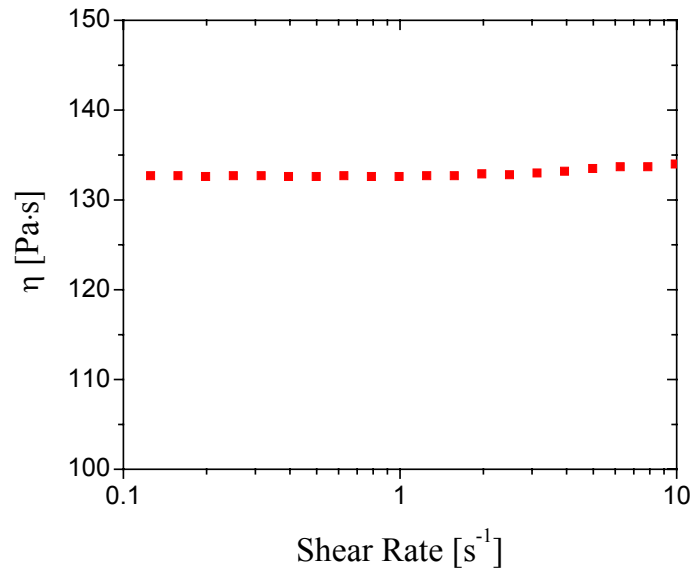


Figure 3.8 Shear viscosity of the low molecular weight polybutadiene as a function of shear rate. The fluid exhibits Newtonian behavior over the range of shear rates tested.

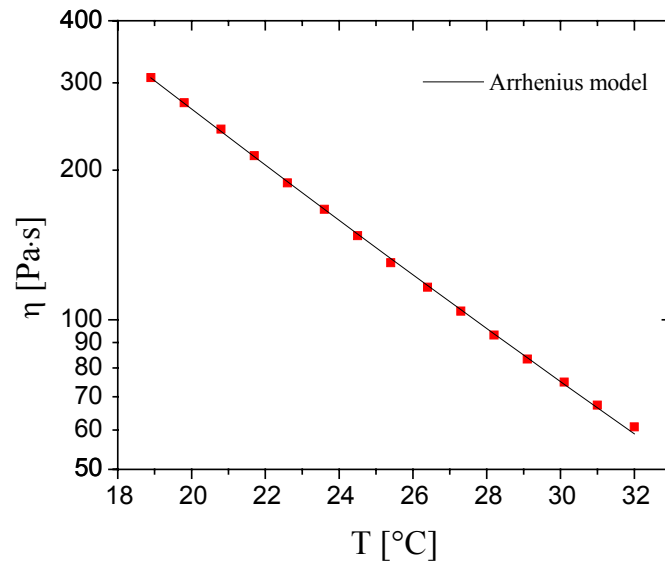


Figure 3.9 Temperature dependence of the shear viscosity for the low molecular weight PBd

The low molecular weight polybutadiene (polymer solvent) was also subjected to oscillatory shear flow in order to probe the linear viscoelastic properties of the fluid. As Figure 3.10 indicates, both the storage and loss modulus are fairly linear in oscillation frequency on the log-log plot, and can thus be approximated by the Maxwell model [5]. From the Maxwell model, the storage modulus, G' , can be written

$$G' = \frac{G_{ps} \lambda_{ps} \omega}{1 + (\lambda_{ps} \omega)^2}, \quad (3.8)$$

and the loss modulus, G'' , can be written

$$G'' = \frac{G_{ps} (\lambda_{ps} \omega)^2}{1 + (\lambda_{ps} \omega)^2}, \quad (3.9)$$

where and the subscript 'ps' stands for polymeric solvent and $G_{ps} = \eta_{ps} / \lambda_{ps}$, the ratio of the viscosity to the relaxation time. Combining Equations 3.8 and 3.9, an estimate of the relaxation time low molecular weight PBd fluid can be found as

$$\lambda_{ps} = \frac{1}{\omega} \frac{G'}{G''} \quad (3.10)$$

From the Maxwell model and the data in Figure 3.10, it was found that the relaxation time of the fluid was $\lambda_{ps} = 5$ ms. This time is much less than the relaxation time either the PS025 fluid or the SM3 fluid. Given that the FISER II filament stretching rheometer can achieve a maximum strain rate of $\dot{\epsilon}_0 = 20 \text{ s}^{-1}$, the maximum Deborah number ($De = \lambda \dot{\epsilon}_0$) achievable with this fluid in a stretching experiment would be $De \approx 0.1$, and Newtonian extensional flow behavior would be expected.

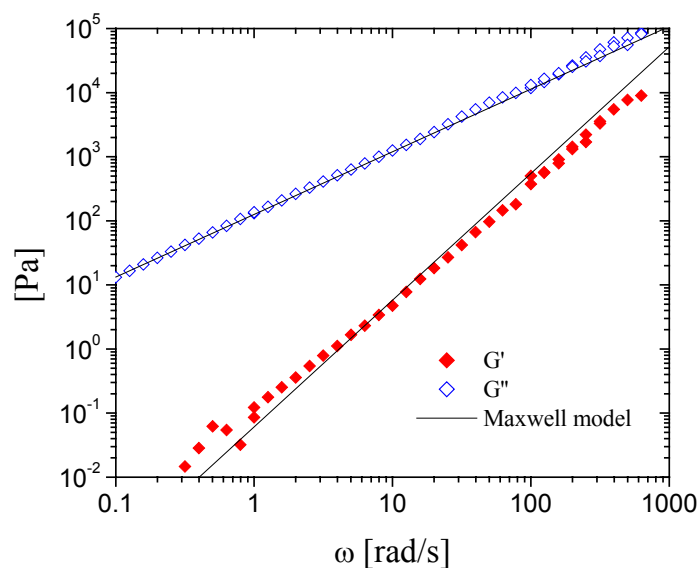


Figure 3.10 Storage and loss moduli of the low molecular weight polybutadiene oligomer and the fitted curves from the Maxwell model.

The shear flow behavior of the concentrated, entangled PBd fluid was quite different than that of the low molecular weight solvent. The zero shear rate viscosity at 25° C was greater by nearly a factor of ten and the fluid was clearly shear thinning (the shear viscosity decreased by nearly 20% over the same range of shear rates). The results of a temperature ramp experiment for the concentrated, entangled fluid, along with a fit curve from the WLF model, are shown in Figure 3.12.

The results of the oscillatory shear experiments on the concentrated, entangled fluid are significantly different than those for the PBd solvent, and the simple Maxwell model can no longer explain the linear viscoelasticity of the fluid. Figure 3.13 contains the experimental data for the storage and loss moduli as well as fit curves generated using Equations 3.7 for the Zimm model. The Zimm model is suited for dilute solutions such as the Boger fluids discussed earlier in this chapter, and is not expected to accurately model a concentrated solution. Nevertheless, the model was used to arrive at a rough estimate for the relaxation time of the fluid. For the fit curves of Figure 3.13, the model yields a relaxation time of $\lambda_z = 500$ ms. This value is significantly larger than the 5 ms relaxation time of the solvent, however, it is still much smaller than the relaxation times of the polystyrene Boger fluids, and the Deborah number corresponding to the maximum possible stretch rate of the FISER II filament stretching rheometer, $\dot{\epsilon} = 20$ s⁻¹, is only $De \approx 10$. A few stretching experiments were made near this maximum Deborah number,

however it was not possible to induce the desired elastic instability. Although possible, extensional rheology testing was not done on this fluid.

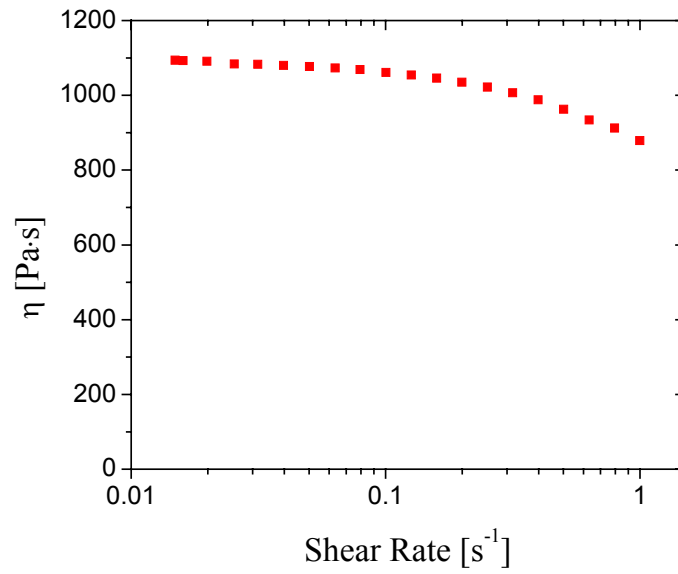


Figure 3.11 Shear viscosity (on a linear scale) of the concentrated polybutadiene fluid as a function of shear rate. The zero shear rate viscosity is $\eta_0=1100$ [Pa·s].

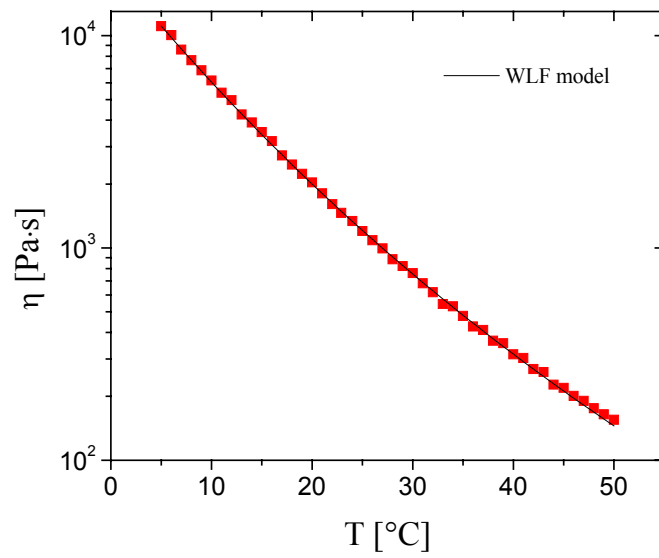


Figure 3.12 Temperature dependence of concentrated polybutadiene fluid and WLF model fit ($a_{\text{WLF}}=14.5$, $b_{\text{WLF}}=151$ °C, $T_0=25$ °C).

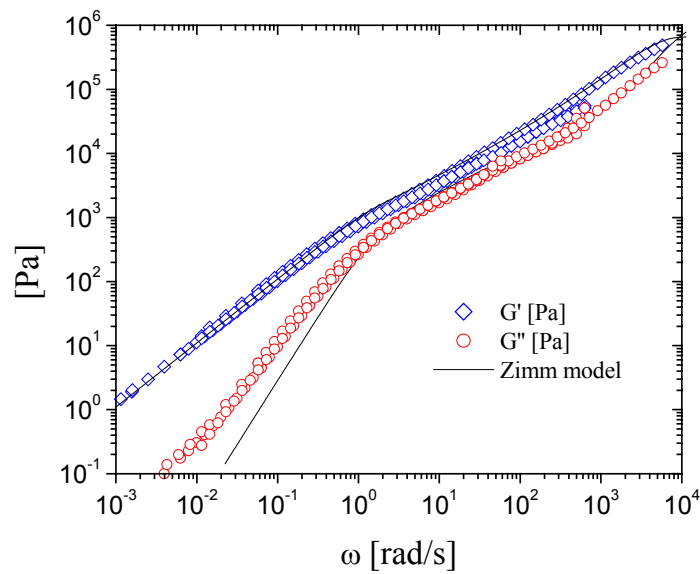


Figure 3.13 Storage and loss moduli of the concentrated polybutadiene and the Zimm model predictions. Note that the Zimm theory is for dilute solutions and, as expected, does not model this concentrated fluid very well. ($\lambda_z=0.5$ [s], $\eta_s=132$ [Pa·s], $\eta_0=1100$ [Pa·s] $h^*=0.1$)

Chapter 4 Experimental Results

This chapter is divided into three sections, one corresponding to each of the two free surface fingering instabilities seen in the experiments, and one section discussing the cavitation observed for very high stretching rates. The experiments were done using the FISER II filament stretching rheometer described in Chapter 2. The test fluids were described in Chapter 3; a Newtonian liquid and two viscoelastic fluids were used to perform stretching experiments over four orders of magnitude in Deborah number and one order of magnitude in aspect ratio.

For the stretching experiments described in this chapter, an exponential velocity profile is used to stretch a thin cylindrical layer of fluid while measuring axial force. Possible endplate instabilities are recorded using the imaging apparatus described in Chapter 2. For a given experiment, a desired constant strain rate, $\dot{\epsilon}_0$, is chosen and the motors are programmed to move according to an exponential position profile,

$$L(t) = L_0 e^{\dot{\epsilon}_0 t}, \quad (4.1)$$

where L_0 is the initial endplate separation distance, or fluid sample thickness. It follows that the velocity is also an exponential function of time:

$$V(t) = \frac{dL(t)}{dt} = L_0 \dot{\epsilon}_0 e^{\dot{\epsilon}_0 t}. \quad (4.2)$$

As explained in Chapters 1 and 2, exponential stretching profiles as defined by Equations 4.1 and 4.2 lead to more uniform kinematics and a nearly constant strain rate in an elongating filament. The axial strain referred to in this thesis is always the Hencky strain [73], defined as the natural logarithm of the ratio of instantaneous length to initial length, or

$$\epsilon \equiv \ln \frac{L(t)}{L_0} \quad (4.3)$$

Unless otherwise indicated, the Hencky strain referred to in this chapter is always based on the commanded position of the endplates. When an ideal exponential stretch with a constant strain rate is implemented (which is indeed the case in the current experiments), the Hencky strain can be written as the product of the initial strain rate and the elapsed time, so that

$$\epsilon = \dot{\epsilon}_0 t. \quad (4.4)$$

When a viscoelastic liquid is stretched, the response may be considered viscous, elastic, or somewhere in between, depending on the stretch rate and the fluid relaxation time. The Deborah number, described in Chapter 1, is a way of quantifying the nature of the fluid response *a priori*. The Deborah number is defined as the ratio of the fluid time scale, λ , to the experiment time scale, $\dot{\epsilon}_0$, and is written

$$De = \lambda \dot{\epsilon}_0. \quad (4.5)$$

For $De < 1$, purely viscous fluid behavior can be expected, while a large Deborah number signifies that the fluid will behave more like an elastic solid than a liquid when it is deformed.

For the elastic instabilities investigated in this work, the Deborah number is an appropriate description of the experimental flow conditions. For the Saffman-Taylor fingering instability, which can occur in purely viscous liquids, the capillary number is more appropriate. The capillary number, as mentioned in Chapter 1, is a ratio of viscous forces to capillary forces, or surface tension. The capillary number as it applies to reverse squeeze flow can be written

$$Ca = \frac{\mu V_r}{\sigma}, \quad (4.6)$$

where μ is the shear viscosity, V_r is the bulk radial velocity, and σ is the surface tension.

Besides the strain rate $\dot{\epsilon}_0$, which can be chosen as desired, the other variable experimental parameter is the initial aspect ratio, Λ_0 , which is defined as the ratio of the initial sample height to the initial sample radius, or

$$\Lambda_0 \equiv \frac{L_0}{R_0} \quad (4.7)$$

In Chapter 2 it was mentioned that aspect ratios used in filament stretching rheometer are typically $\Lambda_0 \sim O(1)$, with the initial sample thickness being about 3mm. Material thicknesses as low as 25 microns are used in probe-tack tests of pressure-sensitive adhesives. The current experiments were performed using aspect ratios of $0.04 \leq \Lambda_0 \leq 0.40$, which, for the 5mm endplates, correspond to sample thicknesses between 0.10mm and 1.00mm. Altering the initial aspect ratio can have a large effect on the development of instabilities during stretching, as explained later in the chapter.

4.1 Elastic Fingering Instability

The series of images in Figure 4.1 correspond to a stretch using the SM3 fluid at a Deborah number of $De=66$, and initial aspect ratio, $\Lambda_0 = 0.40$. Thus, with 5mm diameter endplates, the initial fluid sample thickness is 1mm. In the lower portion of each picture, the reflection of the fluid column on the beamsplitter can be seen. As the stretch in Figure 4.1 begins, a filament, or stable fluid column, begins to develop. The column continues to grow until at some strain ($\varepsilon \approx 3.47$ in this case), the onset of the elastic fingering instability occurs.

This instability is marked by the outward radial growth of fingers from the base of a previously stable and axially symmetric fluid column. As the instability progresses, the initial fingers can bifurcate and branch as in Figure 4.1, forming complex geometries and developing fibrils, or small strands of material. At the end of the stretch, the sample fails elastically, either far from the endplate or near to it, as in Figure 4.1, and the fluid recoils back to the endplate. This behavior does not occur when Newtonian liquids are stretched because such fluids do not develop the requisite elastic stresses.

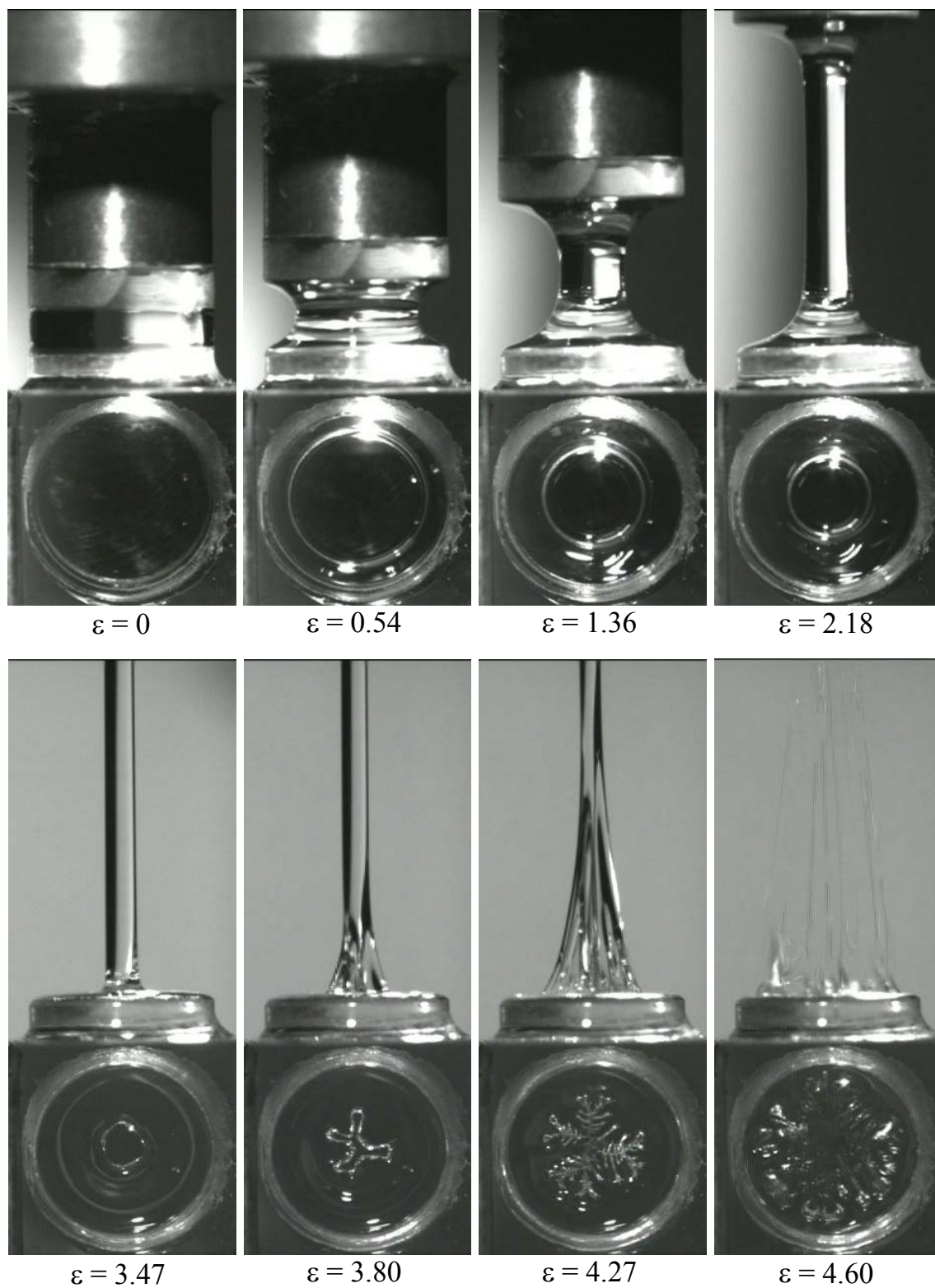


Figure 4.1 The elastic fingering instability seen in the series of images above occurs during an exponential stretching experiment with the SM3 fluid at a $De=66$ and $\Lambda_0=0.40$.

4.1.1 Background

The elastic fingering instability was first studied in the filament stretching geometry by Spiegelberg and McKinley [60] (see Figure 4.2), but the phenomena is not unlike the patterns formed when an adhesive layer is strained and fibrils form [32], [35], [33]. The apparent link between the two phenomena is strengthened when one considers that the flow within the stretched fibrils of an adhesive layer is primarily a uniaxial elongational flow. Spiegelberg and McKinley studied the elastic instability using a set of three polystyrene Boger fluids (different than those used herein). All of the fluids were composed of a monodisperse polystyrene with $M_w = 2.25 \times 10^6$ [g/mol] in a solution of styrene oil. Table 4.1 contains relevant data regarding the fluids used in that study.

Fluid	M_w [g/mol]	η_0 [Pa·s]	λ [s]	σ [N/m]
PS-05	2.25×10^6	47.7	0.78	0.029
PS-1	2.25×10^6	52.0	0.73	0.029
PS-2	2.25×10^6	70.4	0.52	0.029
PS Oil	2.25×10^6	37.0	~	0.029

Table 4.1 Fluid properties for the test fluids used in the 1996 study by Spiegelberg and McKinley [60]. All fluids were polymer solutions comprised of a monodisperse polystyrene in a solution of styrene oil. (Note: the relaxation time, λ , is a mean relaxation time computed from viscometric properties).

The study by Spiegelberg and McKinley resulted in an approximate theory for the critical Hencky strain for the onset of the instability based on critical conditions for stability of a receding meniscus for a given Deborah number. This theory proposes that the instability occurs when elastic tensile forces result in a negative pressure in the fluid near the endplates that is large enough to overcome stabilizing surface tension forces. This theory and its relevance to the current experiments are discussed later in this chapter.

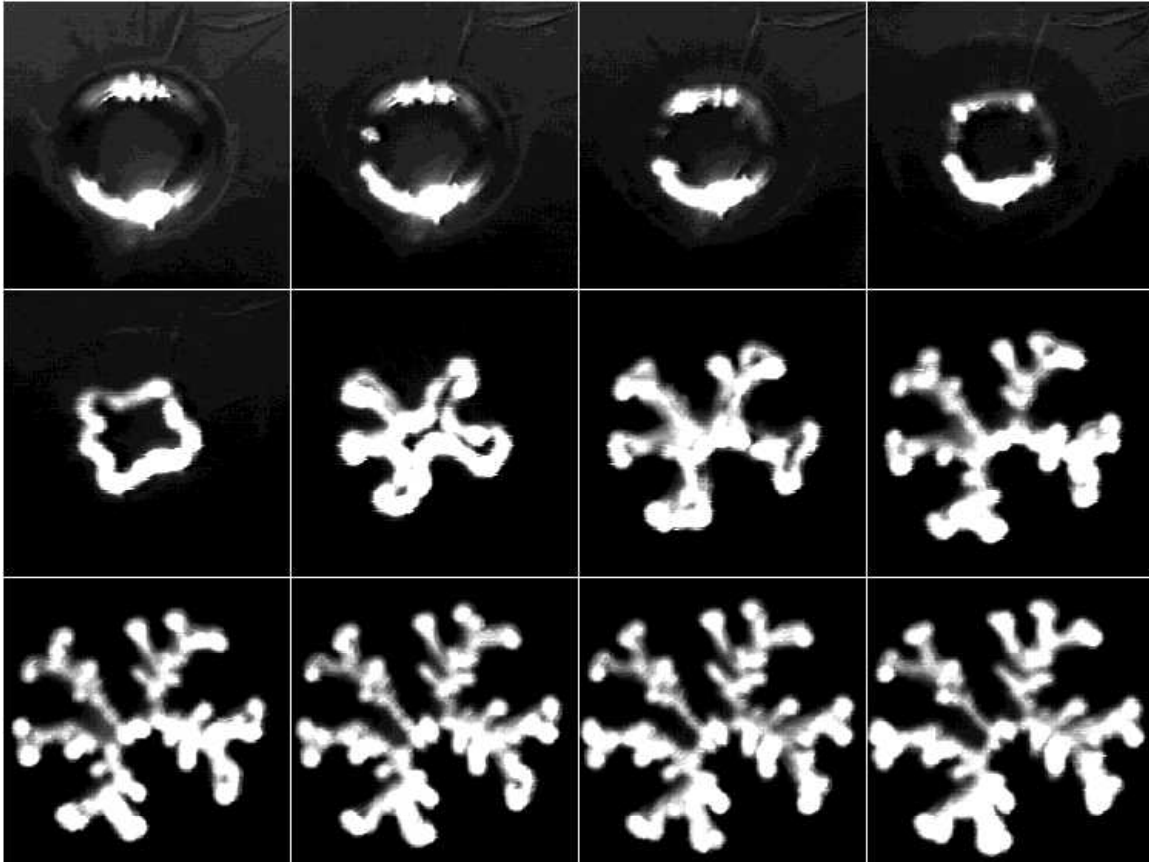


Figure 4.2 A series of images showing development of the elastic fingering instability in 0.05 wt% polystyrene Boger fluid (PS05) as viewed from beneath the endplate in the axial direction. Note that as the instability progresses the fingers bifurcate repeatedly. Reproduced with permission from [60]. Copyright 1996 Elsevier.

Numerical simulations carried out by Rasmussen and Hassager [74] presented numerical results predicting the growth of the elastic fingering instability in the filament stretching flow geometry as well as the pressure field in the fluid near the endplate (see Figure 4.3). However,

these simulations disregarded surface tension, with the effect of there being no preference of lower mode numbers, i.e., perturbations of high mode numbers grew as rapidly as low mode numbers. A more recent publication by the same authors considered the same problem, but included the role of surface tension in the simulations. The results indicate that surface tension can indeed act to reduce the number of fingers (or modes) observed to 3-5 modes [75].

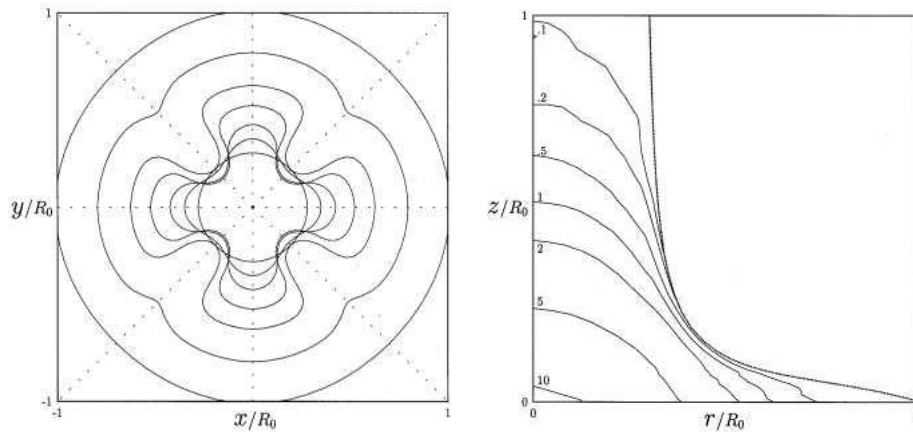


Figure 4.3 Simulations of development of instability cross-section (left), and stress contours near the endplate (right). Reprinted with permission from [74]. Copyright 2000 The Society of Rheology.

In recent filament stretching experiments by Bach *et al.* [76] using a concentrated, entangled polystyrene solution, the investigators were able to control the number of modes in the elastic instability by introducing perturbations through the geometry of the endplates. An instability having an induced mode number of 4 is shown in Figure 4.4.

While previous research has made steps towards understanding the critical strain at the onset of the instability as well as the growth of the initial fingers, there are still many unanswered questions. For example, the causes of the finger bifurcation and branching are still unknown. In addition, the exact mechanism of the instability onset has yet to be explained.

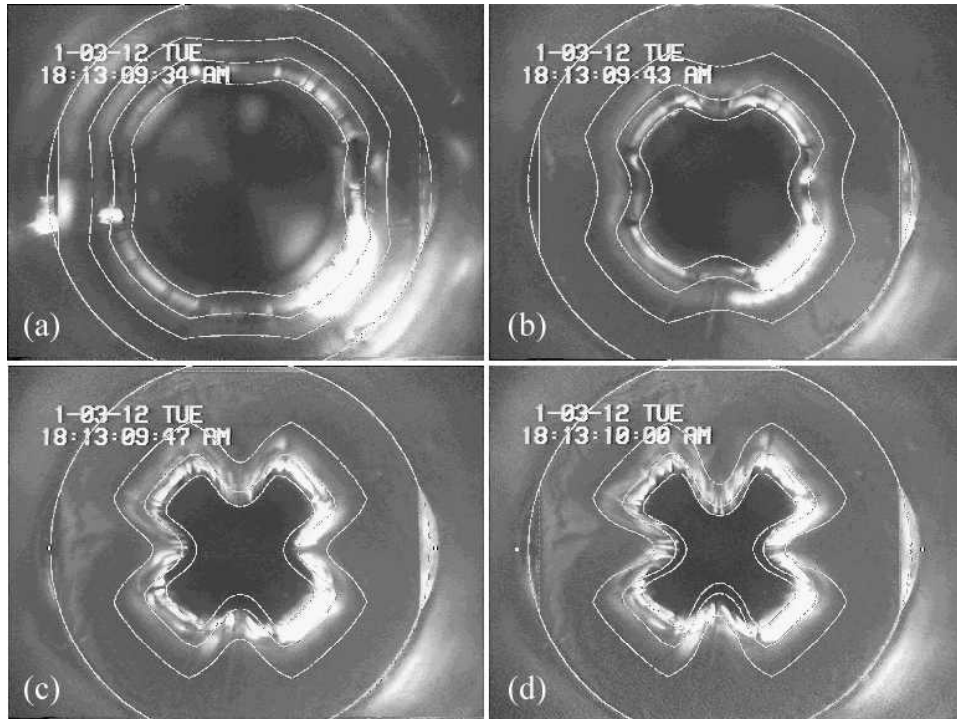


Figure 4.4 Photographs of induced 4-mode elastic fingering instability in a solution of 12% polystyrene in a tricresyl phosphate (TCP) solvent. The white overlaid contours are the results of numerical simulations of the experiment. Note that endplate is not circular, but has four axisymmetric notches. Reproduced with permission from [76].

4.1.2 Results and Discussion

The experiments undertaken for this thesis are an extension of the previous investigations of the elastic instability and concentrate on the effects of varying the initial aspect ratio and the Deborah number. When the Boger fluids are stretched rapidly, i.e., at large Deborah numbers, large elastic tensile stresses can develop. This strain hardening effect can be seen Figure 3.2, in which the Trouton ratio vs. Hencky strain was plotted for an extensional rheometry experiment. Such flow-induced elastic stresses are the driving force behind the elastic fingering instability. The sequence of images in Figure 4.1 shows the onset and development of the elastic instability during exponential stretching. In the early stages of the stretch, a stable, cylindrical fluid column forms. As the plates continue to separate, this fluid column increases in length and decreases in diameter as required for volume conservation. It should be noted that the onset of the elastic

instability occurs when almost all of the fluid at the endplates has been sucked into the column. This is typical of the development of the instability in stretching experiments in which the purely elastic instability occurs prior to any of the other observed flow instabilities, i.e., for larger aspect ratios and moderate Deborah numbers.

The data plots of Figure 4.5 contain measured force and radius data for the stretching experiment shown Figure 4.1. It is obvious from the tensile force data in Figure 4.5 and the corresponding images that the fluid in the column has already begun to strain harden at the onset of the elastic instability. At larger strains, as the fingers continue to grow, the tensile force in the column increases very rapidly.

The lower part of Figure 4.5 contains measured radius data for the experiment. As is typical for extensional rheometry data, the radius is not a straight line of slope $-1/2$, as it would be for the ideal elongation of an incompressible cylinder. This is because a thin layer of fluid coating the endplates remains during the stretch due to a condition of no slip. These ‘reservoirs’ of fluid at the endplates cause the radius to decrease in a nonhomogeneous manner with respect to the axial direction. Although the midpoint radius does decrease exponentially, the true strain of the material elements near the midpoint of the filament cannot be predicted exactly from the axial, or command strain, as it could be done for ideal elongation of an incompressible cylinder.

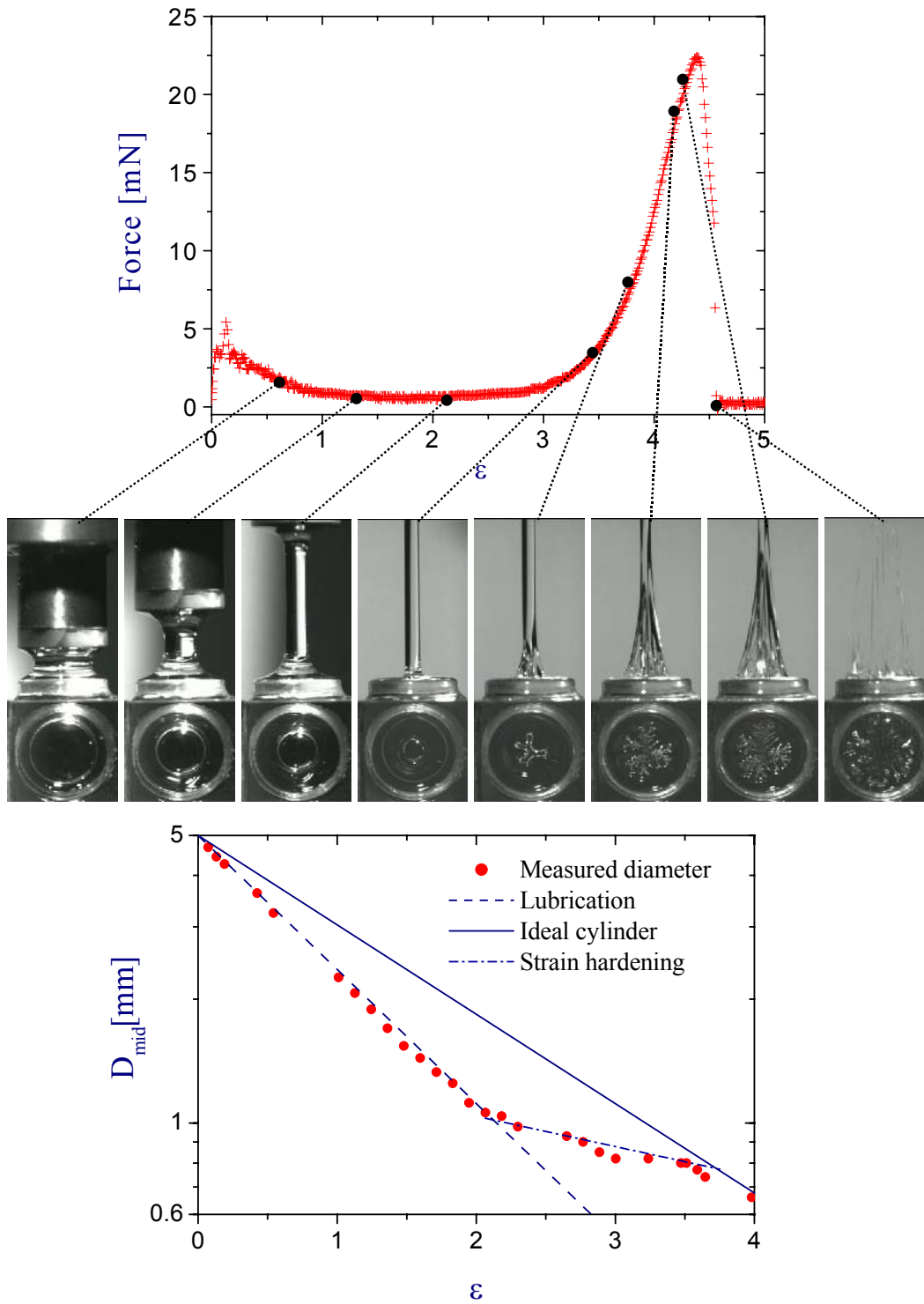


Figure 4.5 Measured axial force (a) and radius (b) as a function of Hencky strain. Note that the instability occurs as the fluid begins to strain harden, i.e., as the tensile force increases rapidly, and when the actual diameter at the midpoint re-approaches the curve predicted from the ideal elongation of a cylinder.

It is clear from Figures 4.1 and 4.5 that the elastic instability occurs when nearly all of the fluid remaining at the endplates is pulled into the axially uniform fluid column, and when curvature at the base of the column is very large. At the end of the column, near an endplate, there is a small region in which strained fluid with high axial tension is matched to a thin layer of relatively unstrained fluid. One possible interpretation is that the elastic instability occurs when more energy is required to drive a radial shear flow over an increasingly thin fluid layer than to stretch and strain harden the fluid surrounding the base of the column. At moderate Deborah numbers, the elastic instability is energetically more preferable than the onset of cavitation at the endplate (cavitation can occur at larger Deborah numbers) and to necking or fracture of the fluid column. A possible mechanism for the instability is shown schematically in Figure 4.6. When the macromolecules in these polymer solutions are stretched, the molecules, or polymer chains behave as a series of loosely interconnected springs, resulting in elastic tension along the streamlines. This is an assumption of the Zimm model for dilute solutions [5] and it is the mechanism responsible for flow phenomena like the Fano flow and the Weissenberg effect described in Chapter 1.

For polymers, there is a higher entropy and lower free energy associated with being in equilibrium configuration. Just prior to the occurrence of the elastic fingering instability, the streamlines at the base of the fluid column experience a very high curvature because the thin layer of relatively unstrained fluid coating the endplate is coupled to the elastic column over a very short distance. This results in fluid flow around a curvature of very small radius (see Figure 4.6). All of these streamlines around the circumference of the column base would prefer, energetically, to straiten and thus eliminate the high curvature. Since the fluid is incompressible, this cannot happen unless cavitation occurs. Before cavitation occurs, however, portions of the fluid at the column base and at periodic angular coordinates do eliminate the large curvature, pulling surrounding fluid from the thin layer as they grow. This is the onset of the elastic fingering instability. As the instability continues to progress, this mechanism repeats on a smaller and smaller scale until the filament ruptures, usually at a point far from the endplate.

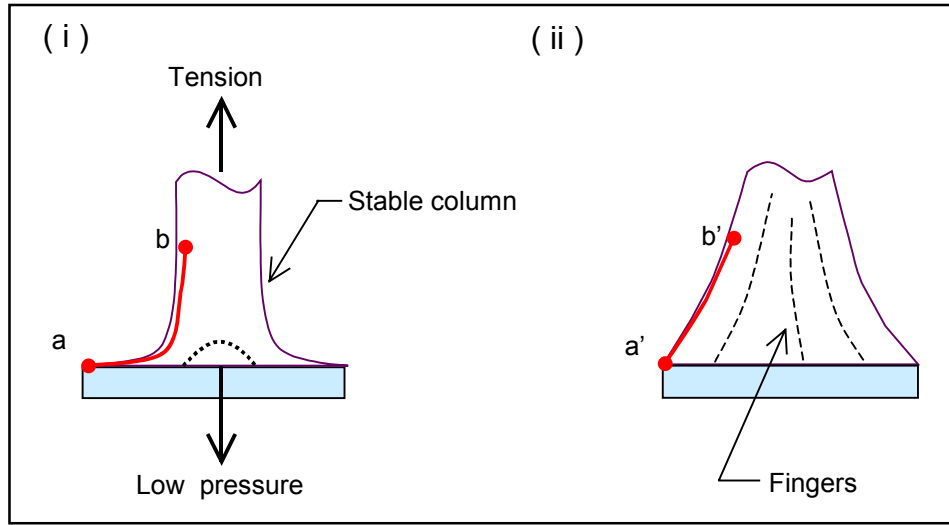


Figure 4.6 Hypothetical sketch of fluid streamlines and elastic tension: (i) before onset of instability, and (ii) immediately after instability.

It is desirable to predict when, or if, the elastic fingering instability will occur in an experiment for a given Deborah number because the onset of the elastic instability determines the point at which the useful part of an extensional rheometry experiment is over. This was the aim of the theory of Spiegelberg and McKinley [60] that was mentioned in a previous paragraph. This theory predicts that the instability should occur when the radial pressure gradient at the endplate becomes greater than the stabilizing forces of surface tension, or when

$$\frac{dP}{dr} \geq \sigma \alpha^2, \quad (4.8)$$

where $\alpha = m/R_0$ and m is the mode number of the initial instability and R_0 is the endplate radius. However, in the current study it was observed experimentally that fingers grow from the base of the column, where the radius is very close that of the column midpoint. Thus a substitution was made in the original theory and the radius used in Equation 4.8 is not the initial, or endplate radius, but the radius found by conservation of volume, or

$$R = R_0 e^{-\dot{\epsilon}_0 t/2} \quad (4.9)$$

and α is then written

$$\alpha = \frac{m e^{\dot{\epsilon}_0 t/2}}{R_0}. \quad (4.10)$$

Dimensional analysis leads to a pressure gradient that is proportional to the axial stress in the filament, or

$$\left. \frac{dP}{dr} \right|_{z=0} \sim \left. \frac{\pi_{zz}}{R} \right|_{z=L(t)/2}, \quad (4.11)$$

From the Oldroyd-B constitutive model [5], an approximation of the tensile stress in the filament for $De > 1/2$ can be written

$$\pi_{zz} \sim \frac{2\eta_p \dot{\epsilon}_0}{De-1} e^{\left(2-\frac{1}{De}\right)\dot{\epsilon}_0 t}, \quad (4.12)$$

where $De = \lambda \dot{\epsilon}_0$. By combining Equations 4.10, 4.11 and 4.12, an estimate of the critical strain required for the onset of the instability can be written as

$$\varepsilon_c = (\dot{\epsilon}_0 t)_{crit} = \frac{\ln(K\sigma/(GR_0)) + \ln(1-(2De)^{-1})}{3/2 - De^{-1}}, \quad (4.13)$$

where $G = \eta_p/\lambda$ is the elastic modulus in the Oldroyd-B model, and K is a constant of order one that is related to the most unstable wave number and should be a constant of proportionality in Equation 4.11 [60]. Figure 4.7 is a plot of the critical strain vs. aspect ratio the data. This plot contains data from the current experiments (for PS025 and SM3) as well as the data for the earlier experiments of Spiegelberg and McKinley for the fluids listed in Table 4.1. The solid curve in this plot was generated using Equation 4.13. Since all of the fluids have different moduli of elasticity, G , a slightly different value of K is required for each fluid so that the curves collapse to a single line.

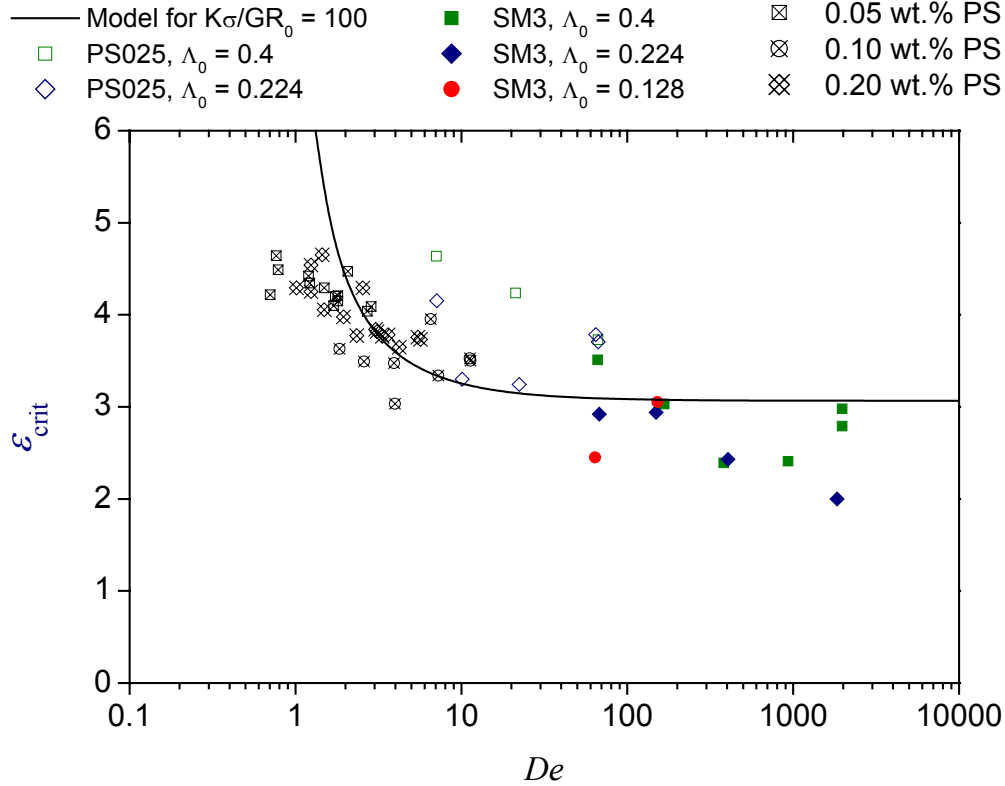


Figure 4.7 Critical Hencky strain vs. Deborah number. Comparison of results of current experiments with those of Spiegelberg & McKinley (1996). The solid line represents the prediction of Equation 4.13.

Another approach at predicting the critical strain for the onset of the elastic instability takes advantage of the experimental observation that the instability occurs when most of the fluid disappears from the endplate and only a thin layer of fluid remains. From Figure 4.5, it can be noted that this strain occurs roughly when the radius data again approaches the ideal radius curve, which is based the deformation of an ideal cylinder. The experimental radius data in Figure 4.5 is shown along with the radius calculated from lubrication theory. At the beginning of the experiment, the data follows the lubrication solution, which has a slope of $-3/4$ on a log-log plot. This has been observed for some time in filament stretching experiments and appears to be valid in general up until strains of $\varepsilon \approx 2$ [77], [78]. It has also been observed that the slope of the radius data beyond the strain at which the lubrication theory no longer applies can be approximated as being $-0.8 \dot{\varepsilon}_0$ [78]. These heuristic approximations of the mid-filament radius can be used to arrive at a prediction for when the elastic instability will occur, which has been done for the experimental data in Figure 4.5. It should be noted that one of the primary unsolved

problems in extensional rheology is to predict the deviation of the actual radius curve from ideal radius curve.

4.2 Saffman-Taylor Fingering Instability

When the aspect ratio is reduced, it is observed that fingers of air penetrate the fluid and move radially inwards at the start of the experiment (see Figure 4.8). This is in contrast to the elastic instability in which the fingers occur at rather large strains and grow radially outward. In addition, this phenomenon occurs in both the Newtonian and the viscoelastic liquids. This flow instability is very similar to the classic Saffman-Taylor fingering instability observed in Hele-Shaw cells.

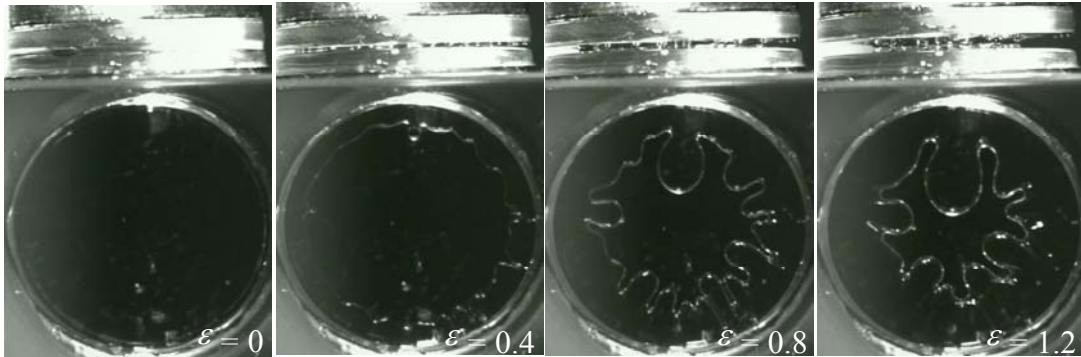


Figure 4.8 Saffman-Taylor instability in a Newtonian liquid: Styrene oil with $\dot{\epsilon}_0 = 0.24\text{s}^{-1}$, $\Lambda_0 = 0.036$, and $Ca/\Lambda_0^2 = 1000$. The instability occurs just as the plates begin to separate, when the radial pressure gradient is greatest.

The Saffman-Taylor fingering instability is an interfacial instability that occurs when a less viscous fluid pushes a more viscous fluid in pressure driven flow [43]. At the onset of the instability, fingers of the less viscous fluid begin to penetrate the more viscous fluid in the streamwise direction (see Figure 4.9).

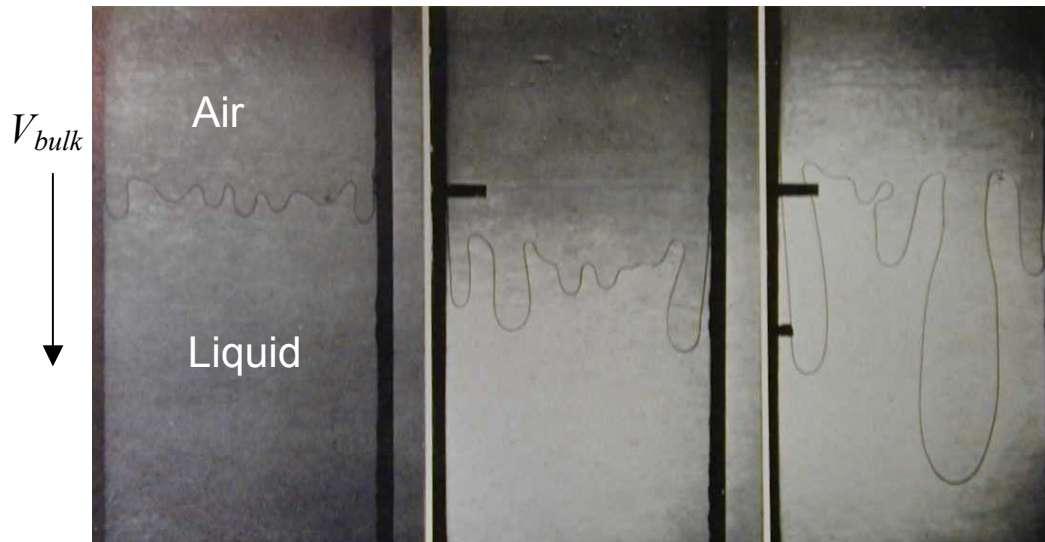


Figure 4.9 Sequence of three images showing the Saffman-Taylor instability in which fingers of a less viscous fluid (air) penetrate a more viscous fluid (glycerine) in pressure driven flow [43]. The images go from left to right in time and the direction of bulk flow is from top to bottom.

A three-dimensional variation of this instability that is quite similar to the instabilities seen in the current experiments has been observed when fluid between two plates is subjected to reverse squeeze flow in a gaseous atmosphere, and the fluid front must move inward to conserve volume. [53]. This same situation can occur when a glass is lifted from a wet countertop. In the following discussion, a theoretical explanation of this viscous flow instability is provided and a prediction of the critical conditions for the onset of the instability is presented.

4.2.1 Planar Saffman-Taylor Instability

When a less viscous liquid moves behind a more viscous liquid in planar flow, such as the flow in a Hele-Shaw cell, the interface between the two fluids is unstable to perturbations. This instability is perhaps best explained using the diagram in Figure 4.10. If an exaggerated perturbation is imagined, such as the one at the top of the figure, it is obvious that the fluid to each side of the point $P+$ (in the directions perpendicular to the flow) are at a lower pressure. This is illustrated by the lower portion of Figure 4.10, which shows the linear pressure drop expected for a Newtonian fluid flowing in a channel. Moving in the flow direction, the difference

in viscosities causes a larger pressure drop at point P^- than at point P^+ , two positions which are parallel along the flow axis.

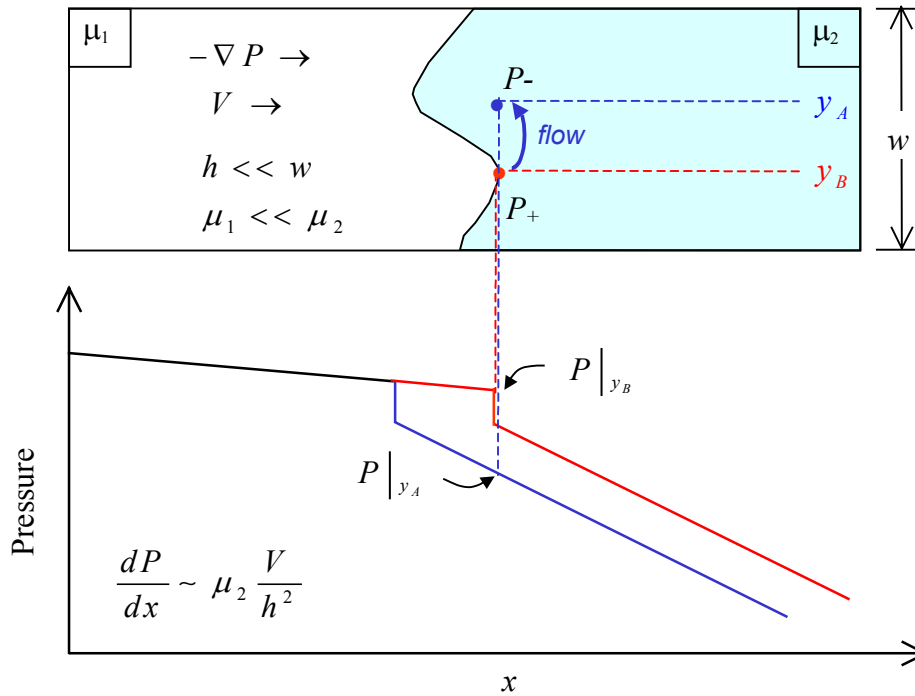


Figure 4.10 Sketch of instability mechanism in Hele-Shaw cell channel flow for a Newtonian fluid of viscosity μ_2 being displaced by a less viscous fluid (such as air) with a viscosity μ_1 . In the figure, V is the bulk velocity, P is the hydrostatic pressure, and h is the channel depth

The Saffman-Taylor instability can also occur in a radial geometry, such as when air is blown into a Hele-Shaw cell causing diverging fingers (see Figure 4.11) or when fluid is removed from a Hele-Shaw cell allowing converging air fingers to penetrate the more viscous fluid [45].

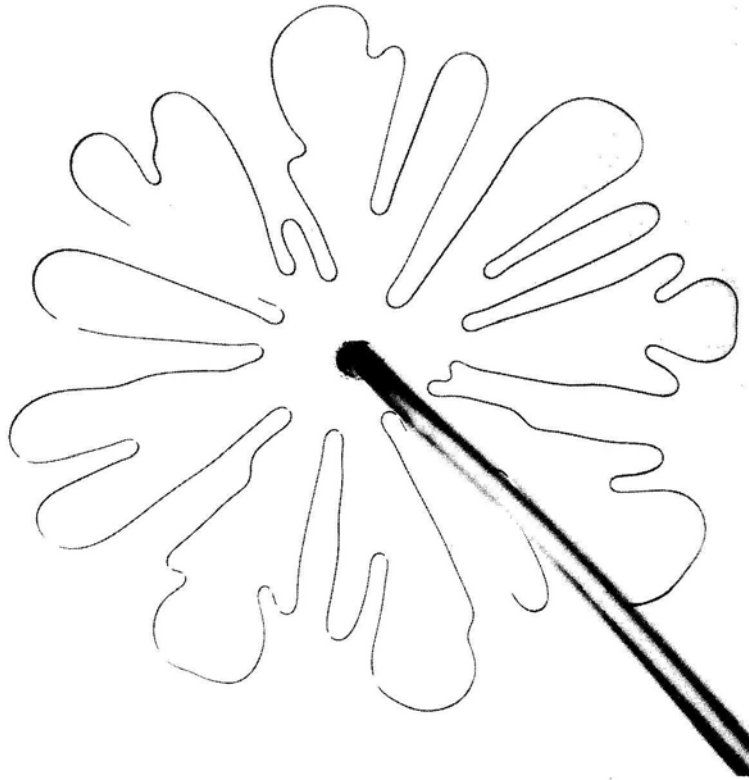


Figure 4.11 Diverging radial Saffman-Taylor instability in a Hele-Shaw cell [45]. Air is injected into a Hele-Shaw cell filled with glycerin, forming fingers that move radially outward.

Both Paterson [45] and Bataille [79] studied the case of converging air fingers penetrating a Newtonian liquid in a Hele-Shaw. These studies resulted in a theory predicting the onset of the instability and the number of fingers, or modes that can be expected. Because of the geometrical similarity to the three dimensional Saffman-Taylor instability observed in the current experiments, the theory for the two-dimensional case serves as a basis from which the theory for the more complicated, three dimensional instability can be adapted. The following paragraphs describe the theory of the planar, radial Saffman-Taylor instability in a Newtonian fluid according to Paterson and Bataille.

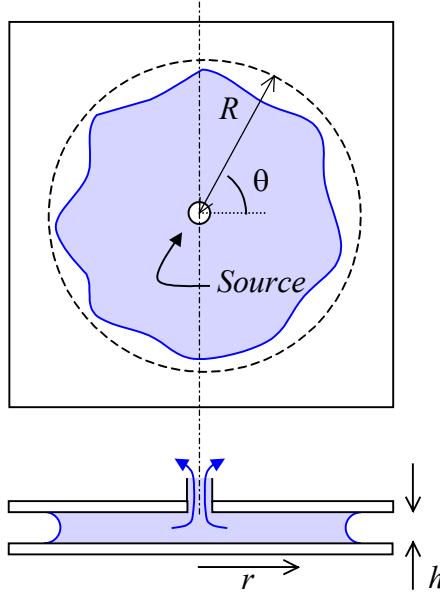


Figure 4.12 Radial Hele-Shaw geometry. If a less viscous fluid is injected at the source, diverging fingers will develop. If instead, liquid is pumped out at the source, converging fingers of the surrounding, less viscous fluid will develop.

From Darcy's law for radial flow, the pressure profile in the liquid is written

$$P(r) = P_0 - \frac{6\mu Q}{\pi h^3} \ln(r/R), \quad (4.14)$$

where P_0 is the atmospheric pressure, μ is the liquid viscosity, h is the cell gap (small compared with the liquid radius), R is the actual fluid radius, r is the radial coordinate, and Q is the volumetric flow rate. The mean radial velocity V_r can be deduced from the flow conservation to be:

$$V_r = \frac{Q}{2\pi R h} \quad (4.15)$$

It follows from Equations 4.14 and 4.15 that the pressure gradient, ∇P_r , at the edge of the liquid disc is

$$\nabla P_r = \frac{12\mu V_r}{h^2}. \quad (4.16)$$

Taking the linear perturbation derivation from Paterson in which an initial circular shape destabilizes into a n mode oscillatory form:

$$r(\theta, t) \rightarrow r(t) + a f(t) e^{in\theta}, \quad (4.17)$$

where a is the initial amplitude (small compared with R) and $f(t)$ is the relative expansion of the perturbation. A linear perturbation analysis leads to the exponential growth with the characteristic rate α_n , so that

$$f(t) = e^{\alpha_n t}. \quad (4.18)$$

This growth rate has been derived independently by both Paterson and Bataille and is given by the following relation:

$$\alpha_n = \frac{n-1}{R_0^2} \left(R V_r - \frac{n(n+1)\sigma h^2}{12 \mu R} \right) \quad (4.19)$$

Two dimensionless parameters that can be defined in this expression are the initial aspect ratio Λ_0 , (an expression of the degree of confinement of the liquid) and the capillary number Ca (which compares viscous dissipation to surface tension):

$$\Lambda_0 = \frac{h}{R} \quad \text{and} \quad Ca = \frac{\mu V_r}{\sigma} \quad (4.20)$$

Using this notation, the characteristic time can be written

$$\alpha_n = (n-1) \left(1 - \frac{n(n+1)}{12} \frac{\Lambda_0^2}{Ca} \right) \frac{V_r}{R}. \quad (4.21)$$

The perturbation grows only if $\alpha_n > 0$, and from Equation 4.21, the critical mode number, n_c , can be written

$$n_c = \sqrt{12 \frac{Ca}{\Lambda^2} + \frac{1}{4}} - \frac{1}{2}. \quad (4.22)$$

The fastest growing mode (maximum value of α_n in Equation 4.21) corresponds to the mode number n_m :

$$n_m = \sqrt{4 \frac{Ca}{\Lambda^2} + \frac{1}{3}}. \quad (4.23)$$

Experimentally, Paterson observed n_m modes, or fingers, growing just at the onset of the instability. Since the front contracts, the total number of fingers decreases, and only the more developed fingers keep growing so that eventually one finger dominates and reaches the source. This final development of the instability is of course beyond the scope of a linear stability analysis.

4.2.2 *Scaling Arguments for 3-D Radial Case*

At the start of a stretching experiment, the endplates begin to separate and fluid must move radially inward to conserve volume. If a cylinder of an incompressible material is deformed in a way that maintains a cylindrical shape, conservation of volume dictates the following relation between the cylinder length and radius:

$$\frac{1}{L} \frac{dL}{dt} = -\frac{2}{R} \frac{dR}{dt}. \quad (4.24)$$

In the case of the current experiments, the fluid element does not maintain a purely cylindrical shape as the endplates separate. Due to a condition of no slip, the fluid takes on an hourglass-like shape. Nevertheless, an approximation of the bulk radial velocity at the start of the stretch can be made by recognizing that the term on the left side of Equation 4.24 is the strain rate, by definition, so that:

$$V_r \approx \frac{dR}{dt} = -\frac{\dot{\epsilon}_0 R_0}{2}. \quad (4.25)$$

The pressure profile resulting in reverse squeeze flow for a Newtonian fluid can be gotten by the classical lubrication approximation [42]:

$$P(r, t) = P_0 - \frac{3\mu}{L^3} \frac{dL}{dt} (R_0^2 - r^2) \quad (4.26)$$

This parabolic profile is quite different from the logarithmic one derived from Darcy's law in a Hele-Shaw cell given by Equation 4.14. However, as Figure 4.13 indicates, the pressure gradient at the edge of the liquid disc *is* the same in both cases, and

$$\nabla P_r|_{r=R_0} = 6\mu \frac{R_0}{L^3} \frac{dL}{dt} = 6\mu \frac{1}{\Lambda_0^2} \frac{\dot{\epsilon}_0}{R_0} = 12\mu \frac{V_r}{L^2}. \quad (4.27)$$

Since the initial pressure gradient at the front is the same in the two situations, it is expected that the relation of Equation 4.23 is a good indicator of the number of fingers observed in reverse squeeze flows. Thus, a larger number of fingers are expected for higher strain rates or smaller aspect ratios (more confined environment), since these conditions lead to larger pressure gradients.

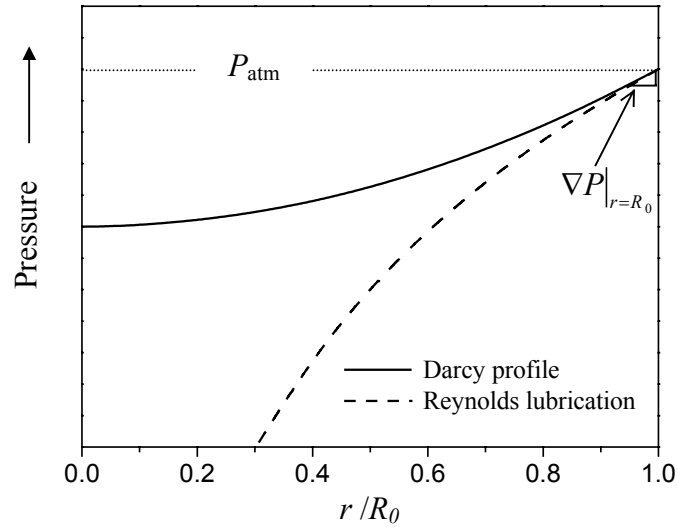


Figure 4.13 Comparison of the radial pressure profiles in the liquid from Darcy’s Law and Reynolds lubrication theory. The two equations result in the same pressure gradient at the front.

Combining Equations 4.20 and 4.25, the initial radial capillary number can be expressed as

$$Ca_0 = \frac{\mu R_0 \dot{\epsilon}}{2\sigma}. \quad (4.28)$$

The number of fingers observed experimentally is plotted in Figure 4.14 against the initial value of Ca_0/Λ_0^2 . It appears that Equation 4.23 overpredicts the actual number of fingers by a factor of about 2. In addition, fingers are observed beyond a critical value of this ratio, or at $Ca_0/\Lambda_0^2 \approx 350$. In contrast to the Hele-Shaw geometry in which the gap between the two plates

is constant, the gap in the current experiment changes as a function of time. Following the results from the linear perturbation derivation, the viscous instability of mode number n grows with the characteristic growth rate α_n . However, as this instability grows, the distance between the endplates gets larger, and the pressure gradient decreases according to lubrication theory. Thus the initial fastest growing finger may not remain the fastest as the stretch progresses. The growth rate, α_n , depends of the actual value of the ratio Ca/Λ^2 , i.e., the growth rate depends on time. In the following section, this aspect is considered in order to derive the growth rate of the perturbations in reverse squeeze flow.

In Paterson's derivations, the evolution of the amplitude of an n mode instability is given by:

$$\frac{df}{dt} = \alpha_n(t) f(t) \quad (4.29)$$

Since the pressure gradient at the edge is the same for reverse squeeze flow as for the Hele-Shaw cell geometry, it is assumed as a first approximation that the growth rate given by Equation 4.19 holds true at small times, if plate separation, average front radius and the bulk radial velocity are expressed as functions of time. Using the derivation of the bulk radius from volume conservation from Equation 4.9, these quantities can be written:

$$V_r \sim -\frac{1}{2} R_0 \dot{\epsilon} e^{-\dot{\epsilon}_0 t/2} \quad (4.30)$$

$$Ca \sim Ca_0 e^{-\dot{\epsilon}_0 t/2} \quad (4.31)$$

$$\Lambda \sim \Lambda_0 e^{\frac{3}{2}\dot{\epsilon}_0 t} \quad (4.32)$$

The transient growth rate can then be written:

$$\alpha_n = (n-1) \left(\frac{1}{2} - \frac{n(n+1)}{24} \frac{\Lambda_0^2}{Ca_0} e^{\frac{7}{2}\dot{\epsilon}_0 t} \right) \dot{\epsilon}_0 \quad (4.33)$$

The amplitude of the n^{th} mode can finally be evaluated by integrating the Equation 4.33:

$$f(t) = \exp\left(\int \frac{dt}{\alpha_n(t)}\right) = \exp\left[(n-1) \left(\frac{\dot{\epsilon} t}{2} - \frac{n(n+1)}{84} \frac{\Lambda_0^2}{Ca_0} \left(e^{\frac{7}{2}\dot{\epsilon}_0 t} - 1 \right) \right)\right] \quad (4.34)$$

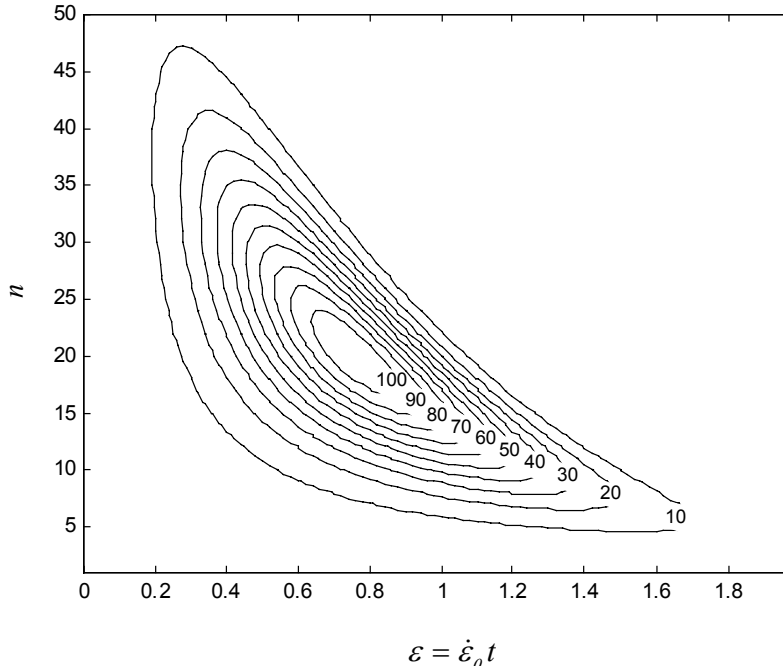


Figure 4.14 Theoretical prediction of the amplitude of the perturbation, f , (Equation 4.34) as a function of strain and mode number, n , for $Ca_0/\Lambda_0^2 = 500$. As the strain increases, the radial pressure gradient decreases, so the perturbations first grow to a maximum and then decay. The mode number which corresponds to the maximum amplitude is $n_{\max}=20$.

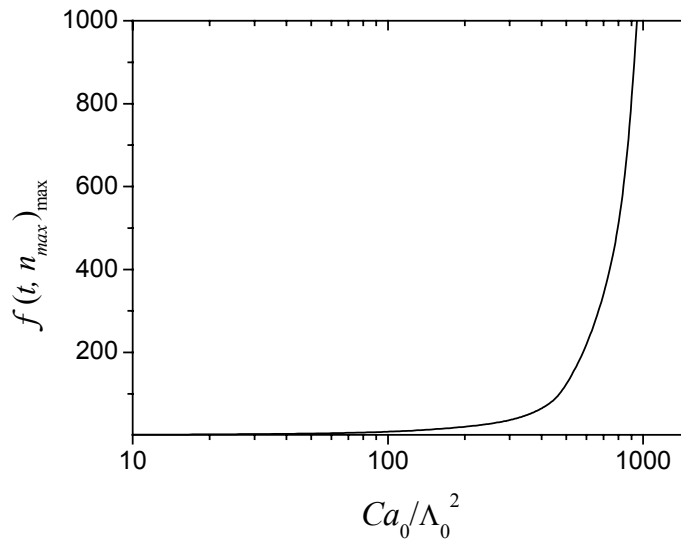


Figure 4.15 Maximum amplitude of the perturbation as a function of the initial value of the ratio Ca/Λ_2 .

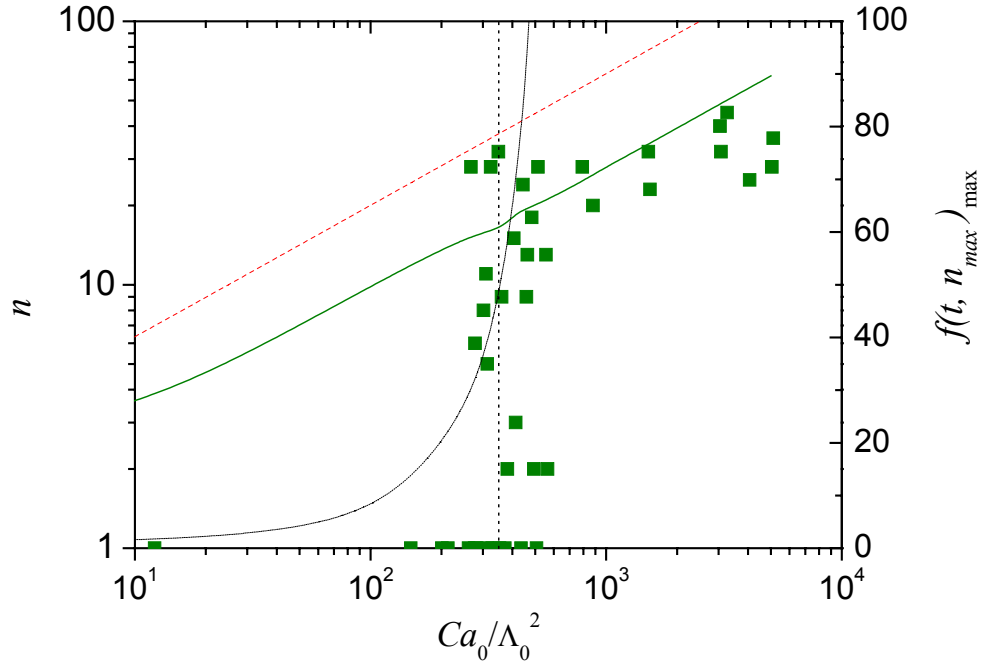


Figure 4.16 Number of fingers, n , observed with styrene oil (Newtonian liquid) versus the initial value of Ca/Λ^2 . Dashed line: Paterson relation (Equation 4.23) for n , directly adapted to a squeeze flow. Solid line: number of fingers corresponding to the perturbation mode with the larger amplitude in the relation (Equation 4.34). The dotted curve corresponds to the instability amplitude, $f(t)$, for n giving the maximum amplitude (see Figure 4.14). Note that the instability is observed experimentally at $Ca_0/\Lambda_0^2 > 350$, when the growth rate begins to increase rapidly ($Ca_0/\Lambda_0^2 = 350$ is denoted by the dotted vertical line).

4.2.3 Results and Discussion

It is observed that when the Saffman-Taylor instability occurs, the fingers grow and then decay as the stretch continues. This effect can be explained by the time-decreasing pressure gradient predicted by the lubrication theory, and can also be inferred from Figure 4.14, in which the growth rate, $f(t)$, steadily decreases after reaching a maximum. The contours in Figure 4.17 were generated using the linear stability analysis described in the last section. These contours represent fluid free surface at various times during a stretching experiment. This simulation is a good representation of the experimentally observed instability, i.e., the perturbations first grow, and then damp out at larger strains so that a fluid filament of circular cross section may form.

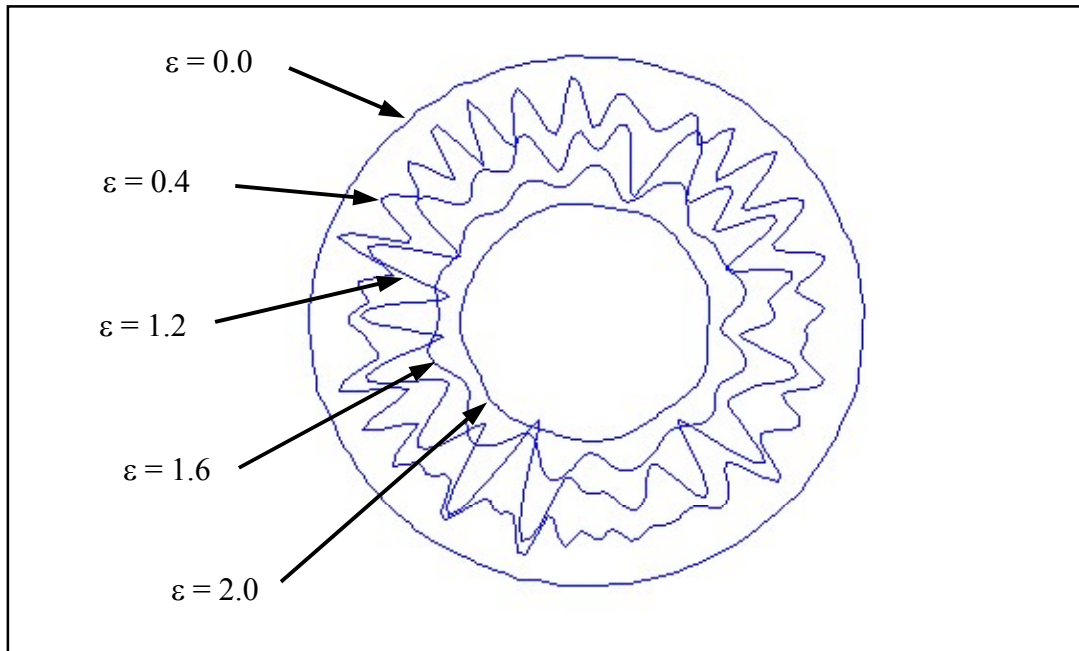


Figure 4.17 Simulation of 3-D Saffman-Taylor instability shape as a function of strain. Note that although the linear perturbation analysis is not expected to be relevant at large strains, the experiment does qualitatively mimic experimental observations, i.e., the finger amplitude often reaches a maximum before the interface begins to re-stabilize as the pressure gradient diminishes.

The Saffman-Taylor fingering instability can also occur in the viscoelastic test fluids. Although the appearance of the fingering instability in these fluids is virtually indistinguishable from the instability in the Newtonian liquid, the conditions for onset are quite different. In Figure 4.18, in which the initial capillary number is plotted against the initial aspect ratio, the stability curve as predicted by the theory adapted Paterson is shown as a solid line of slope 2. As mentioned earlier, the experimental determinations of onset of the viscous fingering instability coincide remarkably well with this prediction. However, at low aspect ratios, the Saffman-Taylor fingering instability in the Boger fluids occurs at appreciably lower strain rates than for the Newtonian liquid. Interestingly, at aspect ratios greater than $\Lambda_0 \approx 0.2$, the onset of the instability in the non-Newtonian liquids occurs at greater capillary numbers than for the Newtonian liquid. This phenomenon can only be explained by flow-induced elasticity, but due to the complex nature of the flow, a full explanation of this behavior is not possible.

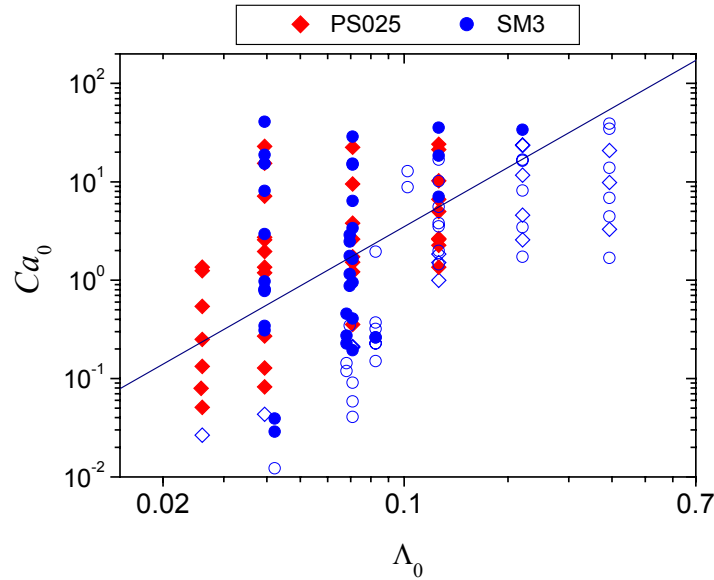


Figure 4.18 Experimental determination of the onset of the viscous fingering with viscoelastic Boger fluids. For each experiment, the capillary number is plotted versus the aspect ratio. Full symbols are used when fingers are observed. The solid line corresponds to the onset of the instability for a Newtonian liquid (styrene oil).

If the Saffman-Taylor instability does occur in the viscoelastic liquids and the Deborah number is large enough, it may be followed by the elastic fingering instability. However, in this case, the elastic fingers no longer grow from a circular column, but from the some shape left by the viscous fingering instability. As seen in Figure 4.19, this can lead to a more intricate pattern, in which small elastic fingers grow at regularly spaced intervals on either side of the primary fingers created by the Saffman-Taylor instability. These patterns have been termed ‘fishbones’ by the author for obvious reasons. Figure 4.20 contains a series of nine images from a stretch in which the fishbones appear. For this experiment the larger, 10mm diameter, endplates were used, but the stretch used the same fluid (SM3) and nearly the same stretch rate as the experiment shown in Figure 4.19 with the 5mm endplates. If there is any noticeable difference in the appearance of the instability, it is that the larger cube provides better optical resolution. As mentioned in the discussion of the elastic instability in Section 4.1, a theoretical explanation of these secondary elastic fingers and the bifurcation that occurs during the fishbone instability is not yet available.

It should be noted that when the elastic instability occurs after the Saffman-Taylor instability, there are two distinguishable morphologies. The first occurs when the elastic fingers grow directly from the fluid fingers left by the viscous fingering instability. In this case the fibrils

are very dense and span nearly the entire radius of the endplate. The second possibility occurs when the Saffman-Taylor instability decays allowing a fluid filament with a roughly circular cross-section to form. The elastic fingers then grow from this rough fluid filament in nearly the same manner as the purely elastic fingering instability.

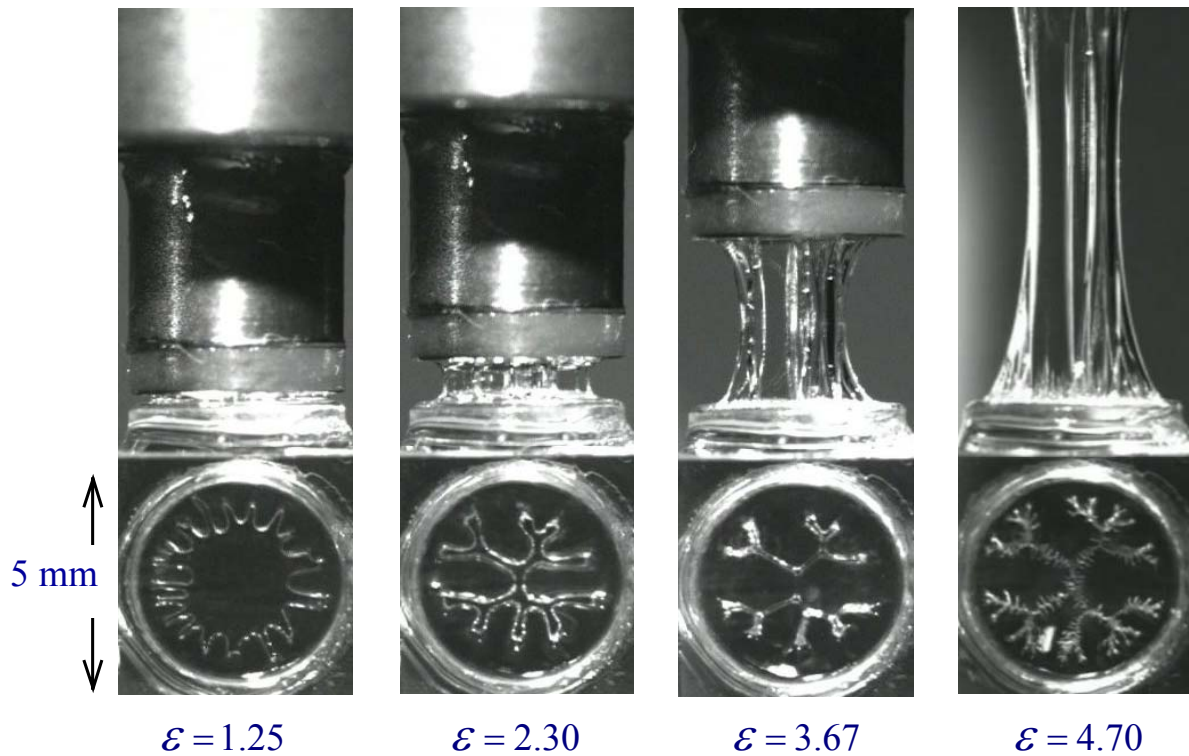


Figure 4.19 A series of 4 images showing the Saffman-Taylor instability followed by the elastic fingering instability that occurs at a larger strain ($\varepsilon_c > 3.7$). This experiment was done using the SM3 fluid at $De=43$ and $\Lambda_0=0.04$.

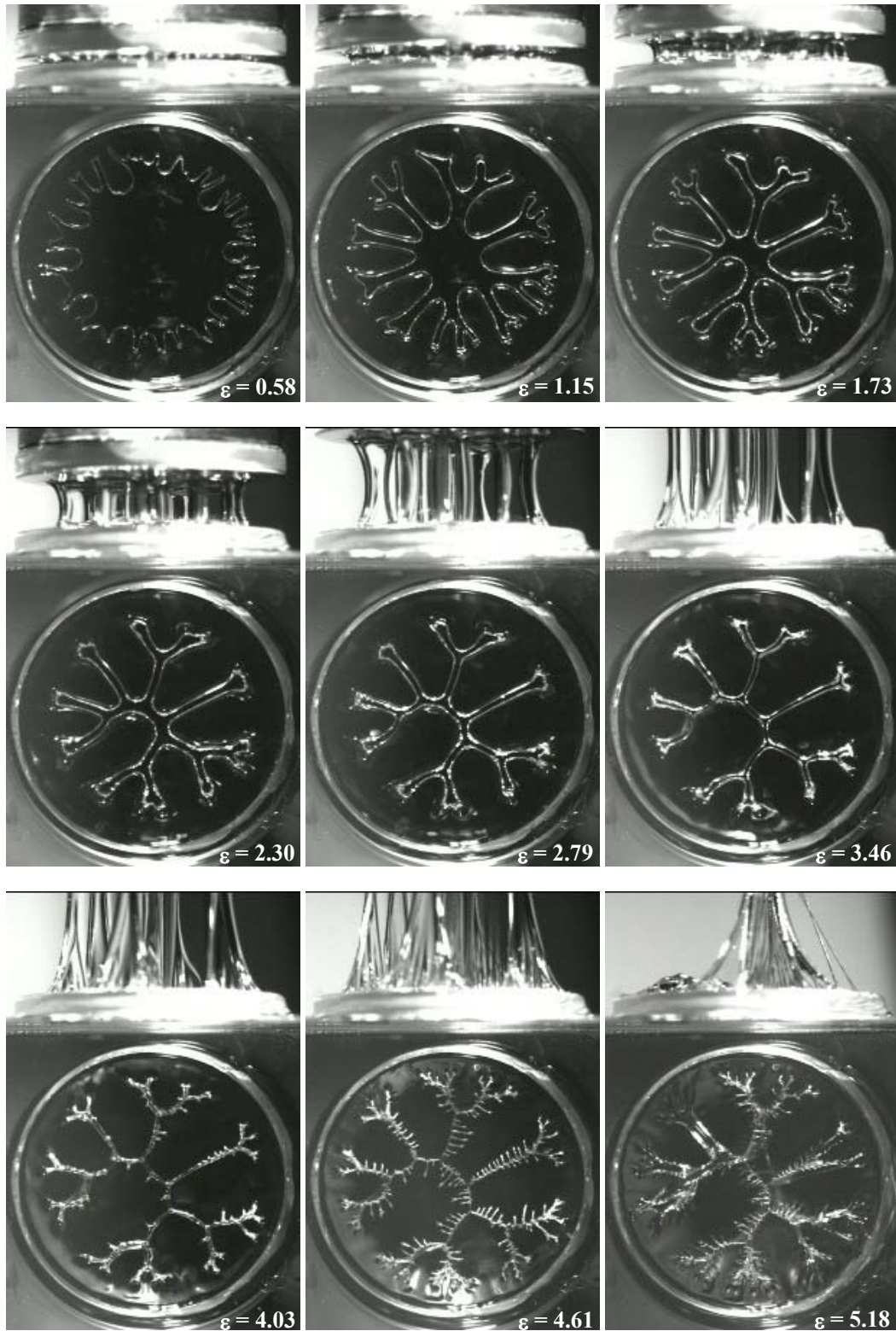


Figure 4.20 Formation of ‘fishbones’ in the elastic instability. This experiment uses the larger 10mm diameter endplates with all other parameters being nearly the same as the experiment shown in Figure 4.19 (SM3 fluid, $\Lambda_0 = 0.04$, $\dot{\epsilon} = 0.27\text{s}^{-1}$, $De=39$, $Ca = 2.8$).

4.3 Cavitation

When the initial aspect ratio is lowered, and when the rate of plate separation is increased, the pressure within the liquid decreases as predicted by lubrication theory, and cavitation may occur. Figure 4.21 contains a still image from a stretching experiment in which two cavitation bubbles form.

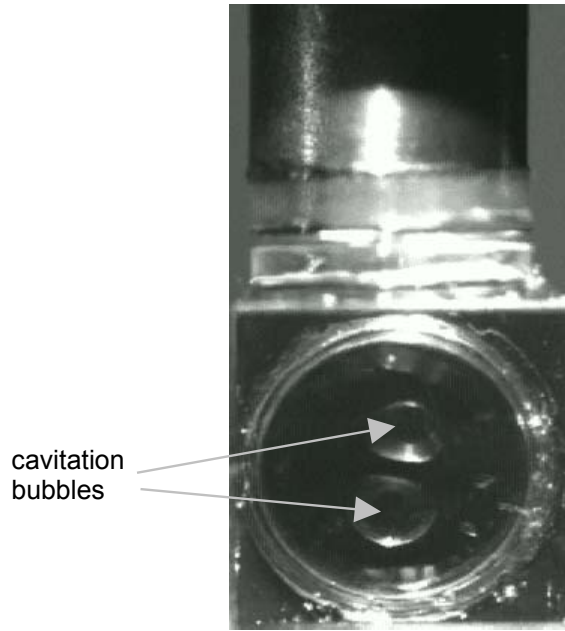


Figure 4.21 Image showing cavitation in the SM3 fluid. Note that the bubbles have appeared before the endplates have separated appreciably. The experimental parameters are: $\dot{\epsilon} = 7.7\text{s}^{-1}$, $\Lambda_0 = 0.04$, $De = 1050$, $Ca = 37$.

4.3.1 Results and Discussion

It has long been realized that cavitation should occur in a liquid below some critical pressure [29], [31]. It was explained earlier in this chapter that the pressure distribution within the fluid sample at the start of an experiment can be found by the lubrication approximation. If Equation 4.26 is written as a function of the initial capillary number and initial aspect ratio, the initial pressure at the center of the endplate is

$$P \Big|_{\substack{r=0 \\ t=0^+}} = P_0 - \frac{6\sigma}{R_0} \left(\frac{Ca_0}{\Lambda_0^2} \right). \quad (4.35)$$

Thus, for a given geometry, the critical pressure is a function of the same dimensionless parameter, Ca_0/Λ_0^2 , that determines the onset of the Saffman-Taylor instability. Figure 4.22 contains experimental data from stretching experiments using all of the test fluids. In this plot, experiments in which cavitation occurred are shown with filled symbols, and experiments with no cavitation are shown with unfilled symbols. From the data in Figure 4.22, it was found using Equation 4.35 that cavitation occurred for $Ca_0/\Lambda_0^2 \geq 4300$. This corresponds to a critical pressure of $P_{crit} \approx -5 \times 10^4 \text{ N/m}^2$. There appeared to be no difference in the critical pressure required for the onset of cavitation for the three test fluids, which was expected, given the similarity in viscosities of the three fluids. However, it should be noted that the cavitation bubbles seemed to grow faster in the Newtonian liquid than in the viscoelastic liquids. A possible explanation is that the cavitation itself induces an elastic response in the vicinity of the bubble, acting to damp further bubble growth. Unfortunately, it was not possible to further explore this phenomenon with standard video because the cavitation always occurred very quickly (within 1.3 frames), resulting in poor temporal resolution.

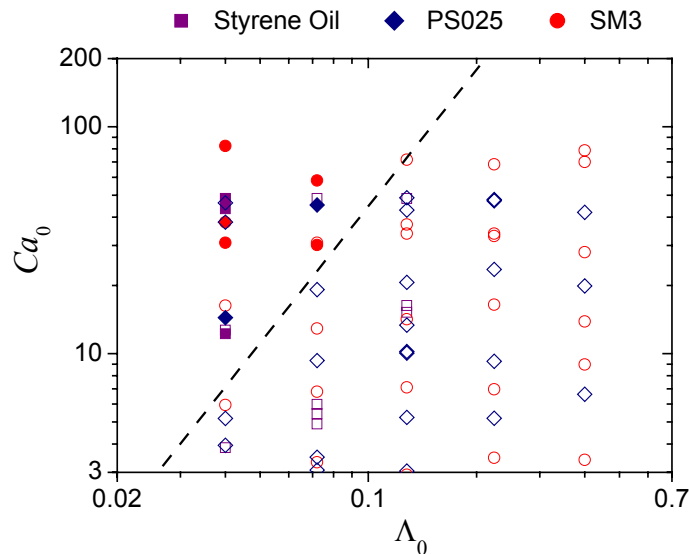


Figure 4.22 Plot of Ca_0 vs. Λ_0 showing validity of critical Ca_0/Λ_0^2 for cavitation. The filled markers represent experiments in which cavitation was observed. The dashed line corresponds to a pressure of -0.5 bar ($-5 \times 10^4 \text{ N/m}^2$) the center of the endplate as calculated from lubrication theory.

Chapter 5 Conclusions and Future Work

5.1 Conclusions

A filament stretching rheometer was modified in order to perform stretching experiments on highly confined liquids in order to investigate various free surface instabilities that can occur. The resulting experiment, which was described in Chapter 2, is very similar to the probe-tack test that is used to test pressure-sensitive adhesives (PSAs). Three test fluids were used; a Newtonian fluid and two model viscoelastic liquids, all of which were described in Chapter 3. The results of the experiments were presented in Chapter 4, which was divided into three sections, corresponding to the three instability mechanisms observed in the experiments.

The first section of Chapter 4 described the elastic fingering instability, which occurs only in the viscoelastic test fluids. The purely elastic fingering instability results when the fluid strain hardens and most of the fluid remaining at the endplates has been drawn into an almost axially uniform elastic fluid column. As this instability progresses, ‘fingers’ of fluid grow radially outward from the column. At larger strains, the tips of the fingers can bifurcate and these new fingers can bifurcate again, resulting in fractal-like geometric patterns. Previous publications have shown that that instability is influenced by surface tension, which has been shown to play a role in setting the number of fingers initially observed [75].

An earlier theory relating surface tension to the critical strain at the onset of the elastic fingering instability [60] was slightly modified in order to better represent the physical problem. This was done by using the approximate midfilament radius rather than the initial endplate radius (from volume conservation) in the estimation of the contribution of surface tension. With this modification the critical strain observed for the current experiments was very close to the prediction of the theory. Nevertheless, it seems that the critical strain also occurs at the point in the stretch when almost all of the fluid has been drawn into the column, and empirical predictions of this strain can be achieved by relating the measured midfilament radius to the radius based on the ideal deformation of a cylinder.

The second section of Chapter 4 describes an instability closely related to the well-known Saffman-Taylor instability that occurs in planar Hele-Shaw cells for Newtonian as well as non-Newtonian fluids. If a less viscous fluid drives a more viscous fluid in a pressure driven flow, the interface between the fluids becomes unstable to perturbations, and fingers of the less viscous

fluid penetrate into the more viscous one. A radial variation of this instability is also possible in a Hele-Shaw cell and independent studies of the Saffman-Taylor instability in this geometry were undertaken by both Paterson [45] and Bataille [79]. The Saffman-Taylor instability is seen in the current experiments when the initial aspect ratio is sufficiently small, and occurs at the start of an experiment when radially converging fingers of air penetrate into the viscous liquid between the endplates. When an experiment begins and the endplates begin to separate, a radial pressure gradient is induced mechanically according to lubrication theory for a reverse squeeze flow. From the theory of Paterson, a stability criterion for the onset of the Saffman-Taylor instability was successfully adapted to the current experiment, and the occurrence or non-occurrence of the instability can now be predicted for Newtonian liquids, given the initial experiment conditions. In viscoelastic liquids, combinations of the elastic instability and the Saffman-Taylor instability can also result. When this occurs, the final shape of the elastic instability can be very complex and elastic fingers grow from remnants of the viscous fingering instability, creating dense fibrillar patterns.

Finally, cavitation can occur when the pressure in the fluid is reduced beyond a critical value, i.e., when the separation rate is large enough and the aspect ratio, or degree of confinement, is small enough. This experimental result is in agreement with classical results of Kaelble [31]. The experimental data indicates that cavitation occurs when the ratio Ca_0/Λ_0^2 reaches a critical value. The corresponding pressure can be found by expressing the lubrication approximation for the initial pressure at the center of the endplates as a function of this number, or

$$P \Big|_{\substack{r=0 \\ t=0^+}} = P_0 - \frac{6\sigma}{R_0} \left(\frac{Ca_0}{\Lambda_0^2} \right) \quad (5.1)$$

From Equation 5.1 and the data in Figure 5.1, the critical pressure required for cavitation in the styrene-based fluids is approximately $P_{crit} = -5 \times 10^4 \text{ N/m}^2$ (-0.5 bar).

5.1.1 *Stability Diagram*

A stability diagram summarizing the results of the current experiments for the non-Newtonian test fluids was developed (see Figure 5.1). This diagram may be used as a guide to predict which instability, if any, may occur in a stretching experiment given the initial experimental parameters. The abscissa represents the importance of elastic effects as

characterized by the Deborah number (De), whilst the ordinate axis characterizes the importance of viscous and capillary forces that drive the Saffman-Taylor instability. The different regimes of this stability diagram are summarized in the following paragraphs.

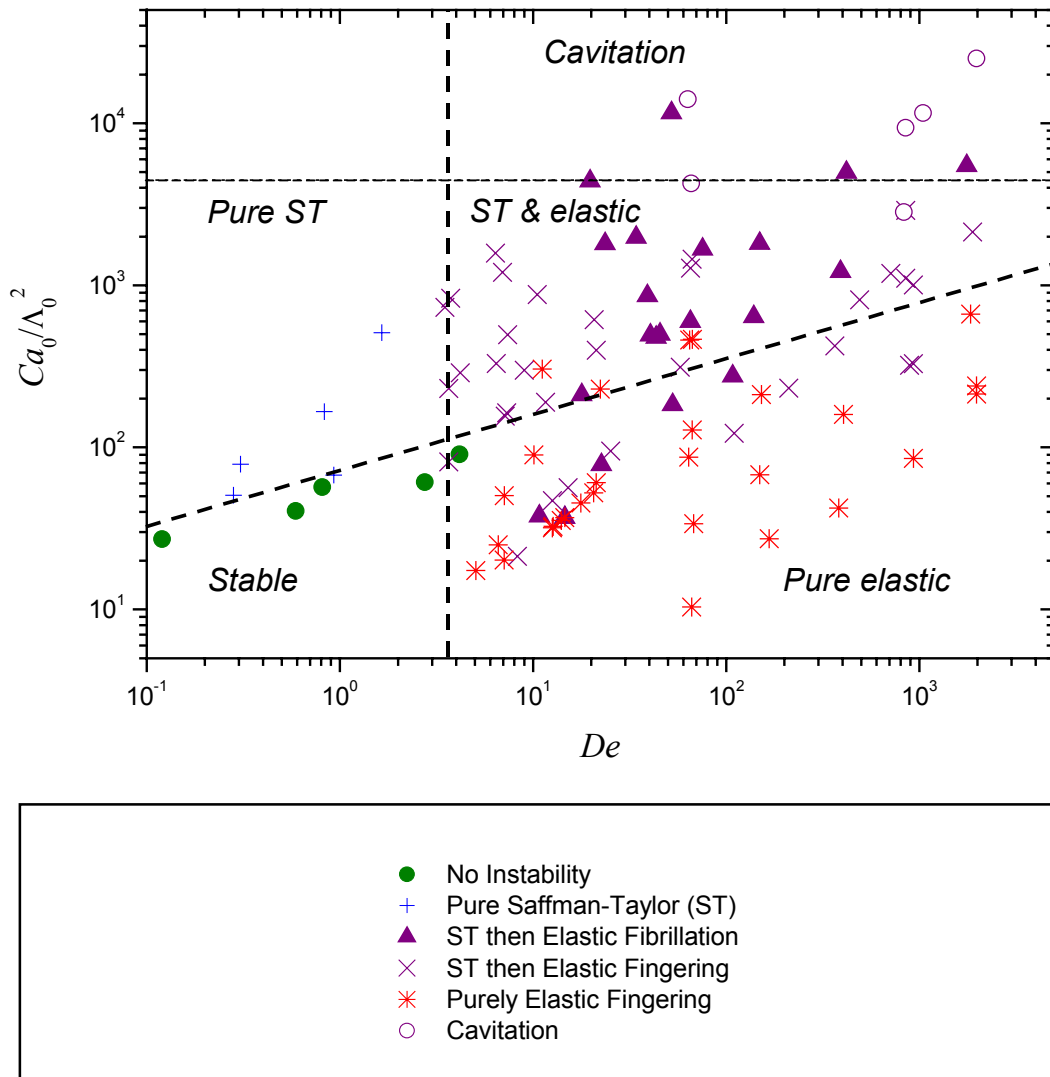


Figure 5.1 Stability diagram for the different modes of instabilities during the filament stretching of highly elastic liquids.

As the diagram indicates, there is a region for small Ca_0/Λ_0^2 and small De for which no instability occurs. In this region, a stable fluid filament develops, leaving an evenly distributed layer of fluid at the endplate (see Figure 5.2).

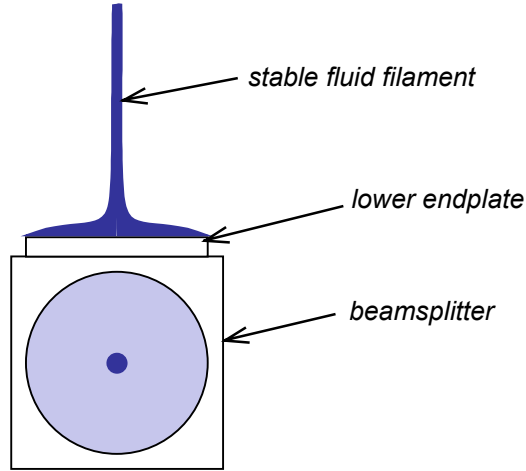


Figure 5.2 Sketch of lower endplate and fluid filament and in an experiment in which no instability develops.

The elastic fingering instability is observed to occur at Deborah numbers above a critical value of $De = 4$, although viscoelastic liquids typically begin to strain harden at $De > 1/2$ [80]. The fact that the elastic instability does not occur at lower Deborah numbers may be related to the dimensionless parameter written

$$\phi = \frac{\lambda\sigma}{\eta_0 R_0} \equiv \frac{De}{Ca}, \quad (5.2)$$

where λ is the fluid relaxation time, σ is the surface tension, η_0 is the zero shear rate viscosity, and R_0 is the endplate radius [60], [75]. This dimensionless number depends only on fluid properties and on the stretching geometry, and is a ratio of surface tension-induced stress, σ/R_0 , to the elastic modulus of the fluid, $G = \eta_0/\lambda$ (for the elastic polymer solutions used in this study, $1 \leq \phi \leq 20$). However, it should be noted that the non-occurrence of the elastic instability of at $1/2 < De < 4$ may simply be because the velocity and position limits of the filament stretching rheometer are reached before the fluid can sufficiently strain harden (see Chapter 2). Figure 5.3 contains a sketch of the elastic fingering instability as it occurs in this region.

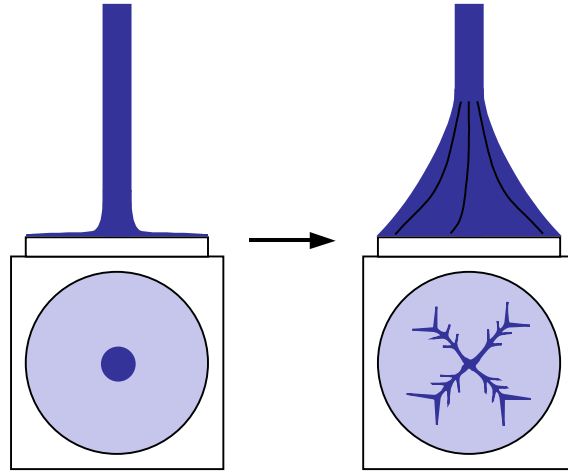


Figure 5.3 Sketch of the purely elastic fingering instability. Early in the experiment, a stable filament forms. At a larger strain, fingers begin to grow outward from the base of the column. These fingers may bifurcate and secondary fingers may grow from the initial fingers.

At values of $Ca_0 / \Lambda_0^2 > 350$, a sufficiently large radial pressure gradient is created to induce the Saffman-Taylor fingering instability in Newtonian liquids. This result is predicted by the theory adapted from Paterson and validated by the experiments using styrene oil. For the viscoelastic test fluids the initial conditions are not as clear. As Figure 5.1 indicates, the critical value of Ca_0 / Λ_0^2 appears to be a function of the Deborah number, suggesting an influence of fluid elasticity on the instability. Consequently, a region is mapped from the experimental results, as shown by the dashed line of positive slope. Above this dashed line, the Saffman-Taylor instability can take on multiple forms. If the Deborah number is below the critical value of $De = 4$, the instability consists only of the Saffman-Taylor instability, followed by no elastic instability. In this case, a fluid column still forms and the decreasing radial pressure gradient can even allow the fluid at the base of the column to regain a circular shape before the experiment ends. If however, the Deborah number is large enough, then the elastic instability will occur after the initial Saffman-Taylor instability. In this case, a single fluid filament can still form, as for experiments marked an ‘×’ on Figure 5.1 (and shown in Figure 5.4), or, the Saffman-Taylor instability can lead directly to fibrillation and the elastic ‘fishbone’ patterns with forming a filament. When the former occurs, it is more like the familiar elastic fingering instability, in which fingers grow radially outward. When the Saffman-Taylor instability leads directly to

fibrillation, elastic fingers grow on a much smaller length scale from the fluid patterns formed by the viscous instability as shown by the sketch in Figure 5.5.

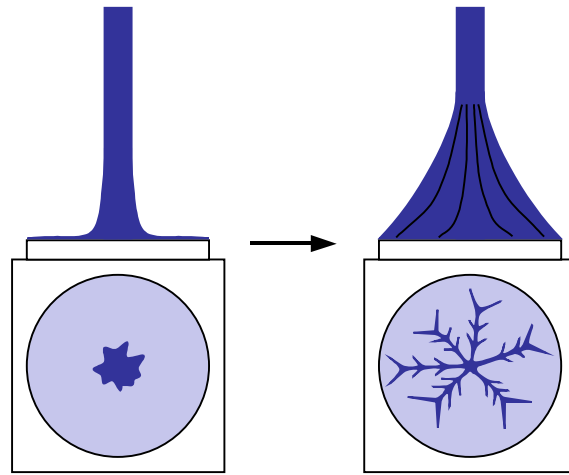


Figure 5.4 It is possible for the Saffman-Taylor instability to occur, then re-stabilize (because of the decreasing pressure gradient) and form a roughly circular fluid column. This phenomenon can occur before the elastic instability. In this case, the elastic fingers grow radially outward from the roughly circular filament.

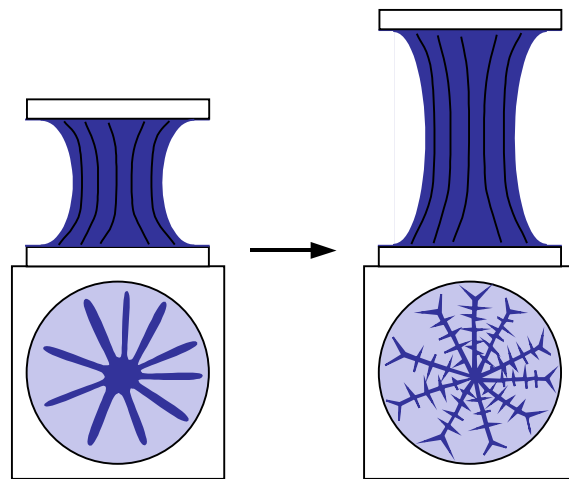


Figure 5.5 When the viscous instability precedes the elastic instability and the Saffman-Taylor fingers do not decay significantly before the onset of the elastic fingering instability, elastic fingers can grow directly from the remaining traces of the viscous fingers, resulting in complex geometric patterns and dense fibrils. These patterns have been termed ‘fishbones’ by the author because of their appearance.

It is well known that cavitation should occur in a viscoelastic liquid at a critical low pressure [31], and this phenomenon is observed in the current experiments as well. It was observed that cavitation in the viscoelastic test fluids occurred at the critical value of $Ca_0/\Lambda_0^2 \approx 4300$ on the ordinate axis of Figure 5.1. From lubrication theory, this value corresponds to a pressure of $P_{crit} \approx -5 \times 10^4 \text{ N/m}^2$. When cavitation occurs, it can be followed by the elastic fingering instability and fibrillation. Just as the Saffman-Taylor instability affects fibril development when that instability leads directly to fibrillation, the shape of the fishbone patterns and the density of the fibrils are influenced by the residual shapes left by the cavitation bubbles (see Figure 5.6).

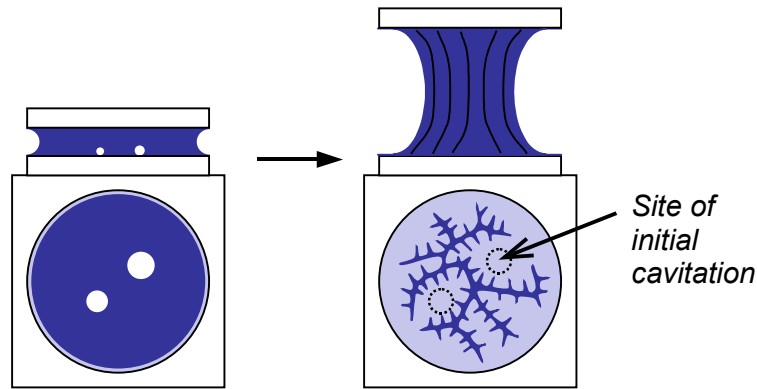


Figure 5.6 When the pressure within the fluid is low enough cavitation can occur. In the viscoelastic fluids, cavitation can be followed by the elastic instability. When this occurs, the final shape of the elastic instability and the morphology of the fibrils is significantly altered because the elastic fingers (and therefore fibrils) grow around the sites where the cavitation bubbles occurred.

5.1.2 Adhesive properties

Because of the close similarity to the probe-tack test, which is used to test pressure sensitive adhesives, it is natural to consider the tensile force and work of adhesion required to debond the endplates. As mentioned in Chapter 1, the viscoelastic test fluids used for this study are not true pressure sensitive adhesives because a residue remains on the endplates after *cohesive* failure [16]. Pressure-sensitive adhesives should debond adhesively and leave no residue. Nevertheless, the test fluids used for the experiments in this thesis do have many similarities to

pressure sensitive adhesives. Fingering instabilities (both elastic and viscous) have been observed in testing of PSAs [56], [58], [57], [59], [54]. In addition fibrillation, which is observed in the current experiments, is of interest because of its effect on the work of adhesion, or the energy per unit area required to normally debond two surfaces [38], [37]. Finally, the force versus strain curves for the strain hardening Boger fluids used for this study are very similar to those for PSAs [21].

Figures 5.7 and 5.8 contain measured force data as a function of Hencky strain for several experiments in which only the purely elastic instability occurred. The first peak in these curves results from the viscous, reverse squeeze flow, which was explained in Chapter 2 using Reynolds lubrication theory. The second peak in the curves, which occurs at greater strains, is due to strain hardening. The data in Figure 5.7 is for three stretching experiments using the SM3 fluid at various initial aspect ratios, but with a nearly constant Deborah number. As expected, the initial viscous force response of the fluid increases with decreasing endplate separation. Interestingly, despite the differing aspect ratios and sample volumes, the data for all three experiments nearly coincides for the later part of the stretch. The maximum force recorded for all three experiments is nearly the same. This is because the Deborah number is so large that in each of the three experiments the fluid is deformed sufficiently that all memory of initial conditions is eradicated.

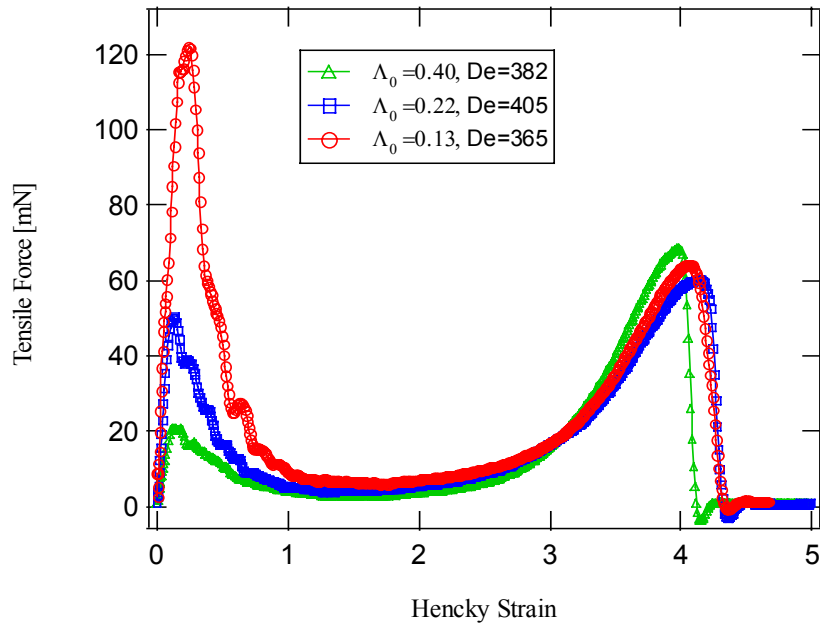


Figure 5.7 Force data for three experiments in which the aspect ratio was varied but the Deborah number remained nearly constant at $De \approx 385$.

The data in Figure 5.8 contains the force versus strain data for three stretching experiments of different aspect ratio, but of a nearly constant Deborah number that is significantly lower than that of the experiments in Figure 5.7. Again, the magnitude of the initial force peak increases with decreasing aspect ratio. By comparing Figures 5.7 and 5.8 it can be seen that the magnitudes of the viscous force responses are lower for the experiments at a lower separation rate for the same aspect ratio, which is again in agreement with lubrication theory. The magnitudes of the second peak (elastic response) are also lower for the experiments of lower Deborah number. It can be concluded from these results that measurement of transient extensional viscosity in the filament stretching rheometer are not so sensitive to changes in aspect ratio.

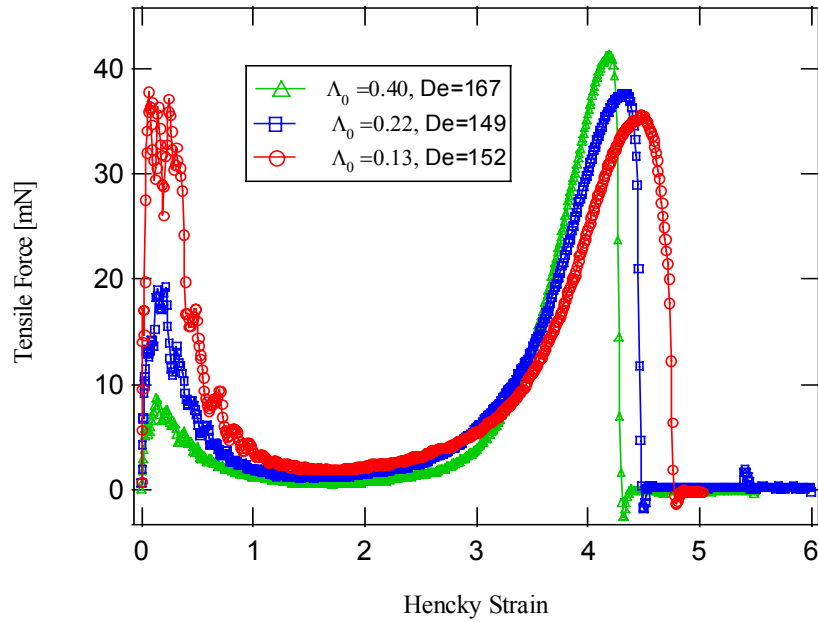


Figure 5.8 Force data for three experiments in which the aspect ratio was varied but the Deborah number remained nearly constant at $De \approx 155$.

By integrating the force curves shown in Figures 5.7 and 5.8 with respect to distance, and then dividing by the endplate area, the work of adhesion (expressed in J/m^2) can be found as

$$w_a = \frac{1}{A} \int F(z) dz, \quad (5.3)$$

where A is the endplate area, and $F(z)$ is the axial force as a function of position, which can be found from the Hencky strain. As seen in Figure 5.9, for the nearly constant Deborah number the

total work of adhesion increases significantly as the aspect ratio, or sample volume size, is increased. This trend is also observed for the three experiments at the lower Deborah number in Figure 5.10. By comparing Figures 5.9 and 5.10, it is seen that the total work of adhesion also increases with increasing strain rate, or Deborah number. An exception to this observation is that the total work of adhesion is nearly equivalent at both Deborah numbers for the lowest aspect ratio. It should be noted that the initial viscous response is insignificant role compared to the elastic response in the work of adhesion.

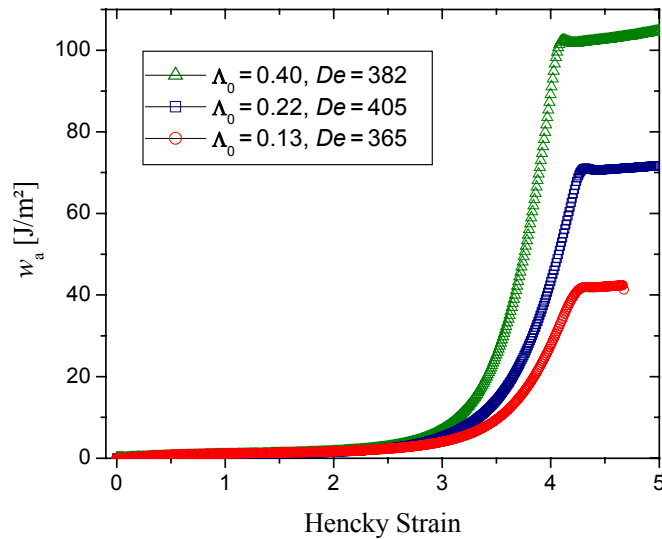


Figure 5.9 Work of adhesion as a function of strain for the experiments shown in Figure 5.7, in which the aspect ratio was varied but the Deborah number remained nearly constant at $De \approx 385$

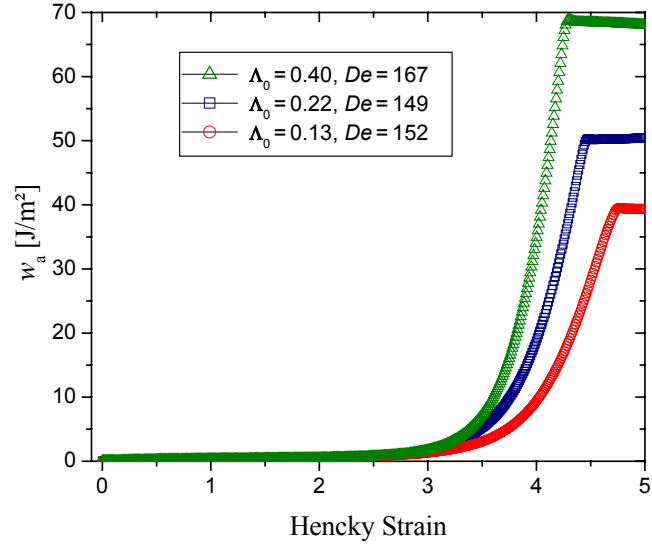


Figure 5.10 Work of adhesion as a function of strain for the experiments shown in Figure 5.8, in which the aspect ratio was varied but the Deborah number remained nearly constant at $De \approx 155$.

5.2 Future Work

There are many avenues that could be taken in the continuation of this research. For example, because of the difficulties in aligning the endplates by the current mechanism, the smaller 5mm endplate assembly was used for the majority of the experiments in this thesis. A larger endplate, however, provides better visualization of the instabilities (see Figure 4.20). In the case of the elastic instability, better optical resolution could lead to a better understanding of the elastic fingering instability. This would be especially helpful in the case of the ‘fishbone’ instability observed when the Saffman-Taylor precedes the elastic instability, for which little is known. With the current alignment mechanism, the angular alignment resolution is fixed, albeit unknown, and as the endplate radius increases, sine errors increase proportionally. A self-aligning mechanism that takes advantage of the flat surfaces of the endplates can be envisioned, i.e., the endplates could be brought together, and then fastened in some appropriate manner.

In addition to better optical resolution, larger endplates allow for even lower aspect ratios to be examined for the same initial endplate separation. Lower aspect ratios could enhance the study of cavitation and the effect of cavitation on fibrillation and adhesive bond strength, a topic for which there is currently much research interest [38], [59], [21], [54], [22], [56]. Lower

aspect ratios are beneficial for the study of cavitation, because a lower strain rate is required to generate the requisite low pressure in the fluid, and it is expected that the cavitation itself would occur on a proportionally longer timescale. This is because the pressure gradient as predicted by lubrication theory should not decay so fast in time. In the current experiments, cavitation happened so fast (within a couple of video frames) that it was impossible to investigate the phenomena in detail using standard video at 30 frames per second. It should be noted that a high-speed camera was obtained on loan from the Edgerton Laboratory at MIT in order to better capture the occurrence of cavitation, and some experiments were recorded at 1000 frames per second. However, it was necessary to increase the intensity of the lighting, which in turn caused reflections on the beamsplitter that obscured the view of the instability, and the high-speed camera proved to be of no great benefit. Admittedly, not a lot of time was spent on this endeavor and it may be worthwhile in the future to optimize the lighting conditions for use with high-speed video.

A simple modification to the experiment that may also provide valuable insight is the use of non-circular endplates. In the course of the current experiments, a rectangular endplate was fashioned from plexiglas and used as the lower endplate. The results were not uninteresting, as can be seen from Figure 5.11.

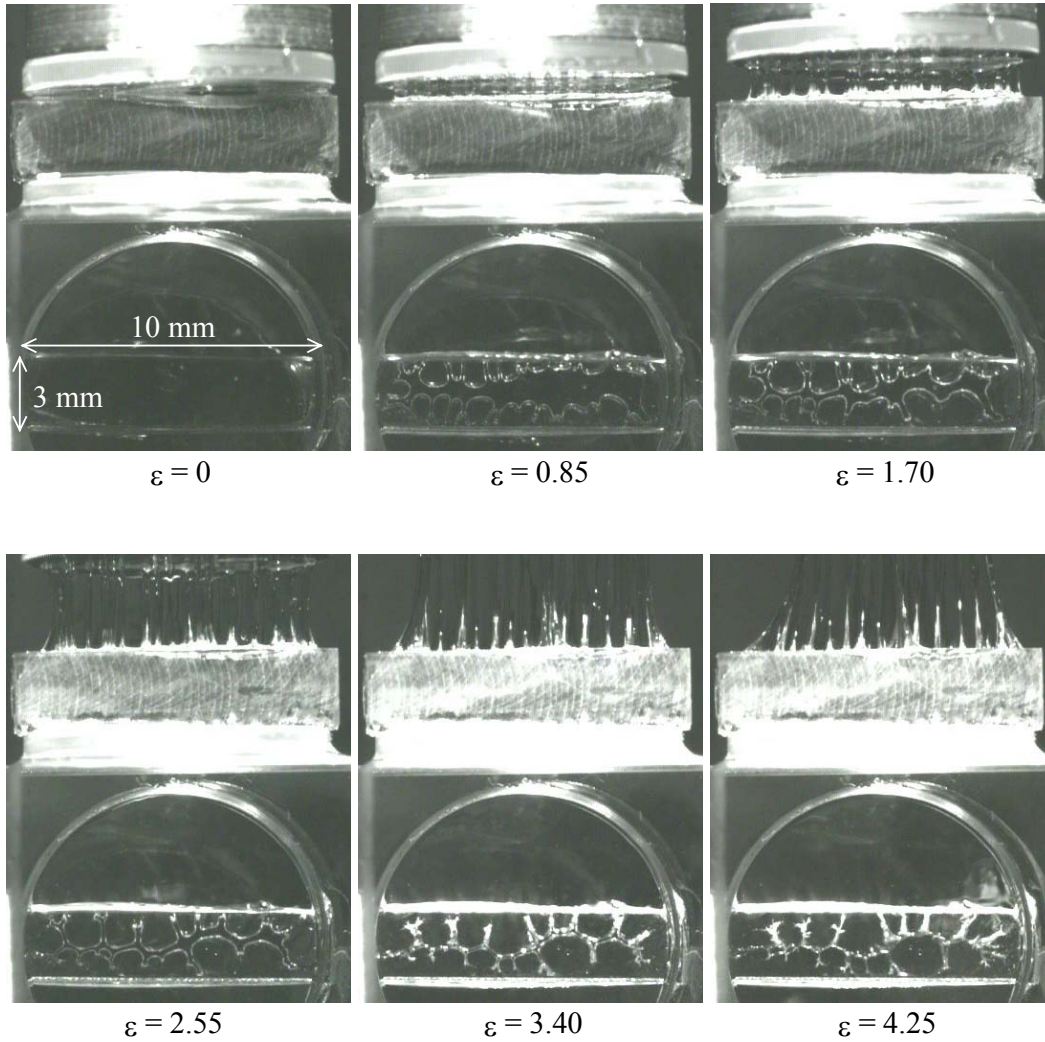


Figure 5.11 Stretching the SM3 liquid with a rectangular endplate (a 3mm x 10mm piece of plexiglas fixed to the prism by capillarity with a thin layer of liquid). For this experiment, an initial gap of $L_0=0.15\text{mm}$ was used. An aspect ratio can be defined using the ratio of the initial gap to the width of the rectangle (3mm), so that $\Lambda_0=0.05$.

5.3 Summary

This study has resulted in the development of a stability diagram and the mapping of a stability region, which can be used to determine the useful limits of initial parameters in filament stretching rheometry. Two types of fingering instabilities were clearly distinguished. The three dimensional radial Saffman-Taylor instability was described by adapting a previous theory

developed for the two dimensional case. It was found that the new theory accurately represented the current experimental findings. A previous theory predicting the onset of the elastic fingering instability was slightly modified to better describe the flow, thus resulting in an accurate prediction of the critical strain for the onset of the elastic fingering instability in the current experiments.

It was found that the viscoelastic liquids used as test fluids are not true pressure-sensitive adhesives because these fluids fail cohesively in a probe-tack test, leaving a residue on the endplates. Nevertheless, the fluids exhibit behavior that is similar in many ways to true PSAs, Such behavior includes fingering instabilities, cavitation, and fibrillation. In addition, it was found that the force profiles for the current experiments were very similar to those observed in similar tests of PSAs. Finally, from the force data, it was ascertained that results of extensional viscosity measurements in the filament stretching rheometer should not be very sensitive to changes in the initial aspect ratio, but that the total work of adhesion is sensitive to such changes.

Bibliography

1. Boger, D.V., *A Highly Elastic Constant-Viscosity Fluid*. J. Non-Newtonian Fluid Mech., 1977/78. **3**: p. 87-91.
2. Anna, S.L., *Filament Stretching of Model Elastic Liquids*, in *Division of Engineering and Applied Sciences*. 2000, Harvard University: Cambridge.
3. Flory, P., *Principles of Polymer Chemistry*. 1953, Ithaca: Cornell University Press.
4. Reiner, M., *The Deborah Number*. Phys. Today, 1964. **17**: p. 62.
5. Bird, R.B., R.C. Armstrong, and O. Hassager, *Dynamics of Polymeric Liquids*. 2 ed. Vol. I: Fluid Mechanics. 1987, New York: Wiley.
6. Trouton, F.T., *On the coefficient of viscous traction and its relation to that of viscosity*. Proc. Roy. Soc. London, 1906. **77**: p. 426-440.
7. Bird, R.B., R.C. Armstrong, and O. Hassager, *Dynamics of Polymeric Liquids*. 2 ed. Vol. II: Kinetic Theory. 1987, New York: Wiley.
8. Sridhar, T., V. Tirtaatmadja, D.A. Nguyen, and R.K. Gupta, *An Overview of the Project MI*. J. Non-Newtonian Fluid Mech., 1990. **35**: p. 86-92.
9. James, D.F. and K. Walters, *A Critical Appraisal of Available Methods for the Measurement of Extensional Properties of Mobile Systems*, in *Techniques of Rheological Measurement*, A.A. Collyer, Editor. 1994, Elsevier Science: New York.
10. Sridhar, T., V. Tirtaatmadja, D.A. Nguyen, and R.K. Gupta, *Measurement of Extensional Viscosity of Polymer Solutions*. J. Non-Newtonian Fluid Mech., 1991b. **40**: p. 271-280.
11. Tirtaatmadja, V. and T. Sridhar, *A Filament Stretching Device for Measurement of Extensional Viscosity*. J. Rheology, 1993. **37**(6): p. 1081-1102.
12. Szabo, P., *Transient Filament Stretching Rheometer I: Force Balance Analysis*. Rheol. Acta, 1997. **36**: p. 277-284.
13. McKinley, G.H., *Science Requirements Document for The Extensional Rheology Experiment*. 1997: Harvard University.
14. Anna, S.L., G.H. McKinley, D.A. Nguyen, T. Sridhar, S.J. Muller, J. Huang, and D.F. James, *An Interlaboratory Comparison of Filament Stretching Rheometers*. J. Rheology, 2001. **45**(1): p. 83-114.

15. McKinley, G.H. and T. Sridhar, *Filament Stretching of Complex Fluids*. Annual Rev. of Fluid Mech., 2002. **34**.
16. *Glossary of Terms*. 2001, Pressure Sensitive Tape Council.
17. Dalquist, C.A., *Pressure-Sensitive Adhesives*, in *Treatise on Adhesion and Adhesives*, R.L. Patrick, Editor. 1969, Marcel Dekker: New York. p. 219-260.
18. Lakrout, H., C. Creton, D. Ahn, and K.R. Shull, *Influence of Molecular Features on the Tackiness of Acrylic Polymer Melts*. Macromolecules, 2001. **34**: p. 7448-7458.
19. Maugis, D. and M. Barquins, *Fracture mechanics and the adherence of viscoelastic bodies*. J. Phys. D: Appl. Phys., 1978. **11**: p. 1989-2023.
20. Gent, A.N., *Adhesion and strength of viscoelastic solids. Is there a relationship between adhesion and bulk properties?* Langmuir, 1996. **12**: p. 4492-4496.
21. Gay, C. and L. Leibler, *On Stickiness*. Phys. Today, 1999. **52**(11): p. 48-52.
22. Chiche, A., P. Pareige, and C. Creton, *Role of surface roughness in controlling adhesion of a soft adhesive on a hard surface*. C.R. Acad. Sci. Paris: Polymers at Interfaces, 2000. **1**(9): p. 1-8.
23. Creton, C., J. Hooker, and K.R. Shull, *Bulk and Interfacial Contributions to the Debonding Mechanisms of Soft Adhesives: Extension to Large Strains*. Langmuir, 2001. **17**: p. 4948-4954.
24. Piau, J., C. Verdier, and B. Lazhar, *Influence of rheology and surface properties in the adhesion of uncross-linked pressure sensitive adhesives*. Rheol. Acta, 1997. **36**: p. 446-461.
25. Zosel, A., *The effect of bond formation on the tack of polymers*. J. Adhesion Sci. Technol., 1997. **11**: p. 1447-1457.
26. Chikina, I. and C. Gay, *Cavitation in Adhesives*. Phys. Rev. Letters, 2000. **85**: p. 4546-4549.
27. McEwan, A.D. and G.I. Taylor, *The peeling of a flexible strip attached by a viscous adhesive*. J. Fluid Mech., 1966. **26**: p. 1-15.
28. Creton, C., *Materials Science of Pressure-Sensitive Adhesive*, in *Materials Science and Technology*, R. Cahn, P. Haasen, and E. Kramer, Editors. 1997, Weinheim VCH: New York. p. 707-741.

29. Gent, A.N. and P.B. Lindley, *Internal rupture of bonded rubber cylinders in tension*. Proc. Roy. Soc. London, A, 1958. **249**: p. 195.
30. Gent, A.N. and R.P. Petrich, *Adhesion of Viscoelastic Materials to Rigid Substrates*. Proc. Roy. Soc. London, A, 1969. **310**: p. 433-448.
31. Kaelble, D.H., *Cavitation in Viscoelastic Media*. Trans. Soc. Rheol., 1971. **15**: p. 275-296.
32. Kaelble, D.H., *Peel Adhesion: Micro-Fracture Mechanics of Interfacial Unbonding of Polymers*. Trans. Soc. Rheol., 1965. **9**: p. 135-163.
33. Brain, A.A., R.A. Chivers, and N.W. Granville. *The Influence of Adhesive Fibrillation on the Peeling of Pressure Sensitive Adhesive Coated Tapes*. in *Euradh '96: Adhesion '96*. 1996. Cambridge: Insitute of Materials; Societe Francaise du Vide; Dechema Institut.
34. Wetzel, F., *The Characterization of Pressure-Sensitive Adhesives*. ASTM Bulletin, 1957. **221**: p. 64-68.
35. Zosel, A., *Physical Properties and Adhesion Performance of Pressure Sensitive Adhesives*. Adhesives Age, 1989. **32**: p. 42-47.
36. Miller, J.C. and R.R. Myers, *A Photographic Study of Liquid Flow in a Roll Nip*. Trans. Soc. Rheol., 1958. **2**: p. 77-93.
37. Lakrout, H., P. Sergot, and C. Creton, *Direct Observation of Cavitation and Fibrillation in a Probe Tack Experiment on Model Acrylic Pressure-Sensitive-Adhesives*. J. Adhesion, 1999. **69**: p. 307-359.
38. Zosel, A., *The effect of fibrillation on the tack of pressure-sensitive adhesives*. Int. J. Adhesion & Adhesives, 1997. **18**: p. 265-271.
39. Connelly, R., W. Parsons, and G. Pearson, *Prediction of Peel Adhesion using Extensional Rheometry*. J. Rheology, 1981. **25**: p. 315-328.
40. Good, R.J. and R.K. Gupta, *Rheological, Interfacial and Thermal Control of Polymer Adhesion. I. Isothermal Theory*. J. Adhesion, 1989. **26**: p. 13-36.
41. Christensen, S.F. and G.H. McKinley, *Rheological Modeling of the Peeling of Pressure Sensitive Adhesives and other Elastomers*. Int. J. Adhesion & Adhesives, 1998. **18**: p. 333-343.

42. Reynolds, O., *On the Theory of Lubrication and Its Application to Mr. Beauchamp Tower's Experiments*. Phil. Trans. Roy. Soc. London, 1886. **177**: p. 157-234.
43. Saffman, P.G. and G. Taylor, *The penetration of a fluid into a porous medium or a Hele-Shaw cell containing a more viscous liquid*. Proc. Roy. Soc. London, A, 1958. **245**: p. 312-329.
44. Hele-Shaw, H.S., *The Flow of Water*. Nature, 1898. **58**: p. 34-36.
45. Paterson, L., *Radial fingering in a Hele Shaw cell*. J. Fluid Mech., 1981. **113**: p. 513-529.
46. Thome, H., M. Rabaud, V. Hakim, and Y. Couder, *The Saffman- Taylor Instability: From linear to circular geometry*. Phys. Fluids A, 1989. **1**: p. 224.
47. van Damme, H., E. Alsac, C. Laroche, and L. Gatineau, *On the Respective Roles of Low Surface Tension and non-Newtonian Rheological Properties in Fractal Fingering*. Europhys. Lett., 1987. **5**: p. 25-30.
48. Rausedo, S.N., P.D. Barnes Jr., and J.V. Maher, *Development of Radial Fingering Patterns*. Phys. Rev. A., 1993. **35**: p. 1245-1251.
49. Ben-Jacob, E., R. Godbey, N.D. Goldenfeld, J. Koplik, H. Levine, T. Mueller, and L. Sander, *Experimental Demonstration of the Role of Anisotropy in Interfacial Pattern Formation*. Phys. Rev. Letters, 1985. **55**: p. 1315-1318.
50. Daccord, G. and J. Nittman, *Radial Viscous Fingers and Diffusion-Limited Aggregation: Fractal Dimension and Growth Sites*. Phys. Rev. Letters, 1986. **56**: p. 336-339.
51. Pearson, J., *The instability of uniform viscous flow under rollers and spreaders*. J. Fluid Mech., 1960. **7**: p. 481-501.
52. Pitts, E. and J. Greiller, *The flow of thin liquid films between rollers*. J. Fluid Mech., 1961. **11**: p. 33-50.
53. Shelley, M.J., F. Tian, and K. Wlodarski, *Hele-Shaw flow and pattern formation in a time-dependant gap*. Nonlinearity, 1997. **10**: p. 1471-1495.
54. Fabre, P., *personal communication*. 2001.
55. Thamida, S., P. Takhistov, and H.-C. Chang, *Fractal dewetting of a viscous adhesive film between separating parallel plates*. Phys. Fluids, 2001. **13**: p. 2190-2200.
56. Crosby, A.J., K.R. Shull, H. Lakrout, and C. Creton, *Deformation and failure modes of adhesively bonded elastic layers*. J. Applied Phys., 2000. **88**(5): p. 2956-2966.

57. Shull, K.R., D. Ahn, W. Chen, C. Flanigan, and A.J. Crosby, *Axisymmetric adhesion tests of soft materials*. Macromol. Chem. Phys., 1998. **199**: p. 489-511.
58. Crosby, A.J. and K.R. Shull, *Adhesive Failure Analysis of Pressure-Sensitive Adhesives*. J. Polym. Sci., Part B: Polym. Phys., 1999. **37**: p. 3455-3472.
59. Shull, K.R., C.M. Flanigan, and A.J. Crosby, *Fingering Instabilities in Confined Elastic Layers in Tension*. Phys. Rev. Letters, 2000. **84**(14): p. 3057-3060.
60. Spiegelberg, S.H. and G.H. McKinley, *Stress relaxation and elastic decohesion of viscous polymer solutions in extensional flow*. J. Non-Newtonian Fluid Mech., 1996. **67**: p. 49-76.
61. Kaelble, D.H., *Theory and Analysis of Peel Adhesion*. Trans. Soc. Rheol., 1959. **3**: p. 161-180.
62. Gierenz, G. and W. Karmann, *Adhesives and Adhesive Tapes*. 2000, Weinheim: Wiley-VCH.
63. Johnson, K., K. Kendall, and A. Roberts, *Surface energy and the contact of elastic solids*. Proc. Roy. Soc. London, A, 1971. **324**: p. 301-313.
64. Hertz, H., *Ueber die Behrührung fester elastischer Körper*. J. reine u. angew. Math., 1882. **92**: p. 156-171.
65. *ASTM Standards*, in *Standard Test Method for Pressure Sensitive Adhesive Adhesives Using an Inverted Probe Machine*. 1998. p. 183-185.
66. Wetzel, F., *Rosin and Rosin Derivatives in Pressure-Sensitive Adhesives*. Rubber Age, 1957. **82**: p. 291-295.
67. Zosel, A., *Adhesion and tack of polymers: Influence of mechanical properties and surface tensions*. Colloid & Polymer Sci., 1985. **263**: p. 541-553.
68. Brauner, O.F., *Steady Spinning of Synthetic Silk-like Fibers and Transient Filament Stretching of Semi-Dilute and Concentrated Polymer Fluids*, in *Department of Chemical Engineering*. 2001, MIT: Cambridge.
69. Francis, B.A. and R.G. Horn, *Apparatus-specific analysis of fluid adhesion measurements*. J. Applied Phys., 2000. **89**: p. 4167-4174.
70. Pitois, O., P. Moucherant, and X. Chateau, *Liquid Bridge between Two Moving Spheres: An Experimental Study of Viscosity Effects*. J. Coll. and Inter. Sci., 2000. **231**: p. 26-31.

71. Graessley, W., *Polymer chain dimensions and the dependence of viscoelastic properties on concentration, molecular weight and solvent power*. *Polymer*, 1980. **21**: p. 258-262.
72. Rothstein, J.P. and G.H. McKinley, *Non-Isothermal Modifications of Purely Elastic Flow Instabilities in Torsional Flows of Polymeric Fluids*. *Phys. Fluids*, 2001. **13**: p. 382-396.
73. Hencky, H., *The Elastic Behavior of Vulcanized Rubber*. *Trans. A.S.M.E.*, 1933. **55**: p. 45-53.
74. Rasmussen, H.K. and O. Hassager, *Three-dimensional simulations of viscoelastic instability in polymeric filaments*. *J. Non-Newtonian Fluid Mech.*, 1999. **82**: p. 189-202.
75. Rasmussen, H.K. and O. Hassager, *The Role of Surface Tension in the Elastic Decohesion of Polymeric Filaments*. *J. Rheology*, 2001. **45**: p. 527-537.
76. Bach, A., H.K. Rasmussen, P. Longin, and O. Hassager, *Controlled disturbances of the free surface in the filament stretching rheometer*. *J. Non-Newtonian Fluid Mech.*, 2001. **in print**.
77. Hassager, O., M.I. Kolte, and M. Renardy, *Failure and nonfailure of fluid filaments in extension*. *J. Non-Newtonian Fluid Mech.*, 1998. **76**: p. 137-151.
78. Yao, M. and G.H. McKinley, *Numerical Simulation of extensional deformations of viscoelastic liquid bridges in filament stretching*. *J. Non-Newtonian Fluid Mech.*, 1998. **74**: p. 47-88.
79. Bataille, J., *Stabilité d'un Déplacement Radial Non Miscible*. *Revue de L'Institut Français du Pétrole*, 1968. **23**: p. 1349-1364.
80. Ide, Y. and J.K. White, *The spinnability of polymer fluid filaments*. *J. Appl. Polym. Sci.*, 1976. **20**: p. 2511-2531.